The Nature of High-Energy Tail Electron Precipitation

Josephine Alessandra Salice

Thesis for the degree of Philosophiae Doctor (PhD)
University of Bergen, Norway
2024

UNIVERSITY OF BERGEN

The Nature of High-Energy Tail Electron Precipitation

Josephine Alessandra Salice

Thesis for the degree of Philosophiae Doctor (PhD)
at the University of Bergen

Date of defense: 14.06.2024

Year: 2024

Title: The Nature of High-Energy Tail Electron Precipitation

Name: Josephine Alessandra Salice

Print: Skipnes Kommunikasjon / University of Bergen

Scientific environment

This study is carried out at the Department of Physics and Technology, University of Bergen. The work is supported by The Research Council of Norway (RCN) under the contracts 223252 and 302040.

Acknowledgements

First and foremost, I would like to thank my supervisor, Hilde Nesse, without whom this thesis would not have been possible. Our many discussions were invaluable, and your readiness to answer questions never went unnoticed. Your support in my outreach initiatives is deeply appreciated. I would not have won Forsker Grand Prix without you. Thank you for including me in CAS, which opened doors to meet co-authors who enriched my research journey—my thanks extend to them as well. To my co-supervisor, Christine, thank you for all the help and support. I wish you had stayed longer.

Heartfelt thanks to my fellow fourth-floor PhDs for making office life fun. Special appreciation to Eldho for priceless journeys, Ingrid for initiating G&T nights, Simon for delicious banana bread and candy, and Michael for enriching discussions. A profound thanks to Margot for being an exceptional friend whose support has been invaluable. Finishing this thesis would have been far more challenging and riddled with errors without you. I cherish all your friendships and hope they last a lifetime.

I want to thank everyone in my Norwegian, American, and Italian family for all your support. It has not gone unnoticed. Thank you for cheering me on during Forsker Grand Prix, even when some of you did not understand a word. With all four of my parents holding doctorates, it seems I was doomed from the start. A special thanks to my mom, Sonia, whose unwavering belief in me has been my rock. I would be lost without you. To my pappa, Kjetil, thank you for facing my writing challenges with me growing up. Turns out I ended up writing a lot more than I thought I would. To Dad, Jamie, and Alex, you guys are epic; thank you for being you. Theo, thank you for also being snål. To G-ma, thank you for being such an inspiration. Kristin, my ultimate training partner, I would have gone insane without you. Inga, thank you for supporting me and cheering me on. To Andrine, thank you for being such a fantastic human being. Your friendship means the world to me.

To my dearest Erlend, thank you for believing in me and enduring living with me through this Journey. I love you og elsker at du er du.

Josephine A. Salice
Bergen, 21.03.2024

Abstract

This thesis is part of the research effort at the University of Bergen trying to understand "What are the effects of particle precipitation on the atmosphere?". An important step toward an answer is to improve the parameterization of Medium Energy Electron (MEE, $\gtrsim$ 30 keV) precipitation used as input in chemistry-climate models. MEE precipitation ionizes the mesosphere and upper stratosphere and initiates chemical reactions that ultimately might change the polar atmospheric circulation and impact the regional winter weather patterns at high latitudes.

MEE parameterizations often fail to accurately capture the intensity, extent, and duration of events, particularly when considering the high-energy tail of MEE ($\gtrsim$ 300 keV). This thesis aims to increase our understanding of these high-energy tail electrons, offering valuable insights for improving atmospheric models and understanding magnetospheric dynamics. Organized in three research papers, the thesis uses optimized MEE precipitation measurements from the Medium Energy Proton and Electron Detectors aboard the Polar Operational Environmental Satellite (POES) and Meteorological Operational Satellite (MetOp) series. Solar wind parameters and geomagnetic indices such as AE, Kp, and Dst are used to evaluate the solar wind driving and magnetospheric processes. The datasets span one solar cycle from 2004 to 2014.

Paper I investigates the intensity, timing, and duration of the $\gtrsim$ 300 keV versus $\gtrsim$ 30 keV fluxes against different solar wind structures. It reveals that the more frequent high-speed solar wind streams result in weaker responses than the less frequent coronal mass ejections and that the high-energy tail properties are dependent on structure. Despite a strong overall correlation (0.89) between the flux peaks of the two channels, the higher energies can deviate by an order of magnitude for a certain $\gtrsim$ 30 keV response. High-energy fluxes typically peak at zero to three days after the lower energies, with solar wind dynamics influencing the delay. The $\gtrsim$ 300 keV flux generally lasts four days, somewhat independent of solar wind drivers, in contrast to the shorter-lived $\gtrsim$ 30 keV response. The distinctions found within the MEE spectrum highlight the importance of integrating such nuances into atmospheric modeling, and the results further suggest a stochastic MEE parameterization for a more precise representation of the different effects driven by solar wind dynamics.

Paper II analyzes solar wind properties and geomagnetic responses associated with substantial $\gtrsim$ 30 keV flux events that are further categorized by their high-energy tail response. It finds that strong $\gtrsim$ 300 keV fluxes can enhance the NO density down to 60 km, but that no single parameter fully explains their variability. However, patterns of elevated solar wind speeds after deep Dst troughs seem to be important for strong responses in these high energies. A probability assessment revealed that certain thresholds of Kp and Dst can close to guarantee or exclude strong $\gtrsim$ 300 keV responses identifying over half of the selected events. The thresholds for Dst are dependent on solar wind structure and can lead to a more accurate assessment if taken into account. Though providing insight into how thresholds can be used in a stochastic MEE model, it was concluded that case studies were needed to specifically understand what causes significant enhancements of $\gtrsim$ 300 keV precipitation.

Paper III builds on Paper II by examining case studies of the events with strong $\gtrsim$ 30 keV fluxes that are separated by weak versus strong $\gtrsim$ 300 keV fluxes. It reveals that a combined application of Kp and Dst criteria can identify about 85% of these events across the solar cycle. However, the study notes the need to refine the theory that high solar wind speeds following a deep Dst trough lead to significant $\gtrsim$ 300 keV fluxes and highlight the importance of sustained geomagnetic activity and radiation belt preloading. It also finds that predicting the absence of strong $\gtrsim$ 300 keV fluxes is more straightforward than predicting its occurrence, as the direction of the solar wind magnetic field plays a critical role in inhibiting such events.

Combined, the three papers imply that concurrent criteria and/or a stochastic approach is required to better capture the nature of the high-energy tail of electron precipitation in chemistry-climate models.

Sammendrag

Denne avhandlingen er en del av en større forskningsinnsats ved Universitetet i Bergen som prøver å forstå "Hva er effektene av partikkelnedbør på atmosfæren?". Ett viktig steg mot et svar er å forbedre parametriseringen av Medium Energy Electrons (MEE, $\gtrsim$ 30 keV) som blir brukt som inndata i kjemiske klimamodeller. MEE nedbør ioniserer mesosfæren og den øvre stratosfæren og initierer kjemiske reaksjoner som i siste instans kan endre den polare atmosfæriske sirkulasjonen og påvirke det regionale været ved høye breddegrader om vinteren.

MEE parametriseringer klarer ikke å fange opp intensiteten, omfanget, eller varigheten av hendelser, spesielt når man vurderer de høyeste energiene eller "halen" til energispekteret ($\gtrsim$ 300 keV). Denne avhandlingen tar sikte på å øke vår forståelse av denne halen, og tilbyr verdifull innsikt for forbedring av atmosfæriske modeller og en dypere forståelse av dynamikken i magnetosfæren som forårsaker dem. Organisert i tre forskningsartikler bruker avhandlingen optimaliserte målinger av MEE nedbør fra Medium Energy Proton and Electron Detectors ombord på Polar Operational Environmental Satellite (POES) og Meteorological Operational Satellite (MetOp) serien. Solvindparametre og geomagnetiske indekser som AE, Kp og Dst brukes for å evaluere solvindens påvirkning og magnetosfæriske prosesser. Datasettene dekker en solsyklus fra 2004 til 2014.

Artikkel I undersøker intensiteten, timingen og varigheten av $\gtrsim$ 300 keV versus $\gtrsim$ 30 keV fluksene mot ulike solvindstrukturer. Den avdekker at de mer hyppige høyhastighetsstrømmene resulterer i svakere respons enn de mindre hyppige koronautbruddene, og at egenskaper til MEE halen er avhengige av solvindstruktur. Til tross for en sterk overordnet korrelasjon (0.89) mellom de to fluxsene, kan høyere energier avvike med en størrelsesorden for en bestemt $\gtrsim$ 30 keV respons. Fluxes til halen når sin topp null til tre dager etter de lavere energiene, der solvindstruktur påvirker evalueringen. $\gtrsim$ 300 keV fluksen varer generelt fire dager, noe uavhengig av struktur, i motsetning til den kortvarige $\gtrsim$ 30 keV responsen. Forskjellene funnet innen MEE spekteret understreker viktigheten av å integrere slike nyanser i atmosfærisk modeller, og resultatene antyder videre at en stokastisk MEE parametrisering kan gi en mer presis representasjon av de forskjellige effektene drevet av solvinden.

Artikkel II analyserer solvindsegenskaper og geomagnetiske responser assosiert med betydelige $\gtrsim$ 30 keV flukser som videre kategoriseres etter halens respons. Den finner at sterke $\gtrsim$ 300 keV flukser kan øke tettheten av NO ned til 60 km, men at ingen av pa-

rameter kan alene forklare variasjonen. Høy solvindhastighet etter et dypt Dst utslag ser ut til å være viktig for sterk respons i halen. En sannsynlighetsvurdering avslørte at visse terskler for Kp og Dst nesten kan garantere eller utelukke en sterk $\gtrsim$ 300 keV respons, og står for over halvparten av de identifiserte hendelsene. Tersklene for Dst er avhengige av solvindstrukturen og gir en mer nøyaktig vurdering hvis de tas i betraktning. Selv om det gir innsikt i hvordan terskler kan brukes i en stokastisk MEE modell, ble det konkludert at det var nødvendig med å analysere de enkelte tilfellene for å forstå hva som forårsaker betydelige fluksøkninger i $\gtrsim$ 300 keV elektronnedbør.

Artikkel III bygger på Artikkel II ved å undersøke enkle tilfellene med sterke $\gtrsim$ 30 keV flukser delt inn i svake versus sterke $\gtrsim$ 300 keV flukser. Den avslører at en kombinert anvendelse av Kp- og Dst-kriterier identifiserer omtrent 85% av disse hendelsene gjennom disse 11 årene. Imidlertid påpeker studien behovet for å modifisere teorien om at høye solvindhastigheter etter en dyp Dst fører til betydelige $\gtrsim$ 300 keV flukser, og understreker betydningen av vedvarende geomagnetisk aktivitet og et allerede styrket strålingsbelte. Den finner også ut at det er enklere å forutsi fraværet av sterke $\gtrsim$ 300 keV flukser, ettersom retningen på det magnetiske feltet i solvinden spiller en avgjørende rolle i å hemme slike hendelser.

Samlet sett antyder de tre artiklene at samtidige kriterier og/eller en stokastisk tilnærming er nødvendig for bedre å gjenspeile naturen til halen av MEE nedbør i kjemiske klimamodeller.

List of Publications

This thesis and the collection of papers within are submitted for the degree of Philosophiae Doctor (PhD) in physics at the Department of Physics and Technology, University of Bergen.

The thesis consists of an introductory part, two published articles, and one article currently under review. All papers are published or under review in international peer-reviewed journals.

Paper I J. Salice, H. Nesse, E. M. Babu, C. Smith-Johnsen, and I. G. Richardson (2023), *Exploring the Predictability of the High-Energy Tail of MEE Precipitation Based on Solar Wind Properties*, JGR Space Physics, Vol. 128, Issue 3, doi: 10.1029/2022JA031194

Paper II J. Salice, H. Nesse, N. Partamies, E. Kilpua, A. Kavanagh, M. Decotte, E. M. Babu, and C. Smith-Johnsen (2024), *The High-Energy Tail of Energetic Electron Precipitation: Solar Wind Drivers and Geomagnetic Responses*, Front. Astron. Space Sci., Vol. 11, doi: 10.3389/fspas.2024.1352020

Paper III J. Salice, and H. Nesse (2024), *The High-Energy Tail of Energetic Electron Precipitation: Case Studies*, Submitted to Front. Astron. Space Sci. on 16-March-2024

During my PhD studies, I have also contributed to the following papers.

A H. Nesse, N. Partamies, E. M. Babu, C. Smith-Johnsen, and J. A. Salice (2021), *The Predictive Capabilities of the Auroral Electrojet Index for Medium Energy Electron Precipitation*, Front. Astron. Space Sci., Vol. 8, doi: 10.3389/fspas.2021.714146

B E. M. Babu, H. Nesse, C. Smith-Johnsen, V. Maliniemi, J. A. Salice, R. M. Millan, and I. G. Richardson (2022), *Determining Latitudinal Extent of Energetic Electron Precipitation Using MEPED On-Board NOAA/POES*, JGR Space Physics, Vol. 127, Issue 9, doi: 10.1029/2022JA030489

C E. M. Babu, H. Nesse, S. M. Hatch, N. Olsen, J. A. Salice, I. G. Richardson (2023), *An Updated Geomagnetic Index-Based Model for Determining the Latitudinal Extent of Energetic Electron Precipitation*, JGR Space Physics, Vol. 128, Issue 10, doi: 10.1029/2023JA031371

D H. Nesse, E. M. Babu, J. A. Salice, and B. Funke (2023), *Energetic Electron Precipitation During Slot Region Filling Events*, JGR Space Physics, Vol. 128, Issue 10, doi: 10.1029/2023JA031606

E M. Decotte, K. M. Laundal, J. A. Salice, S. M. Hatch, S. Haaland, and A. Ohma (2024), *Revealing the effect of Earth's rotation on geospace*, Submitted to Nature on 13-March-2024

Contents

1 Introduction

The solar wind is a constant stream of energetic particles emitted from the Sun. It consists primarily of protons and electrons. Upon reaching Earth, the planet's magnetic field acts as a shield, defending against most solar wind particles. Nonetheless, a fraction of these particles can still penetrate and become trapped within Earth's magnetic field environment. This not only poses a risk of radiation damage to satellites and astronauts but also contributes to the phenomenon known as Energetic Particle Precipitation (EPP). EPP deposits its energy in the upper and middle atmosphere by ionization, dissociation, or excitation of atmospheric gases. These reactions can affect the atmosphere in varied and complex ways. This thesis is part of the research group at the University of Bergen that investigates the impacts of precipitating particles on the atmosphere. More specifically, the work in this thesis focuses on Energetic Electron Precipitation (EEP).

EEP is most commonly known for its visual display of the auroras in the polar night sky. Another effect of EEP is the production of the chemically reactive species of odd nitrogen (NO_x: NO, NO_2) and odd hydrogen (HO_x: H, OH, HO_2) gases. These gases can catalytically destroy mesospheric and stratospheric ozone at high latitudes. NO_x is particularly important due to its long lifetime during polar winter darkness. Ozone plays a crucial role in absorbing incoming UV radiation and converting it into thermal energy that heats the local atmosphere. However, in the absence of sunlight, ozone emits infrared radiation, which leads to a cooling effect. Hence, altering ozone concentration will affect the local temperature. Changes in temperature due to EEP-induced ozone depletion can initiate complex feedback loops that can change the polar atmospheric circulation, which ultimately can map down onto regional surface climate (*Seppälä et al.*, 2013; *Maliniemi et al.*, 2016).

The strength of EEP's atmospheric impact is highly dependent on the fluxes and energies of the precipitating electrons. The abundant auroral electrons have energies $\lesssim 30$ keV, which allows them to reach the lower thermosphere and upper mesosphere. Auroral precipitation is the main driver of the EEP indirect effect, which is associated with the general downward circulation at the pole that transports NO_x to mesospheric and stratospheric altitudes. At these lower altitudes, NO_x can efficiently impact ozone. In contrast, Medium Energy Electrons (MEE) originate from the radiation belt, where they have been accelerated to energies $\gtrsim 30$ keV. MEE precipitation can reach the mesosphere, and its high-energy tail ($\gtrsim 300$ keV) can even reach the upper stratosphere, allowing for a direct effect on ozone.

Figure 1.1: A view of the aurora from the International Space Station caused by energetic particles precipitating into the atmosphere. Credit: NASA

The atmospheric effects of the frequent auroral EEP have been extensively studied and are fairly well established (*Marsh et al.*, 2004; *Sinnhuber et al.*, 2011). However, accurate quantification of the MEE spectrum remains difficult due to instrumental challenges and various data handling, as well as incomplete knowledge of the complex magnetospheric dynamics that trap, accelerate, and scatter the electrons in the inner magnetosphere. These challenges manifest themselves in the parameterizations of MEE precipitation used in chemistry-climate models.

Current MEE parameterizations fall short in reproducing not only the intensity of MEE precipitation events but also in capturing the atmospheric extent and duration of the events (*Tyssøy et al.*, 2019; *Nesse Tyssøy et al.*, 2022). They typically offer an averaged MEE response and use a single geomagnetic index for scaling. This approach struggles to capture the variation of the precipitation over daily to decadal scales, especially when considering the high-energy tail of MEE during periods of strong solar wind driving. Understanding the mechanisms that drive these high-energy tail electrons and how they differ from the lower-energy MEE might be one of the missing puzzle pieces for optimizing MEE parameterization.

Refining current MEE parameterizations is essential to achieving a more accurate assessment of EEP's atmospheric effects and its role in solar forcing. This requires optimized data handling and a comprehensive understanding of the entire MEE energy spectrum.

1.1 Objective

Building on the optimized estimates of precipitating MEE fluxes by *Nesse Tyssøy et al.* (2016), this thesis aims to investigate the nature of high-energy tail MEE precipitation. The objective is to increase our understanding of the high-energy tail's unique behavior and drivers. To achieve this, the thesis sets out to answer two main research questions:

1. How do the characteristics of the high-energy tail differ from those of lower-energy MEE precipitation?
2. Which solar wind and geomagnetic parameters can capture the variations in the high-energy tail of MEE precipitation?

Paper I addresses the first research question by comparing $\gtrsim$ 30 keV with $\gtrsim$ 300 keV fluxes within the context of different solar wind structures and their properties. More specifically, it quantifies how the fluxes vary in intensity, timing, and duration. The analysis is done using data over 11-years from 2004 to 2014.

Paper II addresses the second research question by analyzing solar wind properties and geomagnetic responses associated with substantial $\gtrsim$ 30 keV flux events. The events are selected over the same period as in Paper I. This analysis further categorizes the events by the intensity of their high-energy tail response. Through superposed epoch analysis, Paper II aims to determine the strength of the solar wind and geomagnetic responses required for significant high-energy tail fluxes. It also seeks to provide insight into the magnetospheric dynamics that drive these high energies. The focus on the largest MEE flux responses addresses the challenge of their underestimation in current parameterizations.

Paper III focuses on specific case studies based on a selection of events defined in Paper II. These events all have strong $\gtrsim$ 30 keV fluxes but are separated by strong versus weak $\gtrsim$ 300 keV fluxes. This targeted analysis aims to deeply investigate the specific solar wind and geomagnetic properties that lead to strong high-energy tail fluxes.

Together, these papers advance our understanding of the high-energy tail of MEE precipitation and its solar and magnetospheric drivers. They pave the way for an improved MEE parameterization that captures the nature of these high-energy electrons. This research also marks a crucial step toward the creation of a stochastic MEE model that goes beyond the typical average response scaled by geomagnetic activity. The initiative to more accurately capture the variability of the entire MEE energy spectrum is motivated by the need for a realistic assessment of EEP's atmospheric effects. Furthermore, this collective work can enrich radiation belt research and the field of solar atmospheric forcing, providing benefits across these scientific communities.

1.2 Outline

Chapter 2 introduces the solar wind and magnetosphere's interactions, focusing on the processes that lead to EEP. Chapter 3 provides insight into EEP's atmospheric effects and addresses the challenges in parameterizing MEE, which motivates this research. Chapter 4 provides an in-depth look at the data sources and some methodologies. Chapter 5 introduces the three research papers that each contribute to a better understanding of MEE precipitation. Chapter 6 summarizes the key findings of the thesis and outlines directions for future research, highlighting the study's contributions to the field of atmospheric and space sciences. Finally, the three papers that constitute the thesis are presented in full.

2 The Origin of Energetic Particle Precipitation

This chapter provides the scientific foundation to understand the origin of Energetic Particle Precipitation (EPP), with a particular focus on Energetic Electron Precipitation (EEP). Originating from the Sun, these particles journey through interplanetary space as the solar wind. Encountering Earth, the interaction between the solar wind and the magnetosphere causes geomagnetic disturbances and facilitates transportation and acceleration of particles within the magnetosphere.

Section 2.1 provides an overview of the solar wind and its drivers. Section 2.2 explores the complex interactions between the solar wind and the magnetosphere, including the mechanisms of solar wind-magnetosphere coupling, regions of the inner magnetosphere, and geomagnetic storms. Finally, Section 2.3 introduces the magnetospheric dynamics that lead to EEP.

2.1 The Solar Wind and its Structures

The solar wind is a highly conducting plasma emitted from the Sun's corona, consisting mainly of electrons and protons. Embedded in the solar wind is the Sun's magnetic field, referred to as the Interplanetary Magnetic Field (IMF). The solar wind travels at supersonic speeds ranging from about 200 km/s to 800 km/s. The behavior of the solar wind is not uniform; it varies in density, velocity, and temperature, largely influenced by the solar magnetic field and the level of solar activity. These variations play an important role in shaping the dynamics of near-Earth space, driving what is known as space weather.

Figure 2.1 shows a schematic of the two primary large-scale structures within the solar wind. They originate from distinct solar sources and play a crucial role in driving strong space weather conditions. Coronal holes are areas on the Sun where its magnetic field lines stretch out into space instead of looping back to the surface. These areas are cooler and less dense than the surrounding plasma and facilitate rapid, uninterrupted escape of plasma into space due to their open magnetic field lines. This results in what is known as High-speed Solar wind Streams (HSS) (shown to the left in Figure 2.1). When these swift-moving streams overtake the slower-moving solar wind ahead, the interaction compresses the IMF and plasma, forming what are called Co-rotating Interaction Regions (CIR). The term "co-rotating" refers to the fact that these interaction regions can last long enough to cycle back into Earth's vicinity with the Sun's approximately 27-day

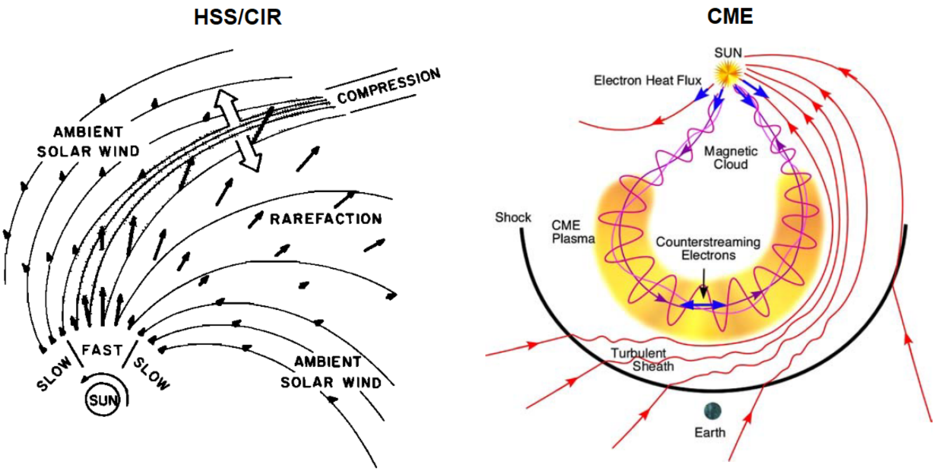

Figure 2.1: A schematic illustration of the properties of the two primary large-scale solar wind structures. To the left is a typical HSS leading to a compressed CIR (taken from *Pizzo* (1978)). To the right is a typical CME with its preceding shock and sheath (taken from *Zurbuchen and Richardson* (2006)).

rotation, sometimes reappearing multiple times. From the perspective of a fixed observer on Earth, a CIR will lead the HSS.

The other solar source contributing to intense space weather conditions involves sunspots, which are darker, cooler areas on the Sun's surface characterized by intense magnetic activity. These regions become more prevalent around solar maxima, a period marked by increased magnetic field flux around the Sun's equator. This increase results from the twisting of the Sun's magnetic field, causing it to bulge under pressure and extend through the photosphere. High magnetic stress leads to the reconnection and reconfiguration of magnetic field lines with opposite polarities, a process known as magnetic reconnection. Reconnection can unleash a sudden and powerful burst of electromagnetic energy, termed a solar flare. Furthermore, it can trigger an explosive release of plasma and magnetic fields into space, known as Coronal Mass Ejections (CMEs) (shown to the right in Figure 2.1). In escaping the Sun, CMEs often have greater speeds than the upstream solar wind, creating a supersonic fast-forward shock ahead of itself (*Kilpua et al.*, 2017). Between the CME and its shock is a turbulent plasma region called the sheath. Following the sheath, the core of the CME often contains a magnetic cloud, a structure with a coherent magnetic field that exhibits a helical shape.

The two solar wind structures have unique properties leading to different space weather conditions. Figure 2.2 illustrates a schematic highlighting their typical characteristics.

When observed in situ at approximately the Earth's distance from the Sun, a CIR's approach is marked by increases in density and pressure, accompanied by large amplitude magnetic field fluctuations (*Kataoka and Miyoshi*, 2006; *Kilpua et al.*, 2017). With the following arrival of the HSS, there is a decrease in density and pressure while the solar wind speed and temperature rise. In turn, a CME that is preceded by a shock wave is characterized by a sudden increase in all parameters. Similar to the CIR, the sheath region before a CME is characterized by significant magnetic field fluctuations. However, the CME's arrival is distinguished by a noticeable decrease in temperature and a more uniform magnetic field. The recovery from these elevated conditions tends to be more gradual for HSS/CIRs compared to CMEs.

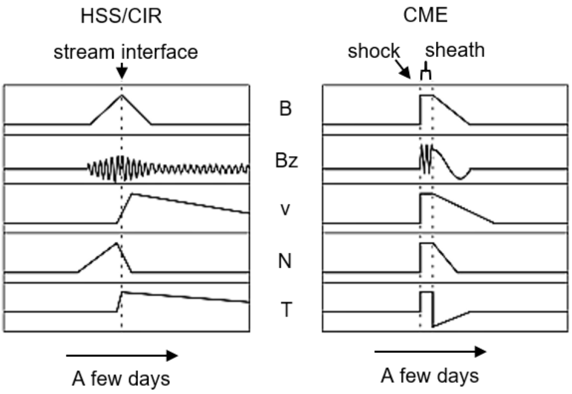

Figure 2.2: A schematic illustration of a typical HSS/-CIR and CME. From top to bottom, the magnetic field strength B, the south-north magnetic field components B_z, solar wind speed v, density N, and temperature T. Adapted from *Kataoka and Miyoshi* (2006).

The frequency at which Earth encounters these solar wind structures is influenced by the 11-year solar cycle. Figure 2.3 shows the annual distribution of these phenomena. CMEs, which are closely linked to sunspots, are most frequent during the solar maximum. In contrast, HSS/CIRs become more common in the declining phase of the solar cycle, as open magnetic field lines migrate to lower latitudes (e.g., *Asikainen and Ruopsa*, 2016). Throughout a solar cycle, HSS/CIR events have the highest occurrence frequency, in part because of their extended duration (*Asikainen and Ruopsa*, 2016). Section 2.2 will further discuss the geomagnetic activity and magnetospheric dynamics that these structures cause.

2.2 The Magnetosphere

Earth is surrounded by a vast magnetic field generated by the movement of molten iron within its outer core. In the absence of external influences, this geomagnetic field would take on a shape closely resembling that of a dipole. However, the dipole configuration is only observed near the Earth's surface; beyond that, the field experiences distortion caused by interactions with the solar wind.

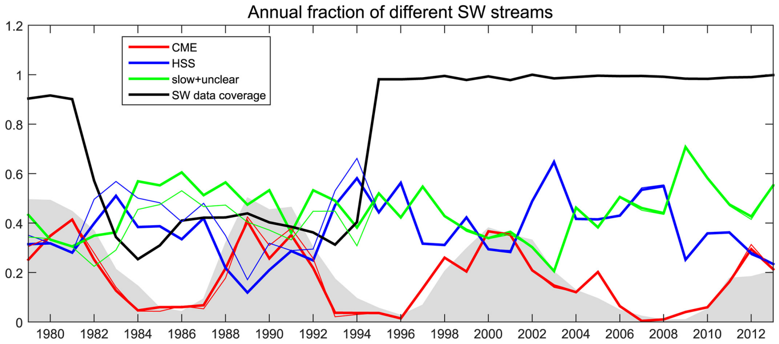

Figure 2.3: The yearly fractions of CMEs (red), HSSs (blue), and slow/ambient or unclear flows (green). Thin lines represent computations excluding missing data points, while thick ones include them. The solar cycle is represented by the annual sunspot number, shown as a shaded region in the background for reference. Taken from *Asikainen and Ruopsa* (2016).

As the solar wind and the accompanying IMF approach Earth's magnetic field, a bow shock forms, decelerating the plasma and converting kinetic energy into thermal energy. Between the bow shock and Earth's magnetic field lies the magnetosheath, a turbulent plasma region characterized by higher density, temperature, and magnetic strength than the solar wind. This sheath deflects the solar wind around the geomagnetic field, creating a cavity known as the magnetosphere. The magnetosphere is the region of space surrounding Earth where Earth's magnetic field dominates. The boundary between the magnetosphere and magnetosheath is called the magnetopause.

The solar wind exerts pressure on the magnetosphere, compressing it on the day side and extending it into a long tail on the night side. The distortion results in a tear-drop shape. A schematic resembling the magnetosphere's shape is presented in Figure 2.4. Typically, the location of the magnetopause at the equator facing the Sun is approximately 10 to 12 Earth radii (R_E) (*Fairfield*, 1971; *Haaland et al.*, 2021) but it can be compressed by several R_E. The magnetotail extends several thousand R_E from Earth on the night side (*Milan et al.*, 2004), but it generally reconnects at distances ranging between 23 to 31 R_E (*Milan et al.*, 2004; *Nagai et al.*, 2023). The location of these regions depends on solar wind conditions.

The geomagnetic field's orientation is stable, with the magnetic south pole situated in the geographic Northern Hemisphere (NH) and the magnetic north pole located in the geographic Southern Hemisphere (SH). The magnetic axis is tilted approximately 11° from Earth's rotational axis. The direction of the IMF as it approaches Earth varies. When components of the IMF are antiparallel to those of the geomagnetic field, magnetic reconnection occurs, allowing plasma transfer from the solar wind to the magnetosphere. The process connects the geomagnetic field lines to the IMF, which are then pulled to

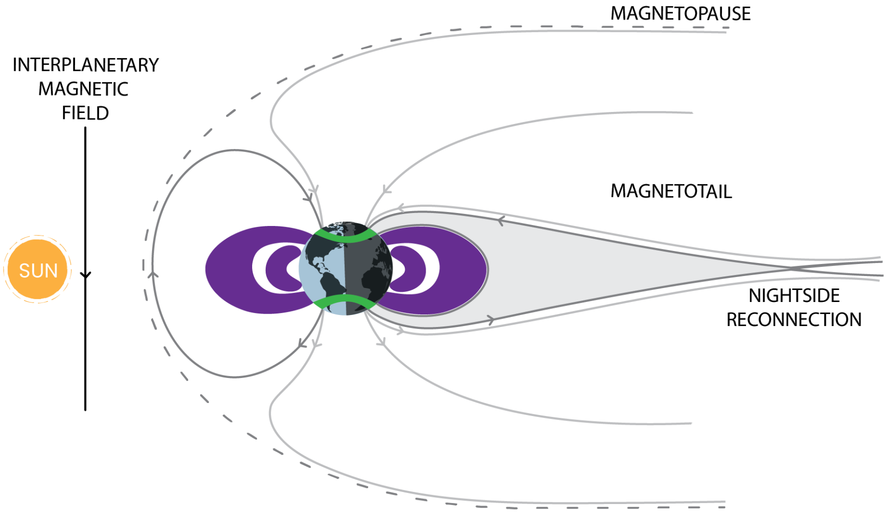

Figure 2.4: A schematic of the magnetosphere influenced by the solar wind. Grey and light grey solid lines indicate closed and open magnetic field lines, respectively. Figure by Margot Decotte.

and stretched out on the night side by the solar wind flow. There, reconnection within the magnetotail seals these field lines. The magnetic tension forces them to snap back to a more dipolar-like structure, accelerating plasma from the tail toward Earth. The field lines will then work their way back to the day side, completing what is known as the Dungey cycle (*Dungey*, 1961).

As such, the solar wind drives the process of magnetospheric convection and acts as the primary source of plasma for the magnetosphere. Within the magnetosphere, the plasma is sorted into various regions depending on density and temperature.

2.2.1 Plasma Regions and Currents

This thesis is mainly concerned with inner magnetosphere plasma regions on closed, dipole-like magnetic field lines. Figure 2.5 shows a schematic of some of the plasma regions and currents generated by different plasma populations in the inner magnetosphere. The innermost part of the magnetosphere is called the plasmasphere. It is a doughnut-shaped region of cold plasma originating from the top of the atmosphere. Depending on geomagnetic activity, the outer boundary, called the plasmapause, varies from about $L = 3$ to $L = 6$ (*Moldwin et al.*, 2002, and references therein), where L refers to the L-shell denoting the closed magnetic field lines intersecting Earth's mag-

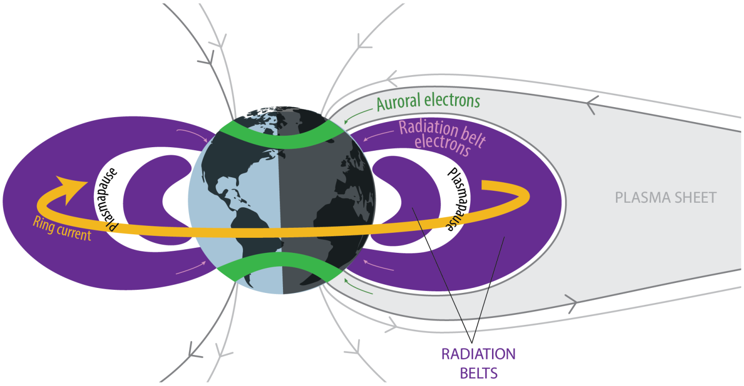

Figure 2.5: Same as Figure 2.4 just zoomed in to show a selection of plasma regions and currents in the inner magnetosphere. Figure by Margot Decotte.

netic equator at a radial distance expressed in R_E. The footpoints of the magnetic field lines move to higher latitudes with increasing L-value.

The radiation belts, or Van Allen Belts, are typically two doughnut-shaped zones of trapped particles (purple regions in Figure 2.5). The inner radiation belt is found within the plasmasphere, which mainly consists of high-energy protons with energies of 10s to 100s of MeV and electrons with energies < 1 MeV (*Millan and Baker*, 2012). The source of these particles is mainly Cosmic Ray Albedo Neutron Decay (CRAND) (*Millan and Baker*, 2012). As such, this region is fairly stable over time, with the maximum flux usually confined within $\mathrm{L} = 2$ (*Sarno-Smith*, 2015). As the proton population extends outward, their average energy decreases; The weaker magnetic field strength leads to increased gyro-radius of protons and requires that protons have lower energy levels to ensure their entrapment. Further details on trapped particles and their dynamics will be explored in Section 2.3.

While the proton population extends outward in a continuous fashion, the electron populations are separated by a region of vacancy known as the slot region. The slot region is located within the plasmasphere near its outer boundary and is formed by various wave-particle interactions. Ultra-Low Frequency (ULF) electromagnetic waves drive inward diffusion of the electrons while plasmaspheric hiss and lightning-generated whistles scatter the electrons into the atmosphere (*Kim et al.*, 2011). More on wave-particle interactions will be discussed in Section 2.3.

The outer radiation belt starts at approximately the same region as the plasmapause with an outer edge varying between L = 6 and L = 10 depending on geomagnetic activity (*Sarno-Smith*, 2015). This region is dominated by a highly dynamic electron population with energies from 10s of keV to several MeV (*Millan and Baker*, 2012). The high-energy electron population in the outer radiation belt, which has higher energies than what is found in the solar wind, predominantly originates from the acceleration of lower-energy particles within the magnetosphere.

The plasma sheet is a region of relatively dense low-energy particles with energies of about one to a few 10s of keV (shaded region in Figure 2.5). The sheet extends down the magnetotail, separating the northern and southern lobes. These particles are energized and injected into the inner magnetosphere during substorm events, where they serve as the source of $>$ 30 keV electron energies. Substorms are dynamic processes in Earth's magnetosphere driven by solar wind-magnetosphere interactions, involving the sudden release of stored magnetic energy from the magnetotail (*Rostoker et al.*, 1980). This results in the rapid injection of particles into the near-Earth environment and is often associated with enhanced auroral activity. In the inner magnetosphere, the particles can further get accelerated through wave-particle interactions and radial diffusion to reach the energies of several MeV.

The movement of positive and negatively charged particles differ in the presence of magnetic fields. As the plasma from the tail gets accelerated toward Earth, the particles will experience an increasing magnetic field gradient. This causes electrons to drift eastward and protons westward perpendicular to both the magnetic field and magnetic gradient direction. The drift leads to a large-scale magnetospheric current called the ring current (yellow arrow in Figure 2.5). The current is located within the plasmasphere and outer radiation belt (*Jorgensen et al.*, 2004).

2.2.2 Geomagnetic Storms

The ring current is often used as a measure of geomagnetic activity. When the IMF has a southward component ($B_z < 0$) for an extended period of time, magnetospheric convection is strengthened, and particle injections from the magnetotail to the inner magnetosphere are increased. The increase in particles will enhance the ring current, diminishing the measurable geomagnetic field via ground-based magnetometers at low latitudes. The Disturbance Storm Time (Dst)-index, a proxy for geomagnetic activity levels, reflects the influence of the ring current, categorizing strong ring current enhancements as storms. A Dst of around 0 nT indicates quiet time conditions and negative deviations of $-$ 30 nT to $-$ 100s of nT give a range of geomagnetic storms from weak to great. Both HSS/CIRs and CMEs can accelerate the injection of plasma into the ring current.

Figure 2.6 shows a schematic of the typical Dst features for a CME-driven (top) and an HSS/CIR-driven (bottom) geomagnetic storm. CMEs preceded by shocks will lead to a strong compression of the day-side magnetopause, causing a sudden rise in Dst. Such a compression starts the initial phase of the storm and is referred to as a Storm Sudden Commencement (SSC) (e.g., *Tsurutani et al.*, 2006). If the following IMF has a southward component, the main phase of the storm starts with an abrupt increase in the ring current strength, visible as a large through in Dst. As long as there is energy coupling between the solar wind and magnetosphere, the energy injection will persist but typically lasts a couple of hours. When the coupling ceases, the injections stop and different loss processes lead to a slow recovery of the ring current, which can take up to a few days.

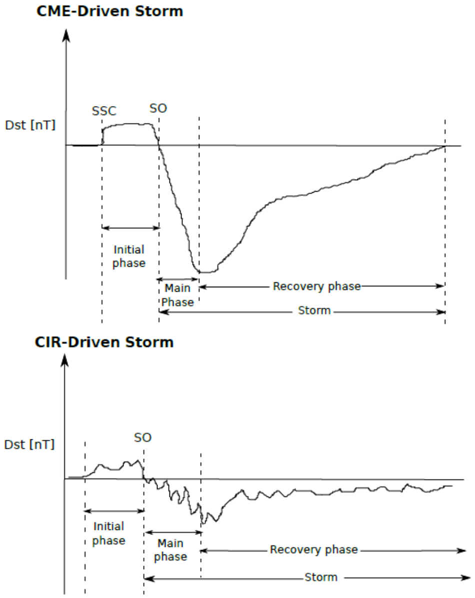

Figure 2.6: Schematics of typical Dst responses during CME-driven (top) and HSS/CIR-driven (bottom) geomagnetic storms. Taken from *Tsurutani et al.* (2006) and adapted by Annet Zawedde.

CIRs and their accompanying HSSs typically do not have a leading shock. The arrival of the high-density, low-velocity CIR causes a more gradual compression of the magnetosphere. The main phase of the storm is mostly driven by the following HSS. The highly fluctuating magnetic field will lead to on-and-off particle injections, typically producing weaker ring current injections over a longer time compared to CME-driven storms. Their long recovery is associated with the HSS lasting longer than the more abrupt CME.

2.3 Outer Radiation Belt Dynamics

The occurrence of CMEs and HSS/CIRs plays a crucial role in determining the rates of particle injection and the resulting fluxes within the outer radiation belt and ring current. A comprehensive understanding of the following acceleration and loss processes occurring in the outer radiation belt is essential for unraveling the complex mechanisms driving EEP. This section aims to shed light on the dynamics that govern trapped particles and to introduce the key acceleration and loss mechanisms. For a full overview of radiation

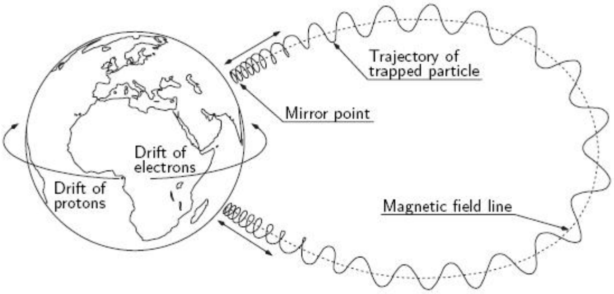

Figure 2.7: Schematic of the three basic motions of trapped particles in Earth's magnetic field. Retrieved online at *European Space Agency* (2007).

belt dynamics, see, e.g., *Koskinen and Kilpua* (2022).

2.3.1 Trapped Particle Motion

In a quasi-dipole magnetic field, electrically charged particles exhibit three fundamental types of motion: gyration around magnetic field lines, bounce motion between mirror points, and drift across the field lines. Each of these motions is governed by an adiabatic invariant, which is preserved as long as the magnetic field changes slowly compared with the timescale of the period of the motion. A schematic of the three particle motions is demonstrated in Figure 2.7.

The first adiabatic invariant is related to the conservation of magnetic flux encircled by a particle's gyration orbit. It implies that the gyration radius will either get smaller or larger depending on whether a particle moves into a region of stronger or weaker magnetic field strength, respectively.

The second adiabatic invariant is associated with a particle's bounce orbit between two mirror points. As a particle moves toward areas of increasing magnetic field strength, its velocity parallel to the field decreases while its perpendicular velocity increases. This dynamic changes the pitch angle, defined as the angle between the particle's velocity vector and the local magnetic field line. Upon reaching a pitch angle of 90°, the particle mirrors, reversing its trajectory. This mirroring effect leads to the particle's bounce motion between hemispheres (see Figure 2.7).

The third adiabatic invariant is related to the conservation of magnetic flux within a particle's drift orbit around the Earth. It suggests that a particle's drift path can adjust to slow variations in Earth's magnetic field, allowing for a stable orbit.

The combination of gyration, bounce, and drift motions within the magnetosphere, governed by their respective adiabatic invariants, is critical for the formation and maintenance of the ring current and radiation belts. For a more detailed explanation of the three adiabatic invariants and particle motions in magnetic fields, see *Baumjohann and Treumann* (1996).

2.3.2 Acceleration of Particles

Acceleration of particles in the inner magnetosphere implies the violation of one or more of the adiabatic invariants (*Baumjohann and Treumann*, 1996). Violation happens when changes in the electromagnetic field align with the timescales of invariant periodic motions. For electrons, the gyration frequency is on the order of kHz, the bounce frequency is on the order of Hz, and the drift frequency is on the order of mHz (*Millan and Baker*, 2012). Typically, fluctuations in the electromagnetic field are associated with plasma waves, which impact electrons differently based on their frequency. Figure 2.8 demonstrates a schematic map of the equatorial plane occurrence of different magnetospheric waves that are most important to radiation belt electrons.

The radiation belt electrons are categorized into three main populations based on energy. The source population with energies from 30 - 200 keV originates from substorm injections and global convection transporting low-energy electrons from the tail towards Earth, where they are energized through adiabatic heating. The seed population has energies from 200 - 500 keV and also originates from substorm injections and inward transport by convection. In the inner magnetosphere, they are further accelerated by waves generated by the source particles. This population acts as a crucial seed for relativistic energies (> 500 keV), as substorms and global convection cannot directly inject MeV electrons into the inner magnetosphere. For more details on different populations, see, e.g., *Koskinen and Kilpua* (2022).

Global Mechanisms

The acceleration of particles in the radiation belt can be divided into global and local mechanisms. The global mechanisms refer to the radial transport of electrons across magnetic L-shells due to the violation of the third adiabatic invariant. If the electron is moved radially inward toward a stronger magnetic field, its velocity perpendicular to the magnetic field will increase due to the conservation of the first adiabatic invariant. For electrons with equatorial pitch angles below 90°, this further implies that their pitch angle will be increased towards 90° as they diffuse inward.

For radial diffusion to be efficient, global fluctuations that resonate with a multiple of the particle's drift frequency are needed. ULF waves, specifically those with frequencies in the mHz range, are natural drivers (*Millan and Baker*, 2012; *Koskinen and Kilpua*,

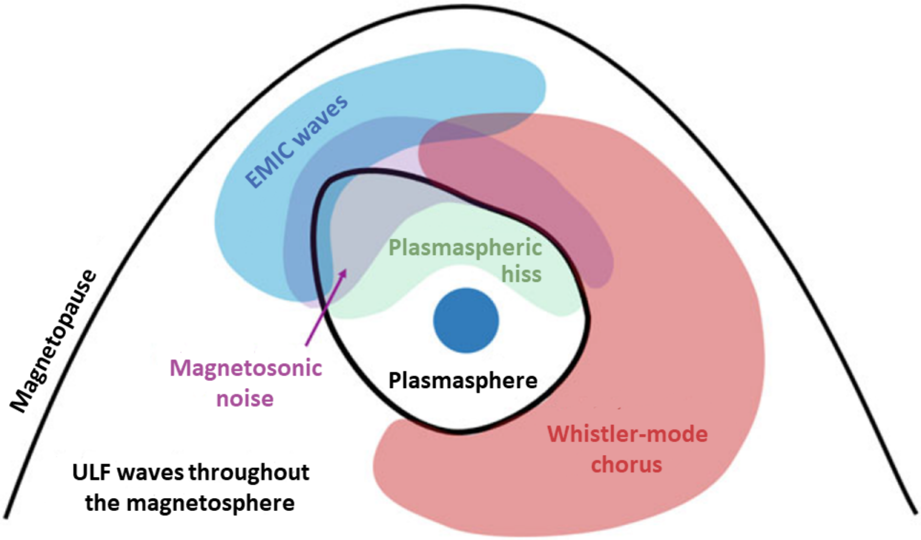

Figure 2.8: Schematic map of the equatorial occurrence of wave modes most important to the radiation belt electrons. The occurrence of different modes depends on magnetospheric activity and available energy. E.g., chorus and EMIC waves can be observed at all local times but are most frequent in the indicated domains. Taken from *Koskinen and Kilpua* (2022).

2022). These waves can be generated both externally and internally by solar wind-magnetopause interactions. Different perturbations in the solar wind, such as pressure pulses hitting the magnetopause, Kelvin–Helmholtz Instabilities caused by large velocity shear across the magnetopause (*Chen and Hasegawa*, 1974), and Flux Transfer Events at the dayside magnetopause due to reconnection (*Russell and Elphic*, 1979) can lead to ULF oscillations in the magnetosphere. Plasma instabilities in sheaths and shocks can also drive waves. Internally, the waves are driven by, e.g., ions injected by substorms (*James et al.*, 2016).

Local Mechanisms

Local acceleration of trapped electrons is driven by wave-particle interactions that occur through gyro-resonance, where the electron's gyration orbit resonates with the wave frequency. This process disrupts the conservation of the first adiabatic invariant, facilitating the acceleration (or deceleration) of the electrons. Whistler-mode chorus waves are Very-Low Frequency (VLF) waves of 0.5 − 10 kHz. The broad frequency range of their emissions allows gyro-resonant interactions across a wide spectrum of electron energies. These interactions have been demonstrated to efficiently accelerate electrons from several 10s of keV to MeV energies (*Summers et al.*, 1998). Whistler-mode chorus waves are generated by anisotropic velocity distributions of source electrons as they are injected and transported from the magnetotail to the inner magnetosphere (*Koskinen and Kilpua*, 2022). They are primarily found from dusk to noon outside of the plasmasphere, with the strongest occurrence at dawn (see Figure 2.8).

Determining the most dominant electron acceleration processes in the magnetosphere, whether local acceleration by whistler-mode chorus waves or inward radial transport driven by ULF waves, remains a highly active and contentious area of research. The complexity of interactions and the lack of a consistent correlation between these processes make it challenging to generalize their effects. *Horne et al.* (2005) revealed that radial diffusion alone could not account for the observed levels of radiation belt fluxes. They found that local acceleration by chorus waves, contrary to previous theories, is a more effective mechanism, significantly enhancing electron energies within one to two days. More recent advancements in multi-satellite observations and computer simulations have provided insights into these mechanisms but with heterogeneous results. A plausible scenario is that acceleration happens due to a combination of both global and local mechanisms where their efficiency is energy-dependent. E.g., *Jaynes et al.* (2018) and *Zhao et al.* (2019) suggest that electrons are first accelerated by chorus waves to MeV energies and then further accelerated to ultra-relativistic energies through inward diffusion by ULF waves.

2.3.3 Loss Processes

Observations have shown that radiation belt electron fluxes can be substantially depleted on timescales of days, hours, or even minutes. There are two main loss processes of radiation belt electrons: magnetopause shadowing, where electrons are lost through the magnetopause, and wave-particle interactions scattering the electrons into the atmospheric loss cone. This latter process directly corresponds to energetic electron precipitation (EEP), the central focus of this thesis.

Magnetopause Shadowing

Magnetopause shadowing can happen through three main scenarios, often occurring simultaneously. These include inward magnetopause deformations due to Kelvin–Helmholtz Instabilities and Flux Transfer Events, compression by solar wind pressure, and outward electron displacement by strong ring current enhancements. These scenarios can cause an overlap of electron drift orbits with the magnetopause, leading to flux drop-outs of outer radiation belt electrons, as depicted in Figure 2.9.

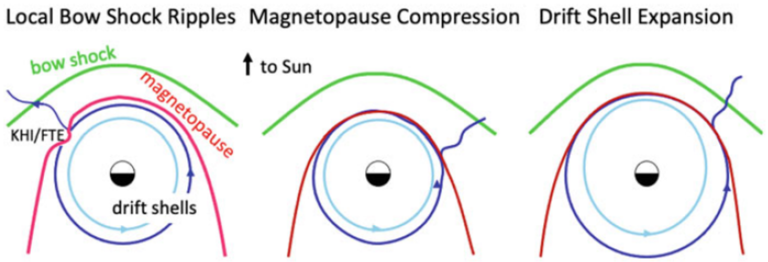

Figure 2.9: Schematic of three different scenarios of magnetopause shadowing. The left demonstrates local perturbations of the magnetopause, the middle demonstrates a strongly compressed magnetopause, and the right shows inflated electron drift orbits. Taken from *Koskinen and Kilpua* (2022).

Pitch-Angle Scattering

The most crucial factor for electron precipitation from the radiation belts into Earth's atmosphere is pitch-angle scattering into the atmospheric loss cone due to wave-particle interactions. The pitch angle (α) changes along a particle's bounce trajectory and is generally referenced at the geomagnetic equator (α_{eq}). If an electron has a $\alpha_{eq} = 90°$, it will be locally trapped at the equator. Electrons with $\alpha_{eq} < 90°$ will have a velocity component parallel to the magnetic field line. The smaller the α_{eq}, the higher the parallel velocity of the electron. Smaller α_{eq} implies that electrons will travel further along the magnetic field line and reach closer to Earth before mirroring. Electrons with mirror points at about 100 km altitude or below are considered lost to the atmosphere as they will lose energy in collisions with atmospheric gases.

Figure 2.10 shows the Loss Cone (LC) or Bounce Loss Cone (BLC), which describes the angle (α_{LC}) corresponding to a mirror point at ~100 km altitude. Electrons where $\alpha < \alpha_{LC}$ are considered lost to the atmosphere. Geographically, the BLC varies with latitude and longitude due to geomagnetic field variations. Over a drift period, the largest α_{LC} corresponds to the Drift Loss Cone (DLC) and is denoted as α_{DLC}. The South Atlantic Anomaly (SAA), a weak spot in the geomagnetic field, is an example of a region where radiation belt electrons will have a larger local α_{LC} (*Rodger et al.*, 2013). In this region, the inner radiation belt is at its closest to Earth's surface (*Nasuddin et al.*, 2019).

Figure 2.8 showed a schematic map of the different magnetospheric waves. Though ULF and whistler-mode chorus waves are found to be the main drivers of electron acceleration, practically all waves depicted can contribute to pitch angle scattering and loss of outer radiation belt electrons. The different waves' ability to scatter electrons depends on the electron's energy and equatorial pitch angle.

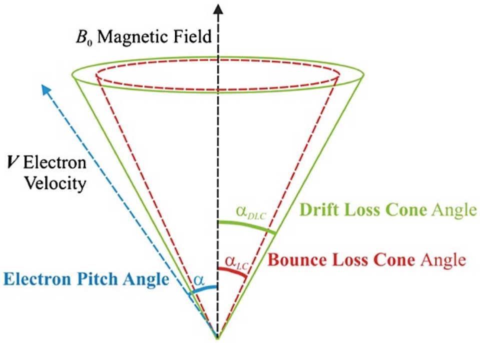

Figure 2.10: Schematic of the atmospheric loss cone where α is the electron pitch angle, α_{LC} is the angular width of the local bounce loss cone, and α_{DLC} is the angular width of the drift loss cone defined by the largest α_{LC} over a particle's drift orbit. Particles where $\alpha < \alpha_{LC}$ are considered lost to the atmosphere. Taken from *Rodger et al.* (2013).

Plasmaspheric hiss are whistler-mode emissions confined to the plasmasphere. They play a crucial role in scattering a wide range of electron energies into the atmospheric loss cone. As previously mentioned, they are responsible for the formation of the slot region between the inner and outer electron radiation belts. Their frequencies range from a few 10s of Hz to a few kHz, which is below the local electron gyro frequencies in the plasmasphere. The origin of hiss remains unclear, though local generation within the plasmasphere, terrestrial lightning strikes, and chorus waves penetrating into the plasmasphere are the current suggested mechanisms (*Koskinen and Kilpua*, 2022). Hiss can scatter electrons ranging from 100s of keV to 1 MeV into the atmospheric loss cone and can also affect electrons over 1 MeV, although at a slower rate (*Millan and Thorne*, 2007; *Koskinen and Kilpua*, 2022).

Whistler-mode chorus waves play a crucial role in scattering processes as well as acceleration. Outside of the plasmasphere, where the plasma is hotter and less dense, whistler-mode chorus waves are closer to the electron gyrofrequency than hiss waves. As source electrons give rise to chorus waves, they can get scattered to the atmospheric loss cone. At higher energies, such as the seed population, the chorus waves can either accelerate electrons, as described earlier, or they can lead to pitch angle scattering through gyro resonance. At equatorial latitudes, they are efficient in scattering electrons with energies less than about 100 keV, while the scattering of up to MeV electrons happens at higher latitudes (*Millan and Thorne*, 2007; *Koskinen and Kilpua*, 2022). Electron microbursts are intense, brief instances of electron precipitation from the magnetosphere, induced by the interaction with lower-band chorus waves characterized by short, nonlinear rising tone emissions. Microbursts, occurring within milliseconds, span energies from a few 10s of keV to several MeV and have been found to significantly deplete the outer radiation belt within timescales of one day (*Bortnik et al.*, 2008).

Electromagnetic Ion Cyclotron (EMIC) waves operate within the frequency range of 0.1 to 5 Hz, sitting below the ion gyrofrequency but above the lower part of the ULF range. They are generated by the temperature anisotropy of ions and are predominantly observed in the afternoon sector near and beyond the plasmapause. EMIC waves mainly interact with protons but also engage in gyro-resonant interactions with electrons in the MeV range. Especially during geomagnetic storms, they effectively contribute to the depletion of ultra-relativistic electrons in the radiation belts (*Summers et al.*, 1998).

Equatorial magnetosonic noise are waves in the Hz to a few 100s Hz range that are also driven by proton distributions in the ring current. They occur primarily at noon to dusk inside and outside of the plasmasphere. These waves interact with a wide range of electron energies through Landau and bounce resonances. EMIC and hiss waves can also interact with electrons through bounce resonance, and all mentioned waves can interact through Landau resonance (see Table 6.3 in *Koskinen and Kilpua* (2022)). Landau resonance occurs when particles moving parallel to the wave's propagation direction at speeds close to its phase velocity exchange energy, which causes either acceleration or damping.

2.3.4 The Influence of Solar Wind Drivers

Significant fluctuations in the electron fluxes of the radiation belts are linked to large-scale solar wind structures, which trigger geomagnetic storms and substorms. These structures, with their distinct properties, initiate gain, acceleration, and loss processes within the radiation belts. While CMEs and HSSs influence the entire spectrum of radiation belt dynamics, their impact and effectiveness differ.

The flow of energy from the solar wind to the magnetosphere is highly dependent on dayside reconnection (e.g., *Newell et al.*, 2007). Along with density and IMF direction, solar wind speed determines the pressure exerted on the magnetosphere and the dayside merging rate. A southward component of the IMF drives much of the magnetospheric dynamics and induces the transport of electrons from the tail to the inner magnetosphere. Solar wind speed has been found to be a good predictor of substorms leading to a bursty energy dissipation of tail electrons (*Newell et al.*, 2016). The loading of the flux in the magnetotail needed to initiate a substorm is often associated with a change in the southward IMF component to northward (*Freeman and Morley*, 2004; *Newell and Liou*, 2011). *Liou et al.* (2018) investigated the characteristics of substorms that occurred during CMEs and HSSs and found that substorms are frequent for both structures but that CMEs were associated with the most intense substorms.

CMEs and their shocks and sheaths are generally associated with strong geomagnetic storms with the assumption of substantial negative B_z. Shocks can abruptly compress the magnetopause and are, hence, usually good drivers of acceleration and inward diffusion of radiation belt electrons by ULF waves (e.g., *Kanekal et al.*, 2016). The following sheaths have been found to effectively cause depletion of radiation belt electrons over a wide range of L-shells (*Kilpua et al.*, 2015) due to both magnetopause shadowing and wave enhancements (*Kalliokoski et al.*, 2020). Their effectiveness is due to their high dynamic pressure and large amplitude IMF variations. If the magnetic structure of a CME points southward, it is considered to be geoeffective. This can lead to large amounts of energy transfer from the solar wind to the magnetosphere, causing both acceleration and loss processes, though not as efficiently as sheaths (*Kilpua et al.*, 2015). Considering the acceleration of electrons over a wide range of L-shells, CMEs have been found to be very efficient compared to HSSs (e.g., *Yuan and Zong*, 2012).

HSSs and their associated CIRs are known to cause moderate geomagnetic disturbances over longer timescales than those associated with CMEs. CIRs are similar to sheaths in that they have high dynamic pressure and highly fluctuating north-south IMF components. The amplitude of the fluctuations is usually smaller than those of sheaths, and hence, CIRs are associated with less pronounced loss mechanisms. HSSs are considered more effective in enhancing relativistic electron populations at geostationary orbit in the radiation belts than CME-driven storms but are found to lack properties that effectively cause losses (*Kilpua et al.*, 2015).

The link between high solar wind speed and increased relativistic electron fluxes at geostationary orbit has been known since the 1970s (*Paulikas and Blake*, 1979). However, their relationship is not necessarily linear. *Reeves et al.* (2011) found that while high solar wind speeds imply a larger probability of high flux enhancements, such enhancements could be found for a large variety of solar wind speeds. Others have pointed to the importance of a negative southward IMF component for the acceleration of electrons in the radiation belts (*Blake et al.*, 1997; *Li et al.*, 2011). Without a sufficient southward component, magnetospheric substorm activity does not occur, further resulting in a lack of seed particles, chorus waves, and acceleration of particles.

Pre-storm fluxes have also been shown to have an effect on the radiation belt responses. *Kilpua et al.* (2015) found that CMEs and CIRs followed by high-speed solar winds that depleted electron fluxes were associated with higher pre-storm fluxes, while those efficient in accelerating had lower pre-storm fluxes. The timing of the different solar wind structures during a solar cycle has also been shown to have an effect on their contribution to loss processes. *Asikainen and Ruopsa* (2016) looked at annual flux data and found that both CMEs and HSSs were most efficient in producing energetic electron precipitation in the declining phase of a solar cycle, likely due to the general increase in the background solar wind speed. Though HSSs contribute more to the annual precipitating fluxes, CMEs were found to have the highest fluxes (*Asikainen and Ruopsa*, 2016).

3 The Polar Atmosphere and Energetic Particle Precipitation

In the previous chapter, the complex dynamics between the solar wind and magnetosphere, along with the wave-particle interactions that drive EEP, were introduced. This section will explore the atmospheric impact of EPP with a focus on EEP. As particles scatter into the atmospheric loss cone, they deposit energy through several observable effects in the middle and upper atmosphere. The most commonly known effect is the auroras, but EPP also leads to ionization of the neutral atmosphere, altering its chemical composition and dynamics. Most importantly, EPP adds to the enrichment of odd nitrogen (NO_x: NO, NO_2) and odd hydrogen (HO_x: H, OH, HO_2) gases. These highly reactive species play an important role in atmospheric chemistry, particularly due to their catalytic role in ozone depletion.

While solar irradiance predominantly dictates global climatic circulations and atmospheric chemistry, the influence of EEP, though lesser in magnitude, is acknowledged as a significant component of the natural solar forcing. This recognition has led to its incorporation into chemistry-climate models such as the Coupled Model Intercomparison Project Phase 6 (CMIP6) (*Matthes et al.*, 2017; *Funke et al.*, 2024). Differences in data processing, ionization rate calculations, and the modeling of background atmospheres result in a broad range of electron ionization rates. However, a general consensus is that the electron forcing is underestimated in current models (*Nesse Tyssøy et al.*, 2022; *Sinnhuber et al.*, 2022; *Funke et al.*, 2024). Hence, the full scope of EEP's impact on atmospheric chemistry and its broader implications remain unresolved, marking it a highly active field of ongoing research.

Section 3.1 starts by introducing the key concepts and mechanisms driving polar atmospheric dynamics. Section 3.2 provides an overview of how particle precipitation, particularly EEP, influences these dynamics. Lastly, Section 3.3 presents the current methods for parameterizing radiation belt electron precipitation and the challenges faced by the scientific community in accurately representing these processes.

3.1 Polar Atmospheric Dynamics

The atmosphere is a complex and dynamic system characterized by interconnected temperature variations, wind patterns, and wave propagation. Changes in any one aspect

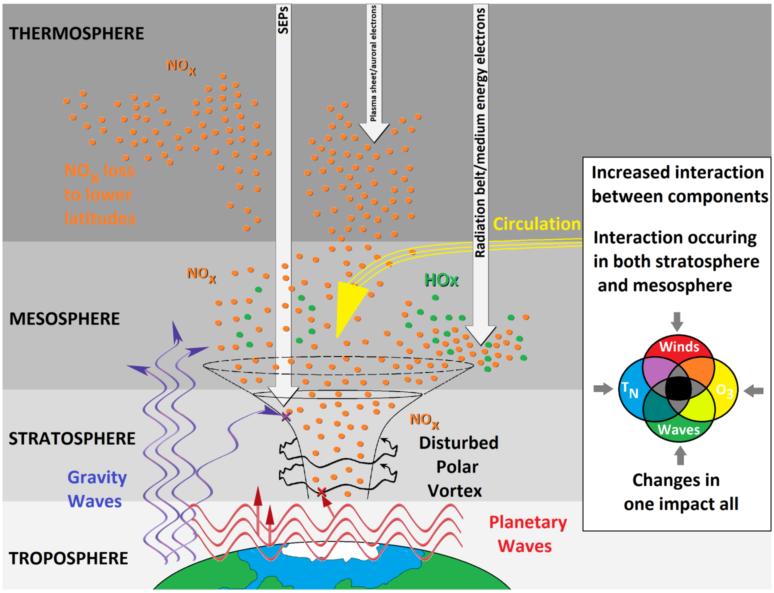

Figure 3.1: A schematic illustrating the atmospheric processes that can contribute to the chemical-dynamical coupling of the winter polar atmosphere. Solar energetic protons (SEPs in the figure), plasma sheet electrons, and radiation belt electron precipitation are shown to create NO_x and HO_x at different altitudes. The general circulation transports these gases to lower altitudes within the polar vortex, where they can alter ozone concentration and, subsequently, temperature, winds, and waves. These variations will have an effect on the strength of the polar vortex. Additionally, planetary and gravity waves are shown to disrupt the polar vortex. Taken from *Edvartsen, Jone Øvretvedt* (2023).

can significantly impact the overall atmospheric equilibrium. Particularly in the polar regions, the role of EPP plays a part in modulating the chemical and dynamic interactions within the atmosphere. Figure 3.1 offers an overview of the mechanisms that can contribute to the chemical-dynamical coupling of the winter polar atmosphere. This section will introduce these processes, highlighting the influence of EPP on the atmospheric system and clarifying its broader implications.

3.1.1 The Polar Vortex and Atmospheric Waves

The stratospheric polar vortex comprises a vast region of air encircled and maintained by a powerful planetary-scale westerly (west to east) wind or jet stream known as the polar night jet. The vortex exists from fall to spring in both hemispheres due to the large-scale temperature gradients between mid and polar latitudes. It forms in the fall, when there is no solar heating in polar regions, strengthens during winter, and then breaks down as sunlight returns in spring, causing the high-latitude winds to become weaker easterlies (*Waugh et al.*, 2017). The vortex extends from the tropopause, up through the strato-

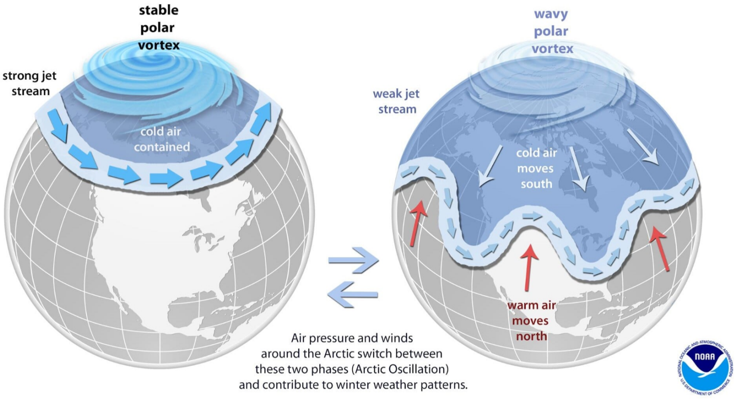

Figure 3.2: Schematic of a stable (left) and disturbed (right) polar vortex. The stable vortex contains cold air within the pole, while, if disturbed, cold air is released to lower latitudes. The manifestation of air from the poles can lead to colder and dryer winters in the NH. Taken from the National Oceanic and Atmospheric Administration (NOAA) website.

sphere, and into the lower mesosphere. The air inside the polar vortex is associated with low pressure and cold temperatures. During stable conditions, the cold air is confined to the poles, while disturbances can cause the polar vortex to become unstable or even break, leading to the propagation of cold air masses to lower latitudes. Figure 3.2 shows a schematic of a stable (left) and disturbed (right) polar vortex. Disturbances in the polar vortex are attributed to atmospheric waves dissipating their energy and momentum on the westerly flow.

Large-scale perturbations of the polar vortex are often associated with planetary waves, also known as Rossby waves (*Waugh et al.*, 2017). Rossby waves result from the Earth's rotation and the variation in Coriolis force with latitude (*Brasseur and Solomon*, 2005; *Woollings et al.*, 2023). These slow-moving waves span thousands of kilometers and are often shaped by stationary geographical features, contributing to their quasi-stationary nature. Rossby waves do, however, propagate from the troposphere to the stratosphere and have a westward phase velocity against the average atmospheric flow.

Rossby wave breaking occurs when their amplitude becomes excessively large, often due to wave-wave interactions or shifts in latitudinal temperature gradients. This breaking leads to the deposition of momentum in the atmosphere as the waves dissipate. Additionally, when these waves move into regions where the background wind speed is similar to their phase speed, critical layer absorption occurs. Such processes will result in westward angular momentum being deposited to the mean flow. At polar latitudes, this implies a weakening of the polar night jet. Under strong wave influence, the increased drag on the jet can lead to large displacements, splitting (*Seviour et al.*, 2013, and reference therein), or even a complete breakdown (wind reversal) of the polar vortex (*Baldwin et al.*, 2021). Disturbances strong enough to break down the polar vortex will lead to a sudden warming of the stratosphere and cooling of the mesosphere and are referred to as Sudden Stratospheric Warmings (SSW). SSWs will impact the downwelling of airmasses inside the polar vortex, which first halts and then strongly increases when it reforms (*Baldwin et al.*, 2021).

Gravity waves are also relevant for the variability of the polar vortex (*Samtleben et al.*, 2019; *Gupta et al.*, 2021; *Yasyukevich et al.*, 2022). These vertically propagating waves have a wavelength from 10s of meters up to several 100s (*Brasseur and Solomon*, 2005). They are generated by disturbances such as airflow over mountain ranges, convective activity in the atmosphere, and weather frontal systems, where the buoyancy force acts to restore equilibrium, propagating these waves from the troposphere to the mesosphere. During winter, the stratospheric winds flow toward the east and filter out gravity waves with similar phase speed. The amplitude of gravity waves grows exponentially with altitude until it becomes unstable and breaks, usually around upper stratospheric and lower mesospheric altitudes. As such, gravity waves during winter will deposit westward angular momentum to the mean flow of the upper polar vortex, giving rise to instabilities.

Atmospheric waves also drive a large-scale circulation pattern in the stratosphere and mesosphere, called the Brewer-Dobson circulation (*Plumb*, 2002). The Brewer-Dobson circulation plays a crucial role in atmospheric dynamics, characterized by the upwelling and subsequent adiabatic cooling within the tropical stratosphere, alongside downwelling accompanied by adiabatic heating at the polar regions (*Salby and Callaghan*, 2002). This circulation pattern is also pronounced in the mesosphere, where downwelling and heating processes are intensified at the winter pole, leading to a warmer polar winter mesosphere compared to its summer counterpart (*Garcia and Solomon*, 1985). Additionally, this dynamic facilitates a general descent of chemical trace gases from the mesosphere to lower altitudes. The resulting temperature and wind patterns influence wave activity, which, in turn, contributes to further variations in temperature and winds. This feedback loop between wind and wave activity is called wave-mean-flow interaction (*Andrews et al.*, 1987) and can further influence the strength of the polar vortex.

The strength of the polar vortex is also known to be affected by the Quasi-Biennial Oscillation, which can modulate the propagation of atmospheric waves from midlatitudes to the polar stratosphere (*Baldwin and Dunkerton*, 2001). It is a roughly 28-month east-west oscillating wind. When easterly, it can guide waves into the polar stratosphere, leading to disturbances of the polar vortex (e.g, *Baldwin and Dunkerton*, 2001; *Watson and Gray*, 2014).

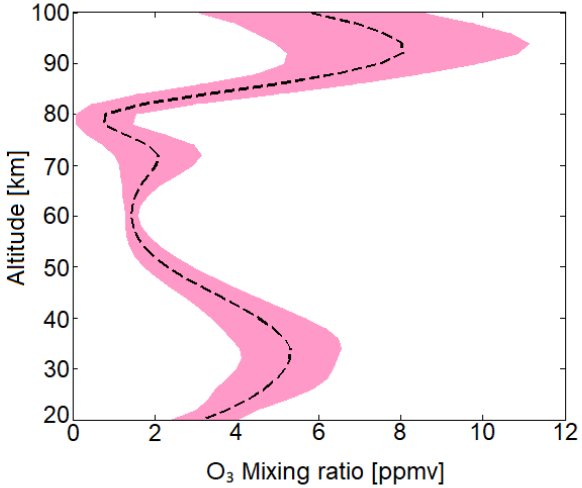

Figure 3.3: Sample of the night time ozone mixing ratio profile in the polar NH at 60° – 90° latitude over the year 2003. Calculations are made from the GOMOS measurements. Three local ozone maxima are visible: The primary ozone maximum at about 30 km, the secondary maximum at about 90 km, and the tertiary ozone maximum at about 70 km. The tertiary ozone maximum is found only during the polar winter. The black dashed line shows the average, and the pink shaded area shows the standard deviation. Taken from *Seppälä, Annika* (2007).

3.1.2 The Role of Ozone

Polar stratospheric temperatures and winds also depend on ozone concentration. Ozone is primarily produced when UV radiation splits molecular oxygen, allowing atomic oxygen to combine with molecular oxygen (*Brasseur and Solomon*, 2005). Concentrated mainly in the stratosphere, between 10 to 50 km altitude, ozone serves as a protective barrier by absorbing most of the Sun's UV radiation. This not only protects life from UV damage but also regulates the atmosphere's thermal structure. Ozone converts the incoming UV radiation into thermal energy, efficiently heating the stratosphere from the top down. In the absence of sunlight, the stratosphere cools as ozone releases stored energy via infrared radiation. As such, it is commonly known that stratospheric temperature correlates with ozone levels (e.g., *Randel and Wu*, 1999; *Langematz et al.*, 2003). Consequently, any changes in ozone concentration will either have a warming or cooling effect.

The average ozone mixing ratio over the polar NH is illustrated in Figure 3.3. In addition to the primary ozone layer at approximately 30 km, there is a secondary maximum around the mesopause at about 90 km and a tertiary maximum at around 70 km. The latter is only present during polar winter. Generally, a loss in ozone concentration will lead to a net cooling in the presence of sunlight and a net warming in the lack of sunlight. During the polar winter, when the stratosphere and mesosphere receive little to no sunlight, observational and modeling studies have shown that EEP-induced ozone loss leads to a net warming in the polar mesosphere and upper stratosphere and a net cooling in the lower stratosphere (e.g., *Langematz et al.*, 2003; *Baumgaertner et al.*, 2011; *Sinnhuber et al.*, 2018). The stratospheric temperature changes related to the loss of ozone are expected to enhance the polar vortex. This effect has been hypothesized to be particularly important during disturbed vortex conditions (*Asikainen et al.*, 2020, and references therein).

EPP is identified as a major source of NO_x and HO_x gases (*Crutzen et al.*, 1975; *Solomon et al.*, 1981), which play an important part in the atmospheric chemistry of the polar regions, acting as catalysts for the depletion of stratospheric and mesospheric ozone. Though both NO_x and HO_x are known to have destructive effects on ozone (e.g., *Sinnhuber and Wieters*, 2012), NO_x is particularly important due to its long lifetime of several weeks during polar winter darkness (*Solomon et al.*, 1982). It is also during polar winter that the polar vortex confines NO_x to high latitudes, allowing the transport of NO_x down through the atmosphere by the Brewer-Dobson circulation. The EPP-induced depletion has far-reaching effects, including altering the thermal structure of the atmosphere and influencing the dynamics of the polar vortex, which in turn can impact ground-level temperature and winter weather patterns (e.g., *Baldwin and Dunkerton*, 2001; *Sinnhuber and Wieters*, 2012; *Seppälä et al.*, 2013; *Kidston et al.*, 2015; *Maliniemi et al.*, 2016). The efficiency of EPP-induced ozone depletion largely relies on particle precipitation within ozone-rich regions. Differences in the type and energy of EPP will lead to various atmospheric impacts due to their differences in flux and ability to reach different altitudes.

3.2 Impact of Energetic Particle Precipitation

Figure 3.4 shows a schematic of the ionization profiles for different types of EPP in the Earth's atmosphere. The penetration depth of energetic particles into the atmosphere depends on their energy, with higher energy particles reaching deeper. The most energetic particle precipitation is associated with galactic cosmic rays and solar protons.

Galactic cosmic rays, originating beyond the solar system, are predominantly high-energy protons with energies ranging from 10 MeV to 10^{15} MeV (*Mironova et al.*, 2015). Capable of ionizing the atmosphere down to the troposphere, they play a role in atmospheric chemistry, typically precipitating at altitudes of 3 to 60 km (*Mironova et al.*, 2015). Although their flux remains relatively stable, it fluctuates slightly with solar activity, as

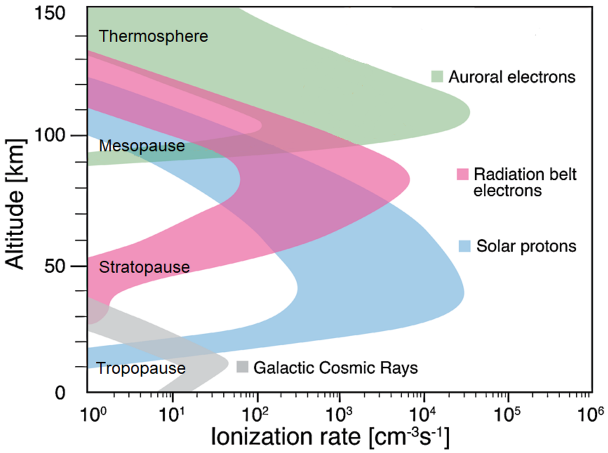

Figure 3.4: A schematic of the various types of energetic particle precipitation into Earth's atmosphere and the altitude profile of their ionization rate. The boundaries of the atmospheric layers are also shown. Note that the upper boundary of the thermosphere is beyond the indicated range in the figure. Modified from *Mironova et al.* (2015). Originally from *Baker et al.* (2012).

the Sun's magnetic field acts as a shield against these cosmic rays. Compared to other types of particle precipitations, their ionization rate is low.

Solar Proton Events (SPE) involve the precipitation of protons with energies predominantly exceeding 10 MeV (*Mironova et al.*, 2015). These events, characterized by large proton fluxes, are closely associated with solar flares and CMEs, and their intensity often escalates with the speed of the solar wind (*Borovsky and Denton*, 2006). SPEs occur sporadically over the solar cycle. The protons primarily precipitate over the entire polar cap, limited in latitude by the particle energy and the strength of the magnetospheric field (*Nesse Tyssøy et al.*, 2013; *Nesse Tyssøy and Stadsnes*, 2015). Their high energies enable them to reach deep into the stratosphere. Upon entry, they produce intense amounts of HO_x and NO_x that can directly affect mesospheric and stratospheric ozone concentrations. The impact of these sporadic and infrequent SPEs on the reactive atmospheric species and ozone levels has been extensively studied (e.g., *Jackman et al.*, 2005; *Funke et al.*, 2011; *Seppälä et al.*, 2008; *Nesse Tyssøy et al.*, 2013; *Nesse Tyssøy and Stadsnes*, 2015; *Zawedde et al.*, 2018).

EPP at higher altitudes primarily involves electron precipitation, though less energetic protons from the inner magnetosphere also contribute. Figure 3.5 shows a detailed distribution of ionization rates for a wide range of EEP energies. The lowest energy EEP is associated with the frequent and abundant auroral electrons. These electrons originate predominantly from the plasma sheet and have energies ranging from one to around 30 keV (*Newell et al.*, 2004; *Khazanov and Glocer*, 2020). They primarily deposit

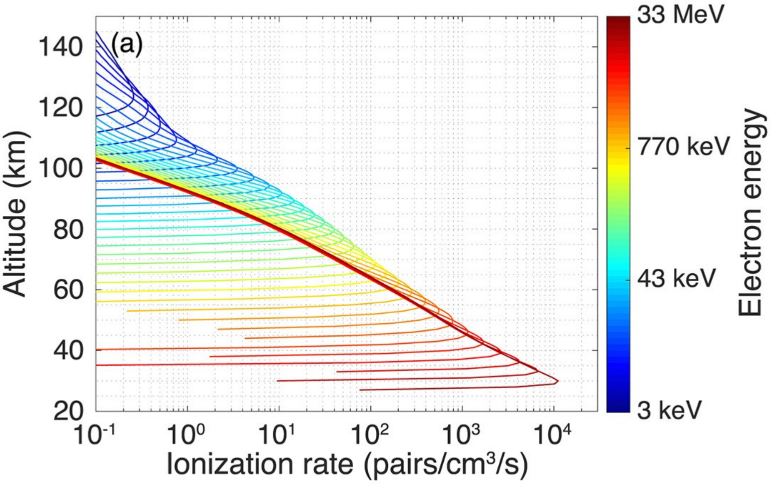

Figure 3.5: The calculated ionization rates at altitudes ranging from 20 to 150 km, induced by monoenergetic electron beams precipitating vertically into the atmosphere from a starting altitude of 500 km. The figure shows results for electron energies distributed between approximately 3 keV and 33 MeV. A roughly linear relationship between the penetration depth and the logarithmic value of the incident electron energy is evident. Taken from *Xu et al.* (2020).

their energy into the lower thermosphere and upper mesosphere, creating vivid auroras and leading to frequent and abundant NO_x production. The radiation belt electrons have energies from 30 keV to relativistic energies, producing both NO_x and HO_x throughout the mesosphere and at the top of the stratosphere.

Auroral electrons have been extensively studied and are commonly found to correlate with geomagnetic indices such as the auroral electrojet indices AE and SME (e.g., *Newell and Gjerloev*, 2014) or the global Kp index (e.g., *Zhang and Paxton*, 2008). They also correlate with solar wind conditions such as IMF direction (e.g., *Milan et al.*, 2010). Additionally, their effects on NO_x are fairly well established (e.g., *Marsh et al.*, 2004; *Sinnhuber et al.*, 2011; *Sinnhuber and Wieters*, 2012).

In the absence of solar photodissociation processes, auroral precipitation leads to significant increases in NO_x concentrations in the lower thermosphere around 100 km altitude (e.g., *Marsh et al.*, 2004; *Sinnhuber et al.*, 2011). This is visible in Figure 3.6, which shows the NO density profiles in the SH from 2007 to 2014. At around 100 km, a NO reservoir is visible throughout the entire year but is especially strong during the SH winter months. The polar winter's residual circulation plays a crucial role in dynamically transporting NO_x from higher to lower altitudes within the lower mesosphere and upper stratosphere. At these altitudes, EEP-induced NO_x can significantly contributes to ozone depletion (e.g., *Solomon et al.*, 1982; *Damiani et al.*, 2016; *Maliniemi et al.*, 2021).

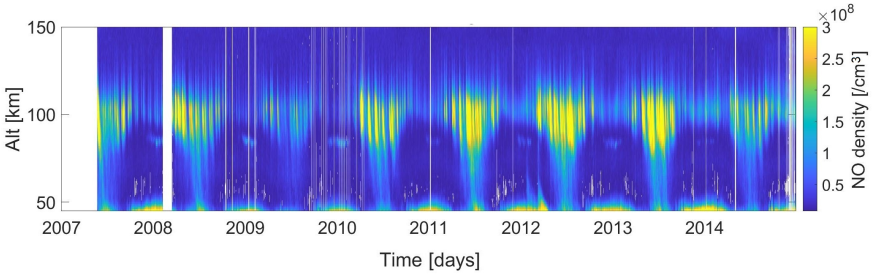

Figure 3.6: SH NO density profile from 2007 to 2014. The NO data is from the SOFIE instrument onboard the AIM satellite. An NO reservoir at around 100 km due to the frequent auroral precipitation is especially evident during SH winter. Additionally, NO density increase from reservoir altitudes down to the stratosphere is visible. This is due to the transport or indirect effect of EEP, but direct production can also contribute. Taken from Paper II.

The compositional changes in ozone due to the downward transportation of NO_x are known as the indirect effect of EEP, with auroral precipitation being the primary source (*Randall et al.*, 2007; *Smith-Johnsen et al.*, 2017). The decent of NO during the polar winter is evident in Figure 3.6, highlighting its impact.

The radiation belt electrons can precipitate to lower mesospheric and upper stratospheric altitudes where the production of NO_x can have a direct impact on ozone concentrations, known as the EEP direct effect (*Randall et al.*, 2007; *Smith-Johnsen et al.*, 2017). However, their significance has been debated in several studies (*Clilverd et al.*, 2009; *Sinnhuber et al.*, 2011, 2014; *Newnham et al.*, 2011; *Daae et al.*, 2012; *Kirkwood et al.*, 2015; *Randall et al.*, 2015). The uncertainty lies in knowledge gaps that stem from limited particle measurements, scarce NO observations in the polar atmosphere, and the significantly lower fluxes compared to auroral precipitation. Nonetheless, recent research indicates that even weak fluxes of this higher energy precipitation can markedly impact atmospheric chemistry and dynamics under specific atmospheric conditions (*Smith-Johnsen et al.*, 2017; *Asikainen et al.*, 2020; *Zúñiga López et al.*, 2022). Still, a better understanding of radiation belt electron precipitation is needed to quantify its impact and relevance on atmospheric dynamics accurately.

Recent research, including the papers in this thesis, has aimed at enhancing our understanding of the higher energy spectrum of EEP, or more specifically, the Medium Energy Electrons (MEE) with energies from 30 keV to 1 MeV. MEE precipitation deposits its energy in the lower mesosphere and upper stratosphere at around 90 to 50 km altitude (*Xu et al.*, 2020; *Nesse Tyssøy et al.*, 2022; *Pettit et al.*, 2023), between 55 – 70° corrected geomagnetic (CGM) latitude (e.g., *Babu et al.*, 2022). The overarching goal is to achieve a more accurate parameterization of MEE precipitation for integration into chemistry-climate models. This will allow for a comprehensive assessment of EEP's atmospheric impacts. The next section will discuss the current parameterization of MEE precipitation recommended for chemistry-climate models and outline its benefits and limitations, as well as the community's efforts to improve it.

3.3 Parameterizing Medium Energy Electron Precipitation

Measuring precipitating MEE fluxes is not straightforward due to several challenges. Unlike the more uniform distribution observed in SPEs, electron precipitation is characterized by variations across magnetic latitudes and Magnetic Local Time (MLT), influenced by the dynamics of the inner magnetosphere and wave-particle interactions. Furthermore, there is a lack of continuous observational data from instruments capable of monitoring within the BLC and across the energy spectrum of MEE precipitation (*Rodger et al.*, 2010). These challenges make it hard to measure MEE precipitation accurately.

MEE precipitation can be measured either by in situ particle detectors on satellites or indirectly by balloon observations, ground-based instruments, and space-based measurements from satellites. Ground-based riometers use the changes in cosmic radio noise absorption in the ionosphere to measure the enhancement of electron concentration caused by EEP and respond to the whole bounce loss cone energy spectrum (e.g., *Rodger et al.*, 2013). Similarly, incoherent scatter radars use the scattering of radio waves by the ionosphere's free electrons and ions to observe changes in electron density due to EEP (e.g., *Juarez Madera et al.*, 2023). Balloon measurements usually include observations of bremsstrahlung X-rays that are generated during the deceleration of the precipitating electrons (e.g., *Mironova et al.*, 2019). Indirect satellite observations include X-ray and UV emissions (e.g., *Østgaard, N. and J. Stadsnes and J. Bjordal and R. R. Vondrak and S. A. Cummer and D. L. Chenette and G. K. Parks and M. J. Brittnacher and D. L. McKenzie*, 1999).

While indirect measurements are effective for detecting EEP, their capabilities are constrained by limitations such as point-based observations and coverage confined to certain latitudes and MLTs. Additionally, indirect measurements depend on assumptions and models to retrieve the fluxes and energy spectra of the particles. Particle measurements from satellites can pass over the entire MEE precipitation region in both hemispheres but are often limited by integral flux measurements and the ability for direct observations inside the BLC. The Upper Atmosphere Research Satellite (UARS) (*Winningham et al.*, 1993), the Polar Operational Environmental Satellite (POES) series, and the Electron Losses and Fields Investigation (ELFIN) twin CubeSats (*Angelopoulos et al.*, 2023), are examples of satellite missions capable of monitoring MEE precipitation within the BLC. However, the POES series stands out for its extensive, near-continuous data records dating back to 1978 until today. With several satellites (up to six) in operation that cover various MLTs, the POES series is considered an optimal option for building comprehensive, long-term analyses and developing MEE parameterizations. The MEE flux measurements from the POES satellites are used in the three papers comprising this thesis. However, using POES instruments requires careful consideration due to issues like degradation and contamination. A detailed description of the satellites and their instrumentation is provided in Chapter 4.

Over the past decade, significant efforts have been dedicated to refining MEE flux measurements and developing a MEE parameterization derived from the POES data. However, variations in data processing have led to a wide range of ionization rate estimates (e.g., *Beharrell et al.*, 2015; *van de Kamp et al.*, 2016, 2018; *Mironova et al.*, 2019; *Pettit et al.*, 2019; *Tyssøy et al.*, 2019, 2021; *Duderstadt et al.*, 2021; *Partamies et al.*, 2021; *Babu et al.*, 2022; *Zúñiga López et al.*, 2022; *Babu et al.*, 2023; *Salice et al.*, 2023; *Nesse et al.*, 2023). Figure 3.7 shows a recent study by *Nesse Tyssøy et al.* (2022) that assessed eight relevant MEE ionization rate estimates derived from POES measurements during a highly geomagnetic active period in April 2010. The figure shows that the differences in estimates are not only in intensity but also in the range and duration of the precipitating MEE fluxes. Currently, it is the ApEEP (top left) ionization rate estimates that are used as input to the chemistry-climate model CMIP6 (*Matthes et al.*, 2017). The ApEEP model builds on the daily resolved model by *van de Kamp et al.* (2016). It uses data from all the electron energy detectors on the 0° telescope, covering the period from 2002 to 2012, to provide the expected daily average flux spectra (*van de Kamp et al.*, 2016). The model is scaled by the geomagnetic daily Ap index, which can be reconstructed back to 1850 (*Matthes et al.*, 2017), enabling parameterization of MEE precipitation far beyond satellite observations.

However, *Nesse Tyssøy et al.* (2022) and *Sinnhuber et al.* (2022) found that the Ap-based model provides the lowest ionization rates and, thereby, the lowest mesospheric NO concentrations. Previous studies have also found similar results of underestimation of mesospheric and stratospheric NO$_x$ produced by the ApEEP model (*Pettit et al.*, 2019; *Tyssøy et al.*, 2019). *Tyssøy et al.* (2019) points out that the ApEEP model falls short in accurately representing flux levels during intense geomagnetic storms due to its performance plateauing for Ap values greater than 40. They also point out that the model falls short during periods of extended geomagnetic recovery phases. As such, a solar cycle bias arises due to the difference in occurrence rate for the intense CMEs and the long-lasting HSSs.

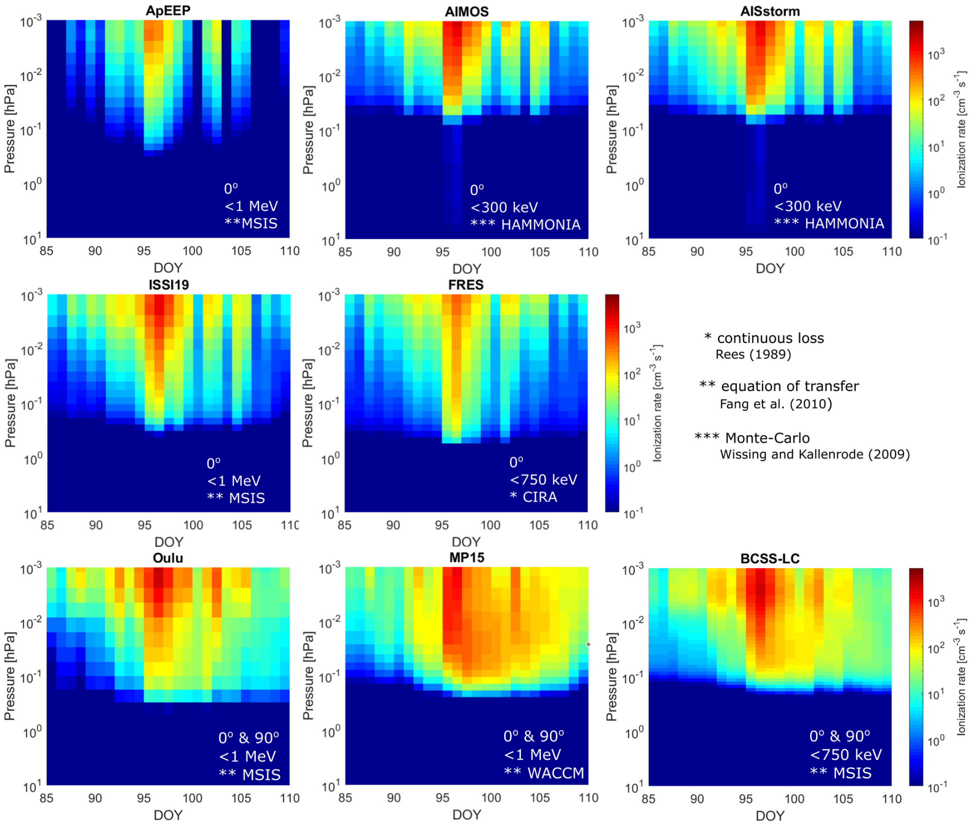

Figure 3.7: Eight different ionization rate estimates of MEE precipitation during a geomagnetic active period in April 2010. The detectors, upper energy limit, background atmosphere, and ionization rate method are listed in the legend of each panel. Taken from *Nesse Tyssøy et al.* (2022).

Tyssøy et al. (2019) suggests that the general underestimation found in the ApEEP model can be solved by using both electron detectors on the POES satellites to estimate a more accurate BLC flux. This is further highlighted by the three bottom panels of Figure 3.7 that demonstrate higher ionization rates obtained by using both telescopes. Furthermore, Figure 3.8 demonstrates that the high-energy tail ($\gtrsim$ 300 keV) of MEE precipitation behaves differently than the lower energies not only when it comes to flux level but also when it comes to timing and duration. Differences in timing have also been pointed out by *Ødegaard et al.* (2017) and *Tyssøy et al.* (2021) and are thought to be due to the extra time needed to accelerate these particles to 100s of keV in the inner magnetosphere. The differences in duration could be affected by the driving solar wind being a CME or HSS as *Longden et al.* (e.g., 2008) found longer precipitation events to be associated with HSS.

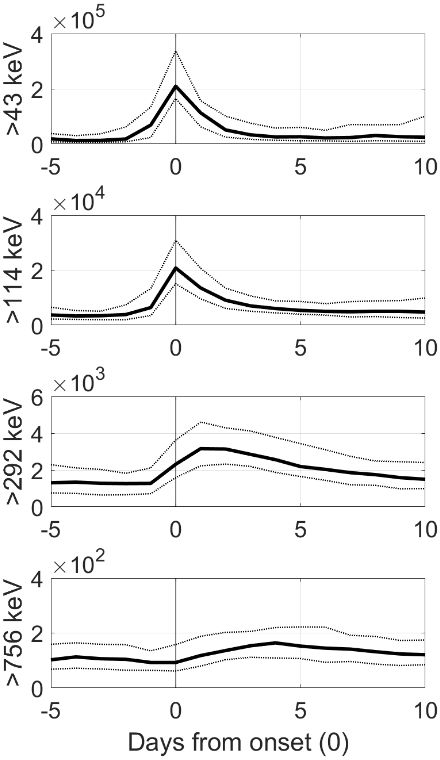

Figure 3.8: Superposed epoch analysis of daily global median electron flux evolution of 164 large flux events from 2004 – 2014. The BCSS-LC in all four electron flux channels (>43, >114, >292, and >765 keV) are shown. The dotted lines represent the 25th and 75th percentiles. Onset (0) is defined by the peak in the >43 keV flux. Flux units are in $cm^{-2}s^{-1}sr^{-1}$.

The variability within the MEE precipitation spectrum presents a challenge for accurately modeling the full MEE energy range using a single geomagnetic index. Given that most indices primarily correlate with the lower energy portions, it is not unlikely that they fail to account for the distinct characteristics of the high-energy tail. This challenge, together with the various ionization rate estimates, demonstrates the need to investigate the high-energy tail of MEE precipitation with flux estimates using both of the electron detector telescopes onboard the POES satellites.

The studies within this thesis apply the BCSS-LC dataset (the bottom right panel of Figure 3.7), where both detector telescopes are used to estimate the complete bounce loss cone flux. This approach is further explained in Chapter 4. By investigating the variations in flux response, timing, and duration across different solar wind structures and by identifying the key parameters that effectively capture high-energy tail events, this body of work aims to establish a robust foundation for the development of a stochastic MEE parameterization. The decision to adopt a stochastic approach stems from the observation that traditional geomagnetic indices do not consistently correlate well with the behaviors of the high-energy tail, forcing a probability-based assessment to more accurately capture and model the complex dynamics and variability of the MEE precipitation. Such a new parameterization could better capture the complex nuances and variations within the MEE energy spectrum than current models, thereby paving the way for improved predictions of space weather impacts on Earth's atmosphere.

4 Data and Methodology

This chapter introduces the data applied in this thesis. All papers use the BCSS-LC MEE fluxes from POES/MetOp. The following section describes the data handling that has previously been performed to achieve the precipitating fluxes from the measurements. The chapter goes on to explain how NO profiles from SOFIE on the AIM satellite are retrieved and some of the challenges associated with it. Lastly, the source of solar wind and geomagnetic data used, will briefly be mentioned.

4.1 MEPED on the POES/MetOp Satellites

The POES series from NOAA and the Meteorological Operational (MetOp) satellites from EUMETSAT, carrying the Medium Energy Proton and Electron Detector (MEPED), have been directly measuring the influx of energetic particle precipitation and particle radiation for over four solar cycles from 1978 until today. The long continuous dataset makes these satellites an invaluable resource for examining the long-term behaviors and trends in the high-energy spectrum of EPP.

These satellites operate in Sun-synchronous, low-altitude (≈ 850 km), polar orbits. They complete an orbit roughly every 100 min and achieve between 14 to 15 orbits per day (*Evans and Greer*, 2004). With the launch of NOAA-15 on the 13th of May 1998, the 5th generation of the POES/MetOp series - with an upgraded Space Environment Monitor-2 (SEM-2) package for MEPED - began. In the period of interest for this thesis (2004 to 2014), up to six satellites were in operation, all with SEM-2. Figure 4.1 shows the operational timeline of these satellites in addition to the satellite MLT coverage over mid to high NH latitudes for four different days over the eleven years. Although data scarcity is observed around the midnight sector (0 MLT), the collective MLT coverage provided by the satellites in the high-latitude polar regions is fairly good. This represents another advantage of using the POES/MetOp satellite series.

MEPED consists of two proton and two electron solid-state detector telescopes, in addition to four omnidirectional detector systems for high-energy protons. This thesis concerns electron measurements from the solid-state detector telescopes. The two MEPED electron telescopes are designed to measure MEE fluxes across three energy ranges from 30 to 2500 keV (*Evans and Greer*, 2004). The nominal lower limits are > 30 (E1), > 100 (E2), and > 300 (E3) keV. Additionally, the highest MEPED proton channel (P6), built to detect protons with energies > 6900 keV, is highly sensitive to relativistic electrons

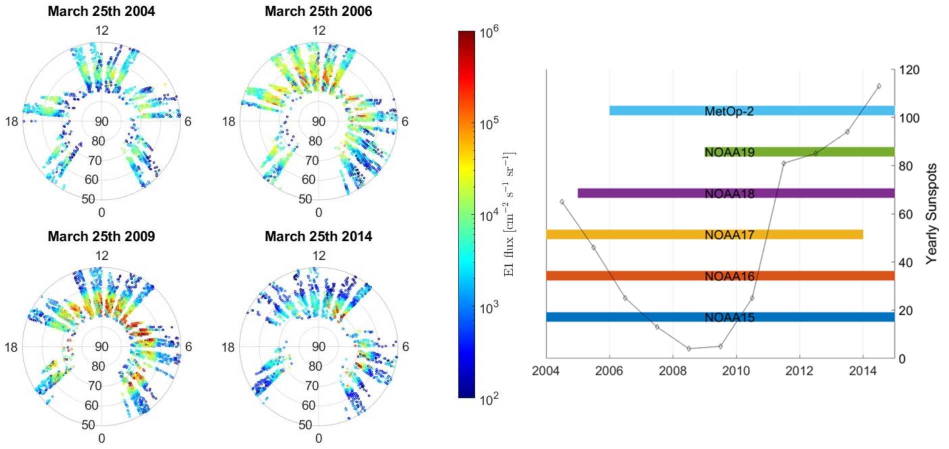

Figure 4.1: On the left, the daily satellite MLT and CGM latitude coverage for the NOAA/POES and EUMETSAT/MetOp satellites with daily BLC flux measurements of $>$ 43 keV electrons on the 25th of March 2004, 2006, 2009, and 2014. To the right is the satellites' operation time from 2004 – 2014, with the yearly sunspot number shown by the gray line. The Figure is modified from *Babu et al.* (2022).

with energies above roughly 1000 keV (*Yando et al.*, 2011; *Nesse Tyssøy et al.*, 2016).

When in operation, the true electron energy limits depend on the incoming energy spectrum (*Yando et al.*, 2011). *Ødegaard et al.* (2017) determined a new optimized effective integral energy limit and associated geometric factors for MEPED's electron measurements and the electron contamination observed in the P6 channel. This recalibration was based on a series of realistic power-law and exponential spectra, calculated based on the geometric factors detailed in *Yando et al.* (2011). The nominal alongside the newly optimized lower energy limits are presented in Table 4.1.

The electron telescopes are susceptible to proton contamination (*Evans and Greer*, 2004; *Yando et al.*, 2011). Without proper adjustments, this can significantly overestimate the actual electron fluxes (*Nesse Tyssøy et al.*, 2016). *Evans and Greer* (2004) suggests that,

Table 4.1: The nominal and new optimized integral lower energy limits for electrons in the three electron channels (E1, E2, E3) and the highest proton channel (P6) of the SEM-2 MEPED detectors.

Energy Channel	**Nominal Lower Limit [keV]**	**New Optimized Lower Limit [keV]**
E1	> 30	> 43
E2	> 100	> 114
E3	> 300	> 292
P6	-	> 756

in theory, proton contributions to the electron telescope sensor readings can be deduced from the proton detector telescope data; however, radiation damage to the proton detection system introduces uncertainty in these corrections. *Sandanger et al.* (2015) and *Ødegaard et al.* (2016) account for the degradation by determining a complete set of correction factors for the SEM-2 package. The corrected proton integral flux spectra in the energy range known to contaminate the different electron detectors (*Evans and Greer*, 2004) are then retrieved and subtracted from the original electron flux measurements. Further details on the procedures can be found in *Nesse Tyssøy et al.* (2016).

To determine the precipitating MEE fluxes, the orientation of the telescopes needs to be assessed. One proton and one electron detector are mounted such that they point radially outward from the Earth-satellite connecting axis, called the 0° detectors. In SEM-2, the remaining two detectors are mounted perpendicular to the 0° detectors and anti-parallel to the satellite traveling direction and are called the 90° detectors (*Evans and Greer*, 2004). All telescopes are rotated away from the described axis by 9° to ensure a clear field of view. The viewing angle of the telescopes is 30° full-width.

At middle to high latitudes, the 0° detector will measure within the BLC, while the 90° detector captures both precipitating and/or trapped fluxes (*Rodger et al.*, 2010). In rare cases of strong pitch angle diffusion due to large geomagnetic disturbances, the MEE fluxes can have an isotropic distribution, allowing the 0° and 90° detector to give a realistic estimate of the precipitating flux (*Nesse Tyssøy et al.*, 2016). Predominantly, the medium energy electrons are strongly anisotropic and have decreasing fluxes towards the center of the BLC. This results in an underestimation of the precipitating fluxes by the 0° detector and an overestimation by the 90° detector. As such, the telescopes will not be able to provide a realistic estimate of the precipitating fluxes if used separately.

Nesse Tyssøy et al. (2016) develop a comprehensive method to address the limitations of using independent telescope measurements for accurate precipitating flux estimates. They estimate the electron pitch angle anisotropy and diffusion level by integrating the measurements from both the 0° and 90° MEPED telescopes with theoretically determined pitch angle distributions. This approach involves solving the Fokker-Planck equation for wave-particle interactions for electron diffusion (*Kennel and Petschek*, 1966; *Theodoridis and Paolini*, 1967) over a wide range of diffusion coefficients and then transforming them to the altitude of the satellite. Furthermore, to identify the theoretical pitch angle distribution that best corresponds to observations, the flux measurement ratios from the two telescopes are used while adjusting for viewing directions, magnetic field orientation, and detector response across different angles. Finally, the BLC size is calculated using the International Geomagnetic Reference Field model, and a realistic representation of

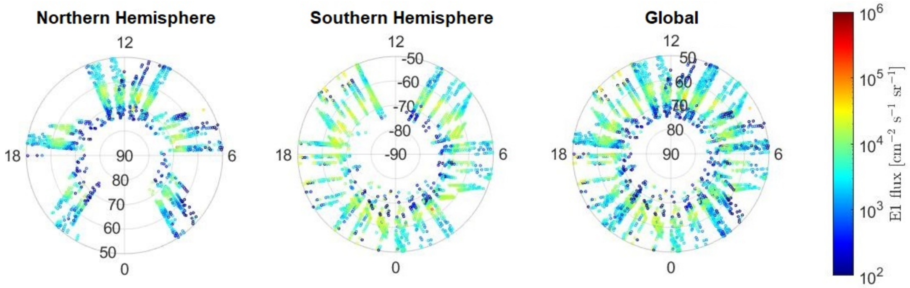

Figure 4.2: The POES coverage over a full day on March 25th, 2004. Three satellites were in operation: NOAA 15, 16, and 17. The Northern and Southern Hemisphere coverage is shown to the left and in the middle, respectively. To the right is the coverage of the satellites when combining the Northern and Southern Hemisphere data. The color bar indicates the daily $>$ 43 keV BLC flux measurements for each point. Published in Paper II.

the precipitating electron flux corresponding to the pitch angle range of the BLC is estimated. Further details on the methodology for constructing the BLC flux estimates are provided in *Nesse Tyssøy et al.* (2016). The left of Figure 4.1 shows the estimated $>$ 43 keV BLC electron fluxes measured over the NH for four different days over the eleven years.

Utilizing the Estimated BLC fluxes

With the constructed BLC flux estimates by *Nesse Tyssøy et al.* (2016), a new opportunity to gain a deeper understanding of the complex dynamics of the high energies of EEP and their effects on the atmosphere opens up. The papers comprising this thesis use the BLC fluxes with the optimized effective integral limits over 11 years from 2004 to 2014 with a daily resolution. While other studies try to scale indices to the flux responses (e.g., *van de Kamp et al.*, 2016; *Tyssøy et al.*, 2021), the papers in this thesis investigate the possibility of a stochastic model. The daily fluxes in Paper I are averaged over 55° – 75° CGM latitude and all MLT in the NH. In papers II and III, a daily global flux for all four energy channels is estimated by combining measurements from both the NH and SH.

Figure 4.2 shows the measured $>$ 43 keV flux coverage for all operational satellites in the Northern and Southern Hemispheres on March 25th, 2004. As previously mentioned, data scarcity is observed around 0 MLT in the NH. In the SH, the data gap is around midday or 12 MLT. Combining the measurements achieves a global daily flux with more comprehensive data points and better MLT coverage (see the example to the right in Figure 4.2). However, different MLT sectors will have different coverage depending on the number of satellite passings. Hence, the global daily BLC flux is first segmented into four MLT sectors: 0-6, 6-12, 12-18, and 18-24 MLT, and then averaged over the four sectors and the CGM latitude bands of 55° – 70° N/S Hemisphere. The change in the latitude band from Paper I to Papers II and III is based on the findings in *Babu et al.* (2022). Though determining the equatorward boundary of MEE precipitation, *Babu et al.* (2022) demonstrates that 55° – 70° CGM latitude captures the main region of MEE precipitation.

4.2 SOFIE on the AIM Satellite

Launched as part of NASA's Aeronomy of Ice in the Mesosphere (AIM) mission, the Solar Occultation For Ice Experiment (SOFIE) has been measuring temperature, ice water content, and a range of trace gases such as H_2O, CO_2, O_3, CH_4, and NO in the polar middle atmosphere from May 2007 until March 2023. NO is one of the atmospheric gases created by EEP and is a key indicator for studying EEP's impact on the atmosphere.

SOFIE has a polar, Sun-synchronous orbit, completing a revolution every 96 minutes, allowing it to orbit the Earth 15 times a day. The satellite takes NO measurements twice per orbit, one in the NH and one in the SH, during local sunset and sunrise. The latitudinal coverage varies from 65° – 85° depending on the time of day and time of year. The NO profiles, which span from 30 to 150 km altitude, offer a vertical resolution of 1 km and are sampled every 0.2 km, effectively covering the range from the upper stratosphere to the lower thermosphere.

Paper II uses the complete SOFIE NO data (version 1.2) over the SH from 2007 to 2014. The decision to limit the NO profile analysis to the SH stems from the significant amount of non-retrievable data below 80 km in the NH due to large thermal oscillations in the detector (see *Gómez-Ramírez et al.* (2013) for further details on retrieval methods and corrections for the SOFIE NO measurements). Additionally, the analysis of NO profiles in the NH is complicated by the higher frequency of SSWs, attributed to the region's highly varying topography, as discussed in Section 3.1.

Initially, the NO data was used to try and identify conditions of EEP's direct effect down to 50 km, specifically by observing significant NO density increases at these altitudes. To do so, establishing a baseline atmosphere was essential. An eight-year median of the NO data and different smoothing and scaling methods were tested. Figure 4.3 presents events identified using a 30-day smoothed NO baseline. An event was classified as a 90 km event (black circles) if the NO density increased by more than 100% above the baseline at altitudes of 110, 100, and 90 km within the same day. If these events also showed a NO increase of over 25% at altitudes of 80, 70, 60, or 50 km on the same or the following day, they were further classified: those reaching down to 50 km are highlighted

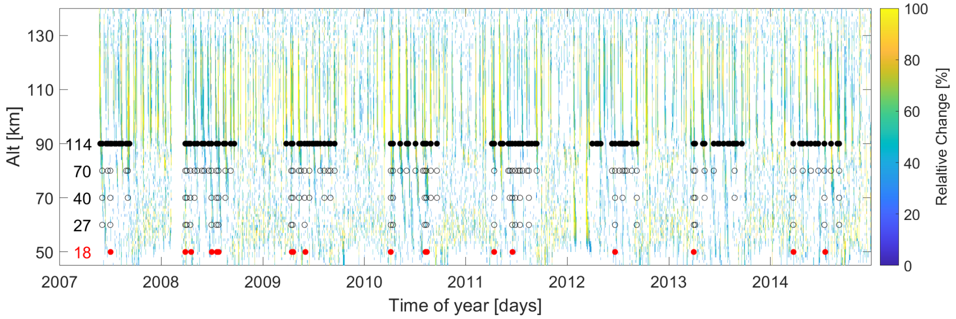

Figure 4.3: The relative NO increase above a 30-day smoothed NO background. 90 km events are shown with solid black circles and 50 km with solid red circles. The hollow circles show events from 80 – 60 km. For clarity, the relative change in the NO data below 20% is not shown.

with red circles, while the others are indicated by empty circles. To ensure clarity in event identification, those occurring within a four-day window were considered a single event, occurrences with incomplete data three days before or after were excluded, and any events coinciding with solar proton events were disregarded. The number of events at each altitude is shown to the left in the figure.

Figure 4.4 shows a Superposed Epoch Analysis (SEA) of the events reaching 90 and 80 km (left) and the ones reaching all the way down to 50 km (right). Onset (day 0) is defined as the day the NO density peaks at 90 km. The NO profiles show that the 50 km events have a clear, direct increase in NO all the way down to 50 km on the onset day, something not evident for 90 km events. This finding was consistent for all tested NO backgrounds.

In analyzing the responses of BLC electron flux, geomagnetic indices, and solar wind properties across the two event categories, challenges emerged due to inconsistencies in how the NO data from SOFIE scaled with flux responses. NO concentrations in the atmosphere, which are very dynamic and fluctuate with seasonal changes in sunlight conditions at the poles, complicate the event selection. Furthermore, SOFIE's method of conducting a single measurement per orbit at varying latitudes based on local sunrise and sunset adds variability. Measurements may or may not occur within regions of MEE precipitation, affecting the data's representation of electron precipitation's impact on NO. Additionally, the limited number of 50 km events fulfilling the criteria made the assessment challenging and inconclusive.

Instead, Paper II explores the geomagnetic conditions and solar wind properties associated with large $>$ 292 keV electron flux responses. This method allows for a more statistically sound response and confirms the presence of fluxes necessary for observing

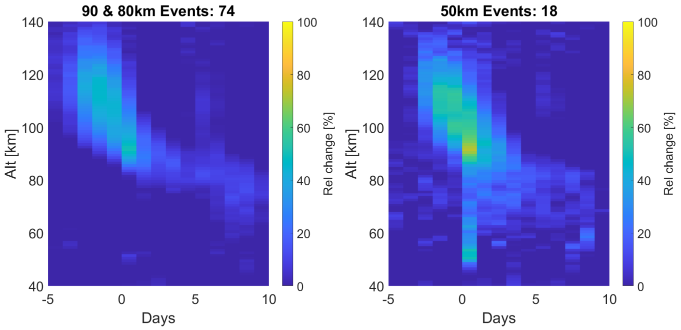

Figure 4.4: SEA of the relative change in NO density for the events reaching 90 and 80 km altitude (left) and those reaching 50 km (right). The y-axis shows altitude from 40 – 140 km. The x-axis shows days from onset (0), defined as the day the NO density peaks at 90 km.

the direct impact of EEP at lower altitudes. The NO profiles from the SH are then used as supplementary data to show atmospheric effects corresponding to these flux responses.

4.3 Solar Wind and Geomagnetic Data

The solar wind and geomagnetic data used in this thesis are all on a daily resolution. To get an idea of the solar wind forcing, the IMF B_z [nT] in geocentric solar magnetic coordinates and the solar wind bulk speed v [km/s] were retrieved from the OMNI2 (formally OMNI) database. To describe the energy transfer from the solar wind to the magnetosphere, the Epsilon parameter (ϵ) [GW] from the SuperMAG database (*Gjerloev*, 2012) is used. This parameter draws from the work of *Akasofu* (1981) and uses the solar wind speed, IMF strength, and the orientation of the IMF at several R_E to give an estimate of the efficiency of the magnetic reconnection process at the magnetopause. The daily substorm onset rate derived based on the auroral electrojet SML index is also retrieved from the SuperMAG database (*Newell and Gjerloev*, 2011). Lastly, the categorization of solar wind structures (being either CME- or HSS-driven) based on *Richardson and Cane* (2012) was used to give further context to the solar wind forcing.

To describe geomagnetic activity, the AE [nT], Kp, and Dst [nT] indices were chosen. These indices are calculated using standardized methods agreed upon by the International Association of Geomagnetism and Aeronomy, making them consistent and comparable over time and across different research studies. The AE (Auroral Electrojet) index quantifies the strength of the geomagnetic activity in the NH auroral zone, reflecting disturbances in the Earth's magnetic field due to auroral electrojet currents. The Kp index is a global geomagnetic activity indicator based on measurements from mid-latitudes. It measures fluctuations in the Earth's magnetic field on a scale from 0 to 9, with higher values indicating more intense geomagnetic storms. The Ap index, used in the model by *van de Kamp et al.* (2018), is derived from the Kp index by transforming the quasi-logarithmic Kp values into a linear scale. As previously mentioned, the Dst index is the Disturbance Storm Time index, which tracks worldwide geomagnetic storm intensity by measuring the strength of the equatorial ring current at low latitudes. The geomagnetic indices are also retrieved from the OMNI2 database.

5 Summary of Papers

This section introduces the three papers forming this thesis. The papers offer insights into the variations within the MEE precipitation spectrum with a focus on the characteristics of the high-energy tail. Further, they investigate which solar wind properties drive large flux enhancements of high-energy tail electrons and examine their associated geomagnetic responses. The objective is to increase our understanding of the high-energy tail's unique behavior and drivers. The overarching goal is to pave the way for an MEE parameterization that better captures the entire energy spectrum to be applied in future chemistry-climate models.

Further, they investigate what solar wind properties drive large flux enhancements of high-energy tail electrons and what characteristic geomagnetic responses they are associated with.

Paper I: Exploring the Predictability of the High-Energy Tail of MEE Precipitation Based on Solar Wind Properties

Paper I investigates how the high-energy tail of MEE precipitation with energies $\gtrsim 300$ keV differs from the lower energies of $\gtrsim 30$ keV. The study focuses on three key aspects:

- Maximum flux response.
- Timing of the maximum flux response.
- Duration of the flux response.

The differences are explored in the context of solar wind structures and the solar wind properties B_z, v, and ϵ. The motivation comes from the considerable differences in existing parameterizations and observations regarding these aspects (*Tyssøy et al.*, 2019; *Nesse Tyssøy et al.*, 2022). The aim is to establish a probabilistic MEE parameterization that goes beyond the average picture, capturing the full variability of the EEP energy spectrum.

All the available optimized BLC fluxes in the NH from 2004 to 2014 for the > 43 and > 292 keV energy channels are used. CMEs and HSSs were categorized into single and combined events. An event was selected if it lasted at least one day and had slower, interstream, solar wind the days before and after. Events with gaps in the flux data or with fluxes falling below 250 electrons $cm^{-2}s^{-1}sr^{-1}$ were discarded. Lastly, if the > 43

or $>$ 292 keV flux peaked before the arrival of the solar wind structure, the event was removed. Based on these criteria, 249 events were identified: 38 CMEs, 181 HSSs, and 34 events being a combination of both.

The event selection enables an analysis of how solar wind structures influence differences between the two energy channels. As the $>$ 43 keV flux evolution is fairly well correlated with geomagnetic activity (*van de Kamp et al.*, 2016; *Tyssøy et al.*, 2021), this study targets the behavior of the $>$ 292 keV flux relative to the lower energies. Onset is defined as the peak in the $>$ 43 keV flux. All solar wind parameters are averaged from two days before to one day after the onset, as this captured the main energy transfer period.

Comprising 73% of the cases, HSS-driven events show the lowest flux responses, suggesting an average-based parameterization will best represent them but downplay times with stronger precipitation. A correlation of 0.89 exists between the $>$ 43 and $>$ 292 keV flux peaks. However, the $>$ 292 keV peak can vary by an order of magnitude for a certain $>$ 43 keV response. Accounting for solar wind structure improves correlation. ϵ consistently relates to the $>$ 292 keV peak for both CME and HSS events, proving valuable if the solar wind structure is unknown. The correlations are only useful if the delay between the flux peaks is known.

The delay of the $>$ 292 keV peak, relative to the $>$ 43 keV peak, ranges from zero to three days, with a one-day delay occurring most frequently. Higher probabilities for faster or slower delays depend on the solar wind structure, where CMEs are more likely to have a zero-day than a two-day delay, while the opposite is true for HSSs. The four-day average solar wind speed can be applied to increase the capability of predicting a certain delay, though different thresholds are required for the different structures. For example, v $>$ 400 km/s makes a zero-day delay more probable during CMEs, while for HSSs, this threshold is at v $>$ 550 km/s.

While the $>$ 292 keV flux duration typically spans four days regardless of solar wind structure, the $>$ 43 keV flux duration varies and is, on average, one day for CME-driven and two days for HSS-driven events. In other words, even short $>$ 43 keV responses can lead to long-lasting $>$ 292 keV fluxes. None of the applied solar wind parameters correlated with duration.

The established characteristics of the high-energy tail of MEE precipitation in Paper I shed light on why a geomagnetic index that correlates well with the lower energies will not accurately represent the high-energy tail. A certain value of the $>$ 43 keV flux peak can result in a $>$ 292 keV flux peak that varies by one order of magnitude. The occurrence of the respective peak is likely to be delayed. Furthermore, a parameterization based on the average events will underestimate the strongest precipitation events largely associated with CMEs. Not taking into account the differences in timing and duration will further lead to an underestimation of MEE precipitation after the peak in the $>$ 43 keV flux. The probability of a certain $>$ 292 keV response is dependent on the solar wind structure. However, the low number of CME-related events makes it hard to draw strong conclusions, though clear tendencies are present. Throughout the study, B_z showed the weakest correlation with high-energy tail properties, likely due to its oscillation between negative and positive values where a daily resolution averages these fluctuations to around zero.

Paper II: The High-Energy Tail of Energetic Electron Precipitation: Solar Wind Drivers and Geomagnetic Responses

Paper II investigates the solar wind properties and geomagnetic responses linked to substantial high-energy tail MEE fluxes. The motivation is to address the observed underestimation of MEE flux parameterizations, particularly during periods of strong solar and geomagnetic activity (*Tyssøy et al.*, 2019). The study seeks to identify predictive indicators for the high-energy tail of MEE, contributing to a more accurate parameterization of the full EEP spectrum in future atmospheric models. The optimized BLC electron fluxes from the NH and SH are used to obtain a global daily average flux covering an entire solar cycle (2004-2014). To assess atmospheric impacts, the study also incorporates NO density measurements from the SOFIE instrument aboard the AIM satellite.

164 peaks in the $>$ 43 keV electron flux exceeding the 90th percentile are identified and categorized based on the corresponding $>$ 292 keV peak fluxes.

- The third with the weakest and strongest $>$ 292 keV flux peaks termed absolute E1 and E3 events, respectively.
- The third with the lowest and highest $>$ 292 keV peaks scaled by the $>$ 43 keV peak termed relative E1 and E3 events, respectively.
- A subset of absolute events, termed overlapping E1 and E3 events, identified based on comparable $>$ 43 keV fluxes.

This categorization led to a total of 110 absolute, 110 relative, and 25 overlapping events. Analyzing the absolute events allows us to identify how strong solar wind and geomagnetic responses need to be to give high $>$ 292 keV fluxes. The relative and overlapping events provide insight into the conditions leading to large high-energy tail fluxes, independent of the initial $>$ 43 keV and total energy flux.

Superposed epoch analysis of NO revealed that absolute E3 events will directly impact the lower mesosphere. While no single solar wind or geomagnetic parameter could fully account for the observed variations in electron precipitation across the E1 and E3 event categories, certain tendencies emerged. Notably, the high-energy tail tends to be associated with elevated solar wind speeds persisting in the recovery of a deep Dst trough.

Probability assessments revealed ϵ, Dst, and Kp as the best single predictors of absolute E1 and E3 events, each exhibiting specific activity thresholds that increase the likelihood of specific events. Additionally, thresholds that either guarantee or rule out an E1 or E3 event with over 95% certainty were identified. Kp is found to be the best parameter as it accurately identified 55% of events. However, when considering solar wind structures, the Dst index could identify 65% of the absolute E1 and E3 events, making it the most indicative parameter for the high-energy tail response. In accordance with Paper I, most E1 events were associated with HSSs, while the E3 events had a more even distribution between CMEs and HSSs.

The study provides insight into how a stochastic model of MEE precipitation can use certain thresholds to identify the probability of high $>$ 292 keV flux responses. Dst and Kp were found to be the best predictive parameters. When it comes to determining the events in the ambiguous range, the results point to high solar wind speeds in the declining phase of a deep Dst trough. However, case studies are necessary to evaluate this hypothesis.

Paper III: The High-Energy Tail of Energetic Electron Precipitation: Case Studies

Paper III evaluates the absolute E1 and E3 events (now just E1 and E3 events) from Paper II through specific case studies. The overarching goal of the detailed examination of case studies is to reveal potential mechanisms that prevent or facilitate acceleration and precipitation of the high-energy tail of MEE. Paper III sets out to evaluate the hypothesis about how elevated solar wind speed persisting in the recovery phase of a deep Dst trough can drive high $>$ 292 keV fluxes. The hypothesis is tested by examining events associated with Kp and Dst extremes with regard to solar wind properties and geomagnetic responses. The case study events are as follows:

- The E1 event with the strongest Dst deflection.
- The E3 event with the weakest Dst deflection.
- The E1 event with the strongest Kp maximum.
- The E3 event with the weakest Kp maximum.

These events mark the limits of the ambiguous Dst and/or Kp ranges found in Paper II. The case studies reveal that high solar wind speed in the recovery phase of a deep Dst trough is not sufficient to guarantee E3 events. Instead, moderate but persistent geomagnetic activity and preloading of the radiation belts seem to stand out for the ambiguous events. More importantly, the analysis reveals that strong Dst values can be associated with weak Kp values and vice versa. This led to an examination of the simultaneous application of Kp and Dst limits to improve event predictability. Interestingly, the E3 event with the weakest Dst deflection was found to be the only E3 event with consistent positive daily B_z values, making it a significant outlier. Its evolution into an E3 event is likely due to persistent, long-lasting, elevated Kp and substorm rate values that ensure acceleration and scattering of the electrons combined with an elevated radiation belt population prior to the event. Consequently, this outlier was excluded when applying the concurrent Kp and Dst criteria for event analysis.

Using both Kp and Dst criteria successfully classifies 75% of the events. This accuracy increased further to 85% when accounting for variations in solar wind structures. The 15% of events left in the ambiguous range were evaluated separately. Though far from a homogeneous group, certain tendencies did reveal themselves. The turning of the IMF B_z component from negative to positive on epoch day zero or one can be used to identify an ambiguous event as an E1 event, allowing for accurate categorization of all but two E1 events but wrongly classifying one ambiguous E3 event. The northward turning of B_z effectively slows the energy transfer from the solar wind to the magnetosphere and reduces the substorm activity. It also makes remaining substorm activity less efficient as the plasmapause will expand and reduce the area of chorus wave growth.

Generally, it was found easier to exclude than to determine an E3 event. For the ambiguous E3 events, the key seems to be in prolonged and sustained substorm activity and/or high solar wind speed driving ULF waves. Events with such properties seem to be able to evolve into E3 events despite low or moderate Kp and Dst values.

The results of Paper III, together with Paper II, imply that concurrent criteria, for example, using Kp, Dst, and even maybe B_z, and/or a more stochastic approach, are needed to better capture the nature of the high-energy tail electron precipitation.

Some Challenges Related to the Analyses

The event selection across a solar cycle presents challenges in assessing the categorizations of events in a statistically robust manner due to their low numbers. This is especially true when further categorizing the events by solar wind properties and > 292 keV response.

The choice of applying daily scales is motivated by the temporal resolution used in chemistry-climate models. However, this might result in the loss of more detailed information about the intensity of various parameters. Such an approach may hide critical insights necessary for understanding the mechanisms behind high-energy tail electron precipitation.

Although the studies in this thesis mark a significant stride towards identifying the occurrence of strong, high-energy tail flux events, pinpointing the exact intensity of these events remains outside our scope. Furthermore, the applied fluxes are estimates, which, despite optimization efforts, have uncertainties. For example, the pitch angle distribution calculations assume steady-state conditions, which might be violated in the main phase of a storm. The research methodology, which averages data across longitudes, MLT, and even hemispheres, further disguises the complexities of these phenomena by smoothing over localized variations that could offer a deeper understanding. The averaging highlights the delicate balance between obtaining a broad overview and preserving essential information that affects high-energy electron precipitation.

6 Conclusions and Future Prospects

Conclusions

The aim to investigate the nature of MEE precipitation is motivated by the need to increase the accuracy of a future parameterization of MEE to be applied in climate models. Moreover, a better understanding of the fundamental nature of acceleration and loss in the outer radiation belt and ring current could provide a better prediction of the harsh radiation environment for the increasing number of satellites orbiting the Earth. These different perspectives are two sides of the same coin, and the results of this thesis feed into the prospects of both.

The objective is to increase our understanding of the high-energy tail's unique behavior and drivers. Two research questions were set to achieve this: "How do the characteristics of the high-energy tail differ from those of lower-energy MEE precipitation?" and "Which solar wind and geomagnetic parameters can capture the variations in the high-energy tail of MEE precipitation?". The nature of the high-energy tail is investigated over 11 years from 2004 to 2014 by using the optimized bounce loss cone fluxes by *Nesse Tyssøy et al.* (2016). Paper I answers the first research question by establishing the differences in peak response, timing, and duration between the > 43 keV and > 292 keV peak fluxes in the context of different solar wind structures and properties. Papers II and III set out to answer the second research question by finding the predictive capabilities of solar wind and geomagnetic parameters to capture strong high-energy tail precipitation events.

From Paper I, it is clear that a parameterization including the delayed and prolonged high-energy tail response could better capture the intensity, range, and duration of MEE precipitation events. The differences between the > 43 and > 292 keV fluxes are also dependent on solar wind drivers. Most evident is the higher fluxes associated with CME-related events. As the occurrence frequency of HSSs is much higher than CMEs, an "average" storm will most likely underestimate the strong precipitation events that occur during CMEs and combined structures. Therefore, knowing the solar wind driver can further help parameterize the > 292 keV fluxes more accurately.

Papers II and III analyze the most intense > 43 keV MEE flux events across the solar cycle to identify which solar wind parameters or geomagnetic indices can accurately reflect changes in the associated > 292 keV flux. However, Paper II showed that no single solar wind nor geomagnetic parameter can capture the differences. Instead, thresholds can be applied to the parameters to help determine the probability of a high or low > 292 keV flux response. Dst and Kp proved most effective, identifying over half of the events. With knowledge of the solar wind structure, Dst's identification abilities increased to 65% of events. Paper III showed that the combination of Dst and Kp could identify up to 75% of the events that were separated into high and low > 292 keV flux peaks. This effectiveness arises from their ability to partially identify different events when applied individually. When knowing the solar wind structure, the combination of Dst and Kp can further identify 85% of the events.

In paper III, the events left within the ambiguous range of Dst and Kp were evaluated as case studies. Though the events had different properties, the turning of the IMF Bz component from negative to positive in the storm's recovery phase helped identify all but two E1 events but wrongly classified one E3 event. Generally, it was found to be easier to exclude the possibility of a strong > 292 keV event than to guarantee one. However, for events with strong > 292 keV fluxes but with moderate Kp and Dst signatures, sustained elevated activity over multiple days seems to be characteristic.

Despite challenges in analysis and interpretation, Papers I through III contribute to expanding our understanding of the high-energy tail of MEE. They offer valuable insights that could aid in the development of parameterizations based on concurrent criteria and in establishing a stochastic parameterization approach.

Future Prospects: A Stochastic Parameterization of MEE to be Applied in Climate Models

Currently, a new solar forcing dataset for the climate model CMIP7 is being constructed (*Funke et al.*, 2024). As a response to the reported underestimation of the MEE ionization rates in CMIP6, updated particle flux observations using both the 0° and 90° telescopes are being used to construct the precipitation model. Moreover, as documented in Paper I, it is recommended to incorporate a lagged or an accumulated response to better capture the delay of the high-energy tail. If validation of the resulting ionization reveals that the scaling parameter corresponds to a wide range of possible flux responses, then *"implementing a stochastic solar-cycle-dependent element should be considered"* (*Funke et al.*, 2024). As such, the results of papers II and III can also have a direct implication for the MEE ionization rates recommended in chemistry-climate model runs. On the other hand, the new CMIP7 MEE ionization rate will most likely depend on one single geomagnetic index as in CMIP6. Based on the results of Paper III, using a two-variable approach is likely to better reflect the high-energy tail. Therefore, a natural step forward would be to develop our own MEE parameterization model.

In addition to Papers I-III, I contributed to four other papers, all addressing different perspectives on the nature of MEE. *Babu et al.* (2022, 2023) developed a model for the varying equatorward boundary of the MEE precipitation region. In *Tyssøy et al.* (2021), AE-based proxies are achieved by accumulating the AE activity over multiple days, including an e-folding lifetime. This approach enables the prediction of 72-86% of the detected daily MEE precipitation variance. As pointed out in Paper II, the AE-based proxies capture the general features of our SEA flux analysis, but are not able to identify the individual high-energy tail events. In the future, it would be valuable to combine these findings into a unified approach. The development of an average-based model that scales the MEE flux intensity by an accumulated geomagnetic index and the equatorward precipitation boundary by daily Dst values could serve as a starting point. Next, a stochastic element can be added utilizing the findings of Papers I-III. For example, in terms of the high-energy tail, the full range of flux responses or the standard deviation of the average MEE model can be applied to upscale or downscale the average flux prediction. This would allow the full range of MEE flux responses throughout the solar cycle to be represented. Finally, the characteristics of the slot region events found in *Nesse et al.* (2023) can be implemented to account for the additional MEE drizzle after the geomagnetic activity subsides. In this manner, the collective key findings from all seven papers can form a new MEE parameterization capable of estimating flux intensity, precipitation regions, and a realistic energy spectrum on daily to decadal scales.

List of Abbreviations

AIM	Aeronomy of Ice in the Mesosphere
BLC	Bounce Loss Cone
CGM	Corrected Geomagnetic
CIR	Co-rotating Interaction Region
CME	Coronal Mass Ejection
DLC	Drift Loss Cone
Dst	Disturbance Storm Time
EEP	Energetic Electron Precipitation
EMIC	Electromagnetic Ion Cyclotron
EPP	Energetic Particle Precipitation
HSS	High-speed Solar wind Streams
IMF	Interplanetary Magnetic Field
MEE	Medium Energy Electron
MEPED	Medium Energy Proton and Electron Detector
MetOp	Meteorological Operational
MLT	Magnetic Local Time
NH	Northern Hemisphere
POES	Polar Operational Environmental Satellites
SAA	South Atlantic Anomaly
SH	Southern Hemisphere

SOFIE	Solar Occultation For Ice Experiment
SPE	Solar Proton Events
SSC	Storm Sudden Commencement
SSW	Sudden Stratospheric Warming
ULF	Ultra-Low Frequency
VLF	Very-Low Frequency

Bibliography

Akasofu, S. I. (1981), Energy coupling between the solar wind and the magnetosphere, *Space Science Reviews*, *28*, doi:10.1007/BF00218810. 41

Andrews, D. G., C. B. Leovy, J. R. Holton, J. Marshall, and R. A. Plumb (1987), *Middle atmosphere dynamics*, Elsevier Science and Technology. 24

Angelopoulos, V., X.-J. Zhang, A. V. Artemyev, D. Mourenas, E. Tsai, C. Wilkins, A. Runov, J. Liu, D. L. Turner, W. Li, K. Khurana, R. E. Wirz, V. A. Sergeev, X. Meng, J. Wu, M. D. Hartinger, T. Raita, Y. Shen, X. An, X. Shi, M. F. Bashir, X. Shen, L. Gan, M. Qin, L. Capannolo, Q. Ma, C. L. Russell, E. V. Masongsong, R. Caron, I. He, L. Iglesias, S. Jha, J. King, S. Kumar, K. Le, J. Mao, A. McDermott, K. Nguyen, A. Norris, A. Palla, A. Roosnovo, J. Tam, E. Xie, R. C. Yap, S. Ye, C. Young, L. A. Adair, C. Shaffer, M. Chung, P. Cruce, M. Lawson, D. Leneman, M. Allen, M. Anderson, M. Arreola-Zamora, J. Artinger, J. Asher, D. Branchevsky, M. Cliffe, K. Colton, C. Costello, D. Depe, B. W. Domae, S. Eldin, L. Fitzgibbon, A. Flemming, D. M. Frederick, A. Gilbert, B. Hesford, R. Krieger, K. Lian, E. McKinney, J. P. Miller, C. Pedersen, Z. Qu, R. Rozario, M. Rubly, R. Seaton, A. Subramanian, S. R. Sundin, A. Tan, D. Thomlinson, W. Turner, G. Wing, C. Wong, and A. Zarifian (2023), Energetic electron precipitation driven by electromagnetic ion cyclotron waves from elfin's low altitude perspective, *Space Science Reviews*, *219*(5), 37, doi:10.1007/s11214-023-00984-w. 30

Asikainen, T., and M. Ruopsa (2016), Solar wind drivers of energetic electron precipitation, *Journal of Geophysical Research: Space Physics*, *121*(3), 2209–2225, doi: 10.1002/2015JA022215. 7, 8, 20

Asikainen, T., A. Salminen, V. Maliniemi, and K. Mursula (2020), Influence of enhanced planetary wave activity on the polar vortex enhancement related to energetic electron precipitation, *Journal of Geophysical Research: Atmospheres*, *125*(9), e2019JD032,137, doi:https://doi.org/10.1029/2019JD032137. 26, 29

Babu, E. M., H. N. Tyssøy, C. Smith-Johnsen, V. Maliniemi, J. A. Salice, R. M. Millan, and I. G. Richardson (2022), Determining latitudinal extent of energetic electron precipitation using meped on-board noaa/poes, *Journal of Geophysical Research: Space Physics*, *127*(9), e2022JA030,489, doi:10.1029/2022JA030489. 29, 31, 36, 39, 51

Babu, E. M., H. Nesse, S. M. Hatch, N. Olsen, J. A. Salice, and I. G. Richardson (2023), An updated geomagnetic index-based model for determining the latitudinal extent of energetic electron precipitation, *Journal of Geophysical Research: Space Physics*, *128*(10), e2023JA031,371, doi:https://doi.org/10.1029/2023JA031371. 31, 51

Baker, D. N., G. M. Mason, and J. E. Mazur (2012), A small spacecraft mission with large accomplishments, *Eos, Transactions American Geophysical Union*, *93*(34), 325–326, doi:https://doi.org/10.1029/2012EO340001. 27

Baldwin, M. P., and T. J. Dunkerton (2001), Stratospheric Harbingers of Anomalous Weather Regimes, *Science*, *294*(5542), 581–584, doi:10.1126/science.1063315. 24, 26

Baldwin, M. P., B. Ayarzagüena, T. Birner, N. Butchart, A. H. Butler, A. J. Charlton-Perez, D. I. V. Domeisen, C. I. Garfinkel, H. Garny, E. P. Gerber, M. I. Hegglin, U. Langematz, and N. M. Pedatella (2021), Sudden stratospheric warmings, *Reviews of Geophysics*, *59*(1), e2020RG000,708, doi:https://doi.org/10.1029/2020RG000708. 24

Baumgaertner, A. J. G., A. Seppälä, P. Jöckel, and M. A. Clilverd (2011), Geomagnetic activity related no$_x$ enhancements and polar surface air temperature variability in a chemistry climate model: modulation of the nam index, *Atmospheric Chemistry and Physics*, *11*(9), 4521–4531, doi:10.5194/acp-11-4521-2011. 26

Baumjohann, W., and R. A. Treumann (1996), *Basic Space Plasma Physics*, 340 pp., World Scientific, Garching, doi:10.1142/p015, max-Planck-Institut für Extraterrestrische Physik, Garching and Ludwig-Maximilians-Universität, München. 14

Beharrell, M. J., F. Honary, C. J. Rodger, and M. A. Clilverd (2015), Substorm-induced energetic electron precipitation: Morphology and prediction, *Journal of Geophysical Research: Space Physics*, *120*(4), 2993–3008, doi:10.1002/2014JA020632. 31

Blake, J. B., D. N. Baker, N. Turner, K. W. Ogilvie, and R. P. Lepping (1997), Correlation of changes in the outer-zone relativistic-electron population with upstream solar wind and magnetic field measurements, *Geophysical Research Letters*, *24*(8), 927–929, doi:https://doi.org/10.1029/97GL00859. 20

Borovsky, J. E., and M. H. Denton (2006), Differences between cme-driven storms and cir-driven storms, *Journal of Geophysical Research: Space Physics*, *111*(A7), doi:10.1029/2005JA011447. 27

Bortnik, J., R. M. Thorne, and U. S. Inan (2008), Nonlinear interaction of energetic electrons with large amplitude chorus, *Geophysical Research Letters*, *35*(21), doi:https://doi.org/10.1029/2008GL035500. 18

Brasseur, G. P., and S. Solomon (2005), *Aeronomy of the Middle Atmosphere: Chemistry and Physics of the Stratosphere and Mesosphere*, Springer. 23, 24, 25

Chen, L., and A. Hasegawa (1974), A theory of long-period magnetic pulsations: 1. steady state excitation of field line resonance, *Journal of Geophysical Research (1896-1977)*, *79*(7), 1024–1032, doi:https://doi.org/10.1029/JA079i007p01024. 15

Clilverd, M. A., A. Seppälä, C. J. Rodger, M. G. Mlynczak, and J. U. Kozyra (2009), Additional stratospheric nox production by relativistic electron precipitation during the 2004 spring nox descent event, *Journal of Geophysical Research: Space Physics*, *114*(A4), doi:https://doi.org/10.1029/2008JA013472. 29

Crutzen, P. J., I. S. A. Isaksen, and G. C. Reid (1975), Solar proton events: Stratospheric sources of nitric oxide, *Science*, *189*(4201), 457–459, doi:10.1126/science.189.4201.457. 26

Daae, M., P. Espy, H. Nesse Tyssøy, D. Newnham, J. Stadsnes, and F. Søraas (2012), The effect of energetic electron precipitation on middle mesospheric night-time ozone during and after a moderate geomagnetic storm, *Geophysical Research Letters*, *39*(21), doi:https://doi.org/10.1029/2012GL053787. 29

Damiani, A., B. Funke, M. López Puertas, M. L. Santee, R. R. Cordero, and S. Watanabe (2016), Energetic particle precipitation: A major driver of the ozone budget in the Antarctic upper stratosphere, *Geophysical Research Letters*, *43*(7), 3554–3562, doi:10.1002/2016GL068279. 28

Duderstadt, K. A., C.-L. Huang, H. E. Spence, S. Smith, J. B. Blake, A. B. Crew, A. T. Johnson, D. M. Klumpar, D. R. Marsh, J. G. Sample, M. Shumko, and F. M. Vitt (2021), Estimating the impacts of radiation belt electrons on atmospheric chemistry using firebird ii and van allen probes observations, *Journal of Geophysical Research: Atmospheres*, *126*(7), e2020JD033,098, doi:10.1029/2020JD033098. 31

Dungey, J. W. (1961), Interplanetary magnetic field and the auroral zones, *Phys. Rev. Lett.*, *6*, 47–48, doi:10.1103/PhysRevLett.6.47. 9

Edvartsen, Jone Øvretvedt (2023), Investigating the impact of space weather on the polar atmosphere using rigorous statistical methods, Ph.D. thesis, Doctoral dissertation University of Bergen. 22

European Space Agency (2007), Basic motion of trapped particles in the earth's magnetic field, `https://www.esa.int/ESA_Multimedia/Images/2007/03/Basic_motion_of_trapped_particles_in_the_earth_magnetic_field`, accessed: 2024-02-14. 13

Evans, D., and M. Greer (2004), Polar orbiting environmental satellite space environment monitor - 2 instrument descriptions and archive data documentation, *NOAA Tech. Memo. 1.4*. 35, 36, 37

Fairfield, D. H. (1971), Average and unusual locations of the earth's magnetopause and bow shock, *Journal of Geophysical Research (1896-1977)*, *76*(28), 6700–6716, doi: https://doi.org/10.1029/JA076i028p06700. 8

Freeman, M. P., and S. K. Morley (2004), A minimal substorm model that explains the observed statistical distribution of times between substorms, *Geophysical Research Letters*, *31*(12), doi:https://doi.org/10.1029/2004GL019989. 19

Funke, B., A. Baumgaertner, M. Calisto, T. Egorova, C. H. Jackman, J. Kieser, A. Krivolutsky, M. López-Puertas, D. R. Marsh, T. Reddmann, E. Rozanov, S.-M. Salmi, M. Sinnhuber, G. P. Stiller, P. T. Verronen, S. Versick, T. von Clarmann, T. Y. Vyushkova, N. Wieters, and J. M. Wissing (2011), Composition changes after the "halloween" solar proton event: the high energy particle precipitation in the atmosphere (heppa) model versus mipas data intercomparison study, *Atmospheric Chemistry and Physics*, *11*(17), 9089–9139, doi:10.5194/acp-11-9089-2011. 27

Funke, B., T. Dudok de Wit, I. Ermolli, M. Haberreiter, D. Kinnison, D. Marsh, H. Nesse, A. Seppälä, M. Sinnhuber, and I. Usoskin (2024), Towards the definition of a solar forcing dataset for cmip7, *Geoscientific Model Development*, *17*(3), 1217–1227, doi: 10.5194/gmd-17-1217-2024. 21, 50

Garcia, R. R., and S. Solomon (1985), The effect of breaking gravity waves on the dynamics and chemical composition of the mesosphere and lower thermosphere, *Journal of Geophysical Research: Atmospheres*, *90*(D2), 3850–3868, doi:https://doi.org/10.1029/JD090iD02p03850. 24

Gjerloev, J. W. (2012), The supermag data processing technique, *J. Geophys. Res.*, *117*, doi:10.1029/2012JA017683. 41

Gómez-Ramírez, D., J. W. C. McNabb, J. M. Russell, M. E. Hervig, L. E. Deaver, G. Paxton, and P. F. Bernath (2013), Empirical correction of thermal responses in the Solar Occultation for Ice Experiment nitric oxide measurements and initial data validation results, *Appl. Opt.*, *52*(13), 2950–2959, doi:10.1364/AO.52.002950. 39

Gupta, A., T. Birner, A. Dörnbrack, and I. Polichtchouk (2021), Importance of gravity wave forcing for springtime southern polar vortex breakdown as revealed by era5, *Geophysical Research Letters*, *48*(10), e2021GL092,762, doi:https://doi.org/10.1029/2021GL092762. 24

Haaland, S., H. Hasegawa, G. Paschmann, B. Sonnerup, and M. Dunlop (2021), 20 years of cluster observations: The magnetopause, *Journal of Geophysical Research: Space Physics*, *126*(8), e2021JA029,362, doi:https://doi.org/10.1029/2021JA029362. 8

Horne, R. B., R. M. Thorne, Y. Y. Shprits, N. P. Meredith, S. A. Glauert, A. J. Smith, S. G. Kanekal, D. N. Baker, M. J. Engebretson, J. L. Posch, M. Spasojevic, U. S. Inan, J. S. Pickett, and P. M. E. Decreau (2005), Wave acceleration of electrons in the van allen radiation belts, *Nature*, *437*(7056), 227–230, doi:10.1038/nature03939. 16

Jackman, C. H., M. T. DeLand, G. J. Labow, E. L. Fleming, D. K. Weisenstein, M. K. W. Ko, M. Sinnhuber, and J. M. Russell (2005), Neutral atmospheric influences of the solar proton events in October–November 2003, *Journal of Geophysical Research: Space Physics*, *110*(A9), doi:10.1029/2004JA010888. 27

James, M. K., T. K. Yeoman, P. N. Mager, and D. Y. Klimushkin (2016), Multiradar observations of substorm-driven ulf waves, *Journal of Geophysical Research: Space Physics*, *121*(6), 5213–5232, doi:https://doi.org/10.1002/2015JA022102. 15

Jaynes, A. N., A. F. Ali, S. R. Elkington, D. M. Malaspina, D. N. Baker, X. Li, S. G. Kanekal, M. G. Henderson, C. A. Kletzing, and J. R. Wygant (2018), Fast diffusion of ultrarelativistic electrons in the outer radiation belt: 17 march 2015 storm event, *Geophysical Research Letters*, *45*(20), 10,874–10,882, doi:https://doi.org/10.1029/2018GL079786. 16

Jorgensen, A. M., H. E. Spence, W. J. Hughes, and H. J. Singer (2004), A statistical study of the global structure of the ring current, *Journal of Geophysical Research: Space Physics*, *109*(A12), doi:https://doi.org/10.1029/2003JA010090. 11

Juarez Madera, D., R. A. Marshall, S. Elschot, S. Kaeppler, P. Reyes, R. H. Varney, and A. B. Crew (2023), Time-dependent inversion of energetic electron precipitation spectra from ground-based incoherent scatter radar measurements, *Journal of Geophysical Research: Space Physics*, *128*(5), e2022JA031,000, doi:https://doi.org/10.1029/2022JA031000. 30

Kalliokoski, M. M. H., E. K. J. Kilpua, A. Osmane, D. L. Turner, A. N. Jaynes, L. Turc, H. George, and M. Palmroth (2020), Outer radiation belt and inner magnetospheric response to sheath regions of coronal mass ejections: a statistical analysis, *Annales Geophysicae*, *38*(3), 683–701, doi:10.5194/angeo-38-683-2020. 20

Kanekal, S. G., D. N. Baker, J. F. Fennell, A. Jones, Q. Schiller, I. G. Richardson, X. Li, D. L. Turner, S. Califf, S. G. Claudepierre, L. B. Wilson III, A. Jaynes, J. B. Blake, G. D. Reeves, H. E. Spence, C. A. Kletzing, and J. R. Wygant (2016), Prompt acceleration of magnetospheric electrons to ultrarelativistic energies by the 17 march

2015 interplanetary shock, *Journal of Geophysical Research: Space Physics*, *121*(8), 7622–7635, doi:https://doi.org/10.1002/2016JA022596. 19

Kataoka, R., and Y. Miyoshi (2006), Flux enhancement of radiation belt electrons during geomagnetic storms driven by coronal mass ejections and corotating interaction regions, *Space Weather*, *4*(9), doi:https://doi.org/10.1029/2005SW000211. 7

Kennel, C. F., and H. E. Petschek (1966), Limit on stably trapped particle fluxes, *Journal of Geophysical Research (1896-1977)*, *71*(1), 1–28, doi:https://doi.org/10.1029/JZ071i001p00001. 37

Khazanov, G. V., and A. Glocer (2020), How magnetically conjugate atmospheres and the magnetosphere participate in the formation of low-energy electron precipitation in the region of diffuse aurora, *Journal of Geophysical Research: Space Physics*, *125*(8), e2020JA028,057, doi:https://doi.org/10.1029/2020JA028057. 27

Kidston, J., A. A. Scaife, S. C. Hardiman, D. M. Mitchell, N. Butchart, M. P. Baldwin, and L. J. Gray (2015), Stratospheric influence on tropospheric jet streams, storm tracks and surface weather, *Nature Geoscience*, *8*, 433–440, doi:10.1038/ngeo2424. 26

Kilpua, E., H. E. J. Koskinen, and T. I. Pulkkinen (2017), Coronal mass ejections and their sheath regions in interplanetary space, *Living Reviews in Solar Physics*, *14*(1), 5, doi:10.1007/s41116-017-0009-6. 6

Kilpua, E. K. J., H. Hietala, D. L. Turner, H. E. J. Koskinen, T. I. Pulkkinen, J. V. Rodriguez, G. D. Reeves, S. G. Claudepierre, and H. E. Spence (2015), Unraveling the drivers of the storm time radiation belt response, *Geophysical Research Letters*, *42*(9), 3076–3084, doi:https://doi.org/10.1002/2015GL063542. 20

Kilpua, E. K. J., A. Balogh, R. von Steiger, and Y. D. Liu (2017), Geoeffective properties of solar transients and stream interaction regions, *Space Science Reviews*, *212*(3), 1271–1314, doi:10.1007/s11214-017-0411-3. 7

Kim, K.-C., Y. Shprits, D. Subbotin, and B. Ni (2011), Understanding the dynamic evolution of the relativistic electron slot region including radial and pitch angle diffusion, *Journal of Geophysical Research: Space Physics*, *116*(A10), doi:https://doi.org/10.1029/2011JA016684. 10

Kirkwood, S., A. Osepian, E. Belova, J. Urban, K. Pérot, and A. K. Sinha (2015), Ionization and no production in the polar mesosphere during high-speed solar wind streams: model validation and comparison with no enhancements observed by odin-smr, *Annales Geophysicae*, *33*(5), 561–572, doi:10.5194/angeo-33-561-2015. 29

Koskinen, H. E. J., and E. K. J. Kilpua (2022), *Physics of Earth's Radiation Belts: The-*

ory and Observations, Astronomy and Astrophysics Library, 272 pp., Springer Nature, Springer International Publishing, doi:10.1007/978-3-030-82167-8, open Access under CC BY 4.0 License. 13, 14, 15, 16, 17, 18, 19

Langematz, U., M. Kunze, K. Krüger, K. Labitzke, and G. L. Roff (2003), Thermal and dynamical changes of the stratosphere since 1979 and their link to ozone and co2 changes, *Journal of Geophysical Research: Atmospheres*, *108*(D1), ACL 9–1–ACL 9–13, doi:https://doi.org/10.1029/2002JD002069. 25, 26

Li, X., M. Temerin, D. N. Baker, and G. D. Reeves (2011), Behavior of mev electrons at geosynchronous orbit during last two solar cycles, *Journal of Geophysical Research: Space Physics*, *116*(A11), doi:https://doi.org/10.1029/2011JA016934. 20

Liou, K., T. Sotirelis, and I. Richardson (2018), Substorm occurrence and intensity associated with three types of solar wind structure, *Journal of Geophysical Research: Space Physics*, *123*(1), 485–496, doi:https://doi.org/10.1002/2017JA024451. 19

Longden, N., M. H. Denton, and F. Honary (2008), Particle precipitation during icme-driven and cir-driven geomagnetic storms, *Journal of Geophysical Research: Space Physics*, *113*(A6), doi:https://doi.org/10.1029/2007JA012752. 32

Maliniemi, V., T. Asikainen, and K. Mursula (2016), Effect of geomagnetic activity on the northern annular mode: Qbo dependence and the holton-tan relationship, *Journal of Geophysical Research: Atmospheres*, *121*(17), 10,043–10,055, doi:10.1002/2015JD024460. 1, 26

Maliniemi, V., H. Nesse Tyssøy, C. Smith-Johnsen, P. Arsenovic, and D. R. Marsh (2021), Effects of enhanced downwelling of NO$_x$ on Antarctic upper-stratospheric ozone in the 21st century, *Atmospheric Chemistry and Physics*, *21*(14), 11,041–11,052, doi:10.5194/acp-21-11041-2021. 28

Marsh, D. R., S. C. Solomon, and A. E. Reynolds (2004), Empirical model of nitric oxide in the lower thermosphere, *Journal of Geophysical Research: Space Physics*, *109*(A7), doi:10.1029/2003JA010199. 2, 28

Matthes, K., B. Funke, M. E. Andersson, L. Barnard, J. Beer, P. Charbonneau, M. A. Clilverd, T. Dudok de Wit, M. Haberreiter, A. Hendry, C. H. Jackman, M. Kretzschmar, T. Kruschke, M. Kunze, U. Langematz, D. R. Marsh, A. C. Maycock, S. Misios, C. J. Rodger, A. A. Scaife, A. Seppälä, M. Shangguan, M. Sinnhuber, K. Tourpali, I. Usoskin, M. van de Kamp, P. T. Verronen, and S. Versick (2017), Solar forcing for cmip6 (v3.2), *Geoscientific Model Development*, *10*(6), 2247–2302, doi:10.5194/gmd-10-2247-2017. 21, 31

Milan, S. E., S. W. H. Cowley, M. Lester, D. M. Wright, J. A. Slavin, M. Fillingim, C. W. Carlson, and H. J. Singer (2004), Response of the magnetotail to changes in the open flux content of the magnetosphere, *Journal of Geophysical Research: Space Physics*, *109*(A4), doi:https://doi.org/10.1029/2003JA010350. 8

Milan, S. E., T. A. Evans, and B. Hubert (2010), Average auroral configuration parameterized by geomagnetic activity and solar wind conditions, *Annales Geophysicae*, *28*(4), 1003–1012, doi:10.5194/angeo-28-1003-2010. 28

Millan, R., and R. Thorne (2007), Review of radiation belt relativistic electron losses, *Journal of Atmospheric and Solar-Terrestrial Physics*, *69*(3), 362–377, doi:https://doi.org/10.1016/j.jastp.2006.06.019. 18

Millan, R. M., and D. N. Baker (2012), Acceleration of particles to high energies in earth's radiation belts, *Space Science Reviews*, *173*(1), 103–131, doi:10.1007/s11214-012-9941-x. 10, 11, 14

Mironova, I. A., K. L. Aplin, F. Arnold, G. A. Bazilevskaya, R. G. Harrison, A. A. Krivolutsky, K. A. Nicoll, E. V. Rozanov, E. Turunen, and I. G. Usoskin (2015), Energetic particle influence on the earth's atmosphere, *Space Science Reviews*, *194*(1), 1–96, doi:10.1007/s11214-015-0185-4. 26, 27

Mironova, I. A., A. A. Artamonov, G. A. Bazilevskaya, E. V. Rozanov, G. A. Kovaltsov, V. S. Makhmutov, A. L. Mishev, and A. V. Karagodin (2019), Ionization of the polar atmosphere by energetic electron precipitation retrieved from balloon measurements, *Geophysical Research Letters*, *46*(2), 990–996, doi:10.1029/2018GL079421. 30, 31

Moldwin, M. B., L. Downward, H. K. Rassoul, R. Amin, and R. R. Anderson (2002), A new model of the location of the plasmapause: Crres results, *Journal of Geophysical Research: Space Physics*, *107*(A11), SMP 2–1–SMP 2–9, doi:https://doi.org/10.1029/2001JA009211. 9

Nagai, T., I. Shinohara, Y. Saito, A. Ieda, and R. Nakamura (2023), Location and timing of magnetic reconnections in earth's magnetotail: Accomplishments of the 29-year geotail near-earth magnetotail survey, *Journal of Geophysical Research: Space Physics*, *128*(12), e2023JA032,023, doi:https://doi.org/10.1029/2023JA032023. 8

Nasuddin, K. A., M. Abdullah, and N. S. Abdul Hamid (2019), Characterization of the south atlantic anomaly, *Nonlinear Processes in Geophysics*, *26*(1), 25–35, doi:10.5194/npg-26-25-2019. 17

Nesse, H., E. M. Babu, J. A. Salice, and B. Funke (2023), Energetic electron precipitation during slot region filling events, *Journal of Geophysical Research: Space Physics*, *128*(10), e2023JA031,606, doi:10.1029/2023JA031606. 31, 51

Nesse Tyssøy, H., and J. Stadsnes (2015), Cutoff latitude variation during solar proton events: Causes and consequences, *Journal of Geophysical Research: Space Physics*, *120*(1), 553–563, doi:10.1002/2014JA020508. 27

Nesse Tyssøy, H., J. Stadsnes, F. Søraas, and M. Sørbø (2013), Variations in cutoff latitude during the January 2012 solar proton event and implication for the distribution of particle energy deposition, *Geophysical Research Letters*, *40*(16), 4149–4153, doi:10.1002/grl.50815. 27

Nesse Tyssøy, H., M. I. Sandanger, L.-K. G. Ødegaard, J. Stadsnes, A. Aasnes, and A. E. Zawedde (2016), Energetic electron precipitation into the middle atmosphere—Constructing the loss cone fluxes from MEPED POES, *Journal of Geophysical Research: Space Physics*, *121*(6), 5693–5707, doi:10.1002/2016JA022752. 3, 36, 37, 38, 49

Nesse Tyssøy, H., M. Sinnhuber, T. Asikainen, S. Bender, M. A. Clilverd, B. Funke, M. van de Kamp, J. M. Pettit, C. E. Randall, T. Reddmann, C. J. Rodger, E. Rozanov, C. Smith-Johnsen, T. Sukhodolov, P. T. Verronen, J. M. Wissing, and O. Yakovchuk (2022), HEPPA III Intercomparison Experiment on Electron Precipitation Impacts: 1. Estimated Ionization Rates During a Geomagnetic Active Period in April 2010, *Journal of Geophysical Research: Space Physics*, *127*(1), e2021JA029,128, doi:10.1029/2021JA029128. 2, 21, 29, 31, 32, 43

Newell, P., K. Liou, J. Gjerloev, T. Sotirelis, S. Wing, and E. Mitchell (2016), Substorm probabilities are best predicted from solar wind speed, *Journal of Atmospheric and Solar-Terrestrial Physics*, *146*, 28–37, doi:10.1016/j.jastp.2016.04.019. 19

Newell, P. T., and J. W. Gjerloev (2011), Evaluation of SuperMAG auroral electrojet indices as indicators of substorms and auroral power, *Journal of Geophysical Research (Space Physics)*, *116*(A15), A12211, doi:10.1029/2011JA016779. 41

Newell, P. T., and J. W. Gjerloev (2014), Local geomagnetic indices and the prediction of auroral power, *Journal of Geophysical Research: Space Physics*, *119*(12), 9790–9803, doi:https://doi.org/10.1002/2014JA020524. 28

Newell, P. T., and K. Liou (2011), Solar wind driving and substorm triggering, *Journal of Geophysical Research: Space Physics*, *116*(A3), doi:https://doi.org/10.1029/2010JA016139. 19

Newell, P. T., J. M. Ruohoniemi, and C.-I. Meng (2004), Maps of precipitation by source region, binned by imf, with inertial convection streamlines, *Journal of Geophysical Research: Space Physics*, *109*(A10), doi:https://doi.org/10.1029/2004JA010499. 27

Newell, P. T., T. Sotirelis, K. Liou, C.-I. Meng, and F. J. Rich (2007), A nearly universal solar wind-magnetosphere coupling function inferred from 10 magnetospheric state variables, *Journal of Geophysical Research: Space Physics*, *112*(A1), doi:https://doi.org/10.1029/2006JA012015. 19

Newnham, D. A., P. J. Espy, M. A. Clilverd, C. J. Rodger, A. Seppälä, D. J. Maxfield, P. Hartogh, K. Holmén, and R. B. Horne (2011), Direct observations of nitric oxide produced by energetic electron precipitation into the antarctic middle atmosphere, *Geophysical Research Letters*, *38*(20), doi:https://doi.org/10.1029/2011GL048666. 29

Partamies, N., F. Tesema, E. Bland, E. Heino, H. Nesse Tyssøy, and E. Kallelid (2021), Electron precipitation characteristics during isolated, compound, and multi-night substorm events, *Annales Geophysicae*, *39*(1), 69–83, doi:10.5194/angeo-39-69-2021. 31

Paulikas, G., and J. Blake (1979), *Effects of the Solar Wind on Magnetospheric Dynamics: Energetic Electrons at the Synchronous Orbit*, pp. 180–202, American Geophysical Union (AGU), doi:https://doi.org/10.1029/GM021p0180. 20

Pettit, J., S. Elliott, C. Randall, A. Halford, A. Jaynes, and K. Garcia-Sage (2023), Investigation of the drivers and atmospheric impacts of energetic electron precipitation, *Frontiers in Astronomy and Space Sciences*, *10*, doi:10.3389/fspas.2023.1162564. 29

Pettit, J. M., C. E. Randall, E. D. Peck, D. R. Marsh, M. van de Kamp, X. Fang, V. L. Harvey, C. J. Rodger, and B. Funke (2019), Atmospheric effects of >30-kev energetic electron precipitation in the southern hemisphere winter during 2003, *Journal of Geophysical Research: Space Physics*, *124*(10), 8138–8153, doi:10.1029/2019JA026868. 31

Pizzo, V. (1978), A three-dimensional model of corotating streams in the solar wind, 1. theoretical foundations, *Journal of Geophysical Research: Space Physics*, *83*(A12), 5563–5572, doi:https://doi.org/10.1029/JA083iA12p05563. 6

Plumb, R. A. (2002), Stratospheric transport, *Journal of the Meteorological Society of Japan. Ser. II*, *80*(4B), 793–809, doi:10.2151/jmsj.80.793. 24

Randall, C. E., V. L. Harvey, C. S. Singleton, S. M. Bailey, P. F. Bernath, M. Codrescu, H. Nakajima, and J. M. Russell III (2007), Energetic particle precipitation effects on the Southern Hemisphere stratosphere in 1992–2005, *Journal of Geophysical Research: Atmospheres*, *112*(D8), doi:10.1029/2006JD007696. 29

Randall, C. E., V. L. Harvey, L. A. Holt, D. R. Marsh, D. Kinnison, B. Funke, and P. F. Bernath (2015), Simulation of energetic particle precipitation effects during the

2003–2004 arctic winter, *Journal of Geophysical Research: Space Physics*, *120*(6), 5035–5048, doi:10.1002/2015JA021196. 29

Randel, W. J., and F. Wu (1999), Cooling of the arctic and antarctic polar stratospheres due to ozone depletion, *Journal of Climate*, *12*(5), 1467 – 1479, doi:10.1175/1520-0442(1999)012<1467:COTAAA>2.0.CO;2. 25

Reeves, G. D., S. K. Morley, R. H. W. Friedel, M. G. Henderson, T. E. Cayton, G. Cunningham, J. B. Blake, R. A. Christensen, and D. Thomsen (2011), On the relationship between relativistic electron flux and solar wind velocity: Paulikas and blake revisited, *Journal of Geophysical Research: Space Physics*, *116*(A2), doi: https://doi.org/10.1029/2010JA015735. 20

Richardson, I. G., and H. V. Cane (2012), Near-earth solar wind flows and related geomagnetic activity during more than four solar cycles (1963-2011), *J. Space Weather Space Climate*, *2*, doi:10.1051/swsc/2012003. 41

Rodger, C. J., M. A. Clilverd, J. C. Green, and M. M. Lam (2010), Use of poes sem-2 observations to examine radiation belt dynamics and energetic electron precipitation into the atmosphere, *Journal of Geophysical Research: Space Physics*, *115*(A4), doi: https://doi.org/10.1029/2008JA014023. 30, 37

Rodger, C. J., A. J. Kavanagh, M. A. Clilverd, and S. R. Marple (2013), Comparison between poes energetic electron precipitation observations and riometer absorptions: Implications for determining true precipitation fluxes, *Journal of Geophysical Research: Space Physics*, *118*(12), 7810–7821, doi:https://doi.org/10.1002/2013JA019439. 17, 18, 30

Rostoker, G., S.-I. Akasofu, J. Foster, R. Greenwald, Y. Kamide, K. Kawasaki, A. Lui, R. McPherron, and C. Russell (1980), Magnetospheric substorms—definition and signatures, *Journal of Geophysical Research: Space Physics*, *85*(A4), 1663–1668, doi: https://doi.org/10.1029/JA085iA04p01663. 11

Russell, C. T., and R. C. Elphic (1979), Isee observations of flux transfer events at the dayside magnetopause, *Geophysical Research Letters*, *6*(1), 33–36, doi:https://doi.org/10.1029/GL006i001p00033. 15

Salby, M. L., and P. F. Callaghan (2002), Interannual changes of the stratospheric circulation: Relationship to ozone and tropospheric structure, *Journal of Climate*, *15*(24), 3673 – 3685, doi:10.1175/1520-0442(2003)015<3673:ICOTSC>2.0.CO;2. 24

Salice, J. A., H. Nesse, E. M. Babu, C. Smith-Johnsen, and I. G. Richardson (2023), Exploring the predictability of the high-energy tail of mee precipitation based on solar wind properties, *Journal of Geophysical Research: Space Physics*, *128*(3), e2022JA031,194, doi:10.1029/2022JA031194. 31

Samtleben, N., C. Jacobi, P. Pišoft, P. Šácha, and A. Kuchař (2019), Effect of latitudinally displaced gravity wave forcing in the lower stratosphere on the polar vortex stability, *Annales Geophysicae*, *37*(4), 507–523, doi:10.5194/angeo-37-507-2019. 24

Sandanger, M. I., L.-K. G. Ødegaard, H. Nesse Tyssøy, J. Stadsnes, F. Søraas, K. Oksavik, and K. Aarsnes (2015), In-flight calibration of noaa poes proton detectors—derivation of the meped correction factors, *Journal of Geophysical Research: Space Physics*, *120*(11), 9578–9593, doi:https://doi.org/10.1002/2015JA021388. 37

Sarno-Smith, L. K. (2015), A Radiation Belt MeV Electron Flux Comparison Between RBE and GOES-15, *Research Gate*. 10, 11

Seppälä, A., H. Lu, M. A. Clilverd, and C. J. Rodger (2013), Geomagnetic activity signatures in wintertime stratosphere wind, temperature, and wave response, *Journal of Geophysical Research: Atmospheres*, *118*(5), 2169–2183, doi:10.1002/jgrd.50236. 1, 26

Seppälä, A., M. A. Clilverd, C. J. Rodger, P. T. Verronen, and E. Turunen (2008), The effects of hard-spectra solar proton events on the middle atmosphere, *Journal of Geophysical Research: Space Physics*, *113*(A11), doi:https://doi.org/10.1029/2008JA013517. 27

Seppälä, Annika (2007), Observations of production and transport of nox formed by energetic particle precipitation in the polar night atmosphere, Ph.D. thesis, Doctoral dissertation University of Otago. 25

Seviour, W. J. M., D. M. Mitchell, and L. J. Gray (2013), A practical method to identify displaced and split stratospheric polar vortex events, *Geophysical Research Letters*, *40*(19), 5268–5273, doi:https://doi.org/10.1002/grl.50927. 23

Sinnhuber, H., M.and Nieder, and N. Wieters (2012), Energetic Particle Precipitation and the Chemistry of the Mesosphere/Lower Thermosphere, *Surveys in Geophysics*, *33*, 1281–1334, doi:10.1007/s10712-012-9201-3. 26, 28

Sinnhuber, M., S. Kazeminejad, and J. M. Wissing (2011), Interannual variation of nox from the lower thermosphere to the upper stratosphere in the years 1991–2005, *Journal of Geophysical Research: Space Physics*, *116*(A2), doi:10.1029/2010JA015825. 2, 28, 29

Sinnhuber, M., B. Funke, T. von Clarmann, M. Lopez-Puertas, G. P. Stiller, and A. Seppälä (2014), Variability of no$_x$ in the polar middle atmosphere from october 2003 to march 2004: vertical transport vs. local production by energetic particles, *Atmospheric Chemistry and Physics*, *14*(14), 7681–7692, doi:10.5194/acp-14-7681-2014. 29

Sinnhuber, M., U. Berger, B. Funke, H. Nieder, T. Reddmann, G. Stiller, S. Versick, T. von Clarmann, and J. M. Wissing (2018), No_y production, ozone loss and changes in net radiative heating due to energetic particle precipitation in 2002–2010, *Atmospheric Chemistry and Physics*, *18*(2), 1115–1147, doi:10.5194/acp-18-1115-2018. 26

Sinnhuber, M., H. Nesse Tyssøy, T. Asikainen, S. Bender, B. Funke, K. Hendrickx, J. M. Pettit, T. Reddmann, E. Rozanov, H. Schmidt, C. Smith-Johnsen, T. Sukhodolov, M. E. Szeląg, M. van de Kamp, P. T. Verronen, J. M. Wissing, and O. S. Yakovchuk (2022), Heppa iii intercomparison experiment on electron precipitation impacts: 2. model-measurement intercomparison of nitric oxide (no) during a geomagnetic storm in april 2010, *Journal of Geophysical Research: Space Physics*, *127*(1), e2021JA029,466, doi:10.1029/2021JA029466. 21, 31

Smith-Johnsen, C., H. Nesse Tyssøy, K. Hendrickx, Y. Orsolini, G. Kishore Kumar, L.-K. G. Ødegaard, M. I. Sandanger, F. Stordal, and L. Megner (2017), Direct and indirect electron precipitation effect on nitric oxide in the polar middle atmosphere, using a full-range energy spectrum, *Journal of Geophysical Research: Space Physics*, *122*(8), 8679–8693, doi:10.1002/2017JA024364. 29

Solomon, S., D. Rusch, J. Gérard, G. Reid, and P. Crutzen (1981), The effect of particle precipitation events on the neutral and ion chemistry of the middle atmosphere: Ii. odd hydrogen, *Planetary and Space Science*, *29*(8), 885–893, doi:https://doi.org/10.1016/0032-0633(81)90078-7. 26

Solomon, S., P. J. Crutzen, and R. G. Roble (1982), Photochemical coupling between the thermosphere and the lower atmosphere: 1. Odd nitrogen from 50 to 120 km, *Journal of Geophysical Research: Oceans*, *87*(C9), 7206–7220, doi:10.1029/JC087iC09p07206. 26, 28

Summers, D., R. M. Thorne, and F. Xiao (1998), Relativistic theory of wave-particle resonant diffusion with application to electron acceleration in the magnetosphere, *Journal of Geophysical Research: Space Physics*, *103*(A9), 20,487–20,500, doi:https://doi.org/10.1029/98JA01740. 15, 19

Theodoridis, G. C., and F. R. Paolini (1967), Pitch Angle Diffusion of Relativistic Outer Belt Electrons, *Ann. Geophys.*, pp. 375–381. 37

Tsurutani, B. T., W. D. Gonzalez, A. L. C. Gonzalez, F. L. Guarnieri, N. Gopalswamy, M. Grande, Y. Kamide, Y. Kasahara, G. Lu, I. Mann, R. McPherron, F. Soraas, and V. Vasyliunas (2006), Corotating solar wind streams and recurrent geomagnetic activity: A review, *Journal of Geophysical Research: Space Physics*, *111*(A7), doi: https://doi.org/10.1029/2005JA011273. 12

Tyssøy, H. N., A. Haderlein, M. I. Sandanger, and J. Stadsnes (2019), Intercomparison of the poes/meped loss cone electron fluxes with the cmip6 parametrization, *Journal of Geophysical Research: Space Physics*, *124*(1), 628–642, doi:10.1029/2018JA025745. 2, 31, 43, 45

Tyssøy, H. N., N. Partamies, E. M. Babu, C. Smith-Johnsen, and J. A. Salice (2021), The predictive capabilities of the auroral electrojet index for medium energy electron precipitation, *Frontiers in Astronomy and Space Sciences*, *8*, doi:10.3389/fspas.2021.714146. 31, 32, 38, 44, 51

van de Kamp, M., A. Seppälä, M. A. Clilverd, C. J. Rodger, P. T. Verronen, and I. C. Whittaker (2016), A model providing long-term data sets of energetic electron precipitation during geomagnetic storms, *Journal of Geophysical Research: Atmospheres*, *121*(20), 12,520–12,540, doi:10.1002/2015JD024212. 31, 38, 44

van de Kamp, M., C. J. Rodger, A. Seppälä, M. A. Clilverd, and P. T. Verronen (2018), An updated model providing long-term data sets of energetic electron precipitation, including zonal dependence, *Journal of Geophysical Research: Atmospheres*, *123*(17), 9891–9915, doi:10.1029/2017JD028253. 31, 42

Watson, P. A. G., and L. J. Gray (2014), How does the quasi-biennial oscillation affect the stratospheric polar vortex?, *Journal of the Atmospheric Sciences*, *71*(1), 391 – 409, doi:10.1175/JAS-D-13-096.1. 24

Waugh, D. W., A. H. Sobel, and L. M. Polvani (2017), What is the polar vortex and how does it influence weather?, *Bulletin of the American Meteorological Society*, *98*(1), 37 – 44, doi:10.1175/BAMS-D-15-00212.1. 22, 23

Winningham, J. D., J. R. Sharber, R. A. Frahm, J. L. Burch, N. Eaker, R. K. Black, V. A. Blevins, J. P. Andrews, J. Rudzki, M. J. Sablik, D. L. Chenette, D. W. Datlowe, E. E. Gaines, W. I. Imhof, R. W. Nightingale, J. B. Reagan, R. M. Robinson, T. L. Schumaker, E. G. Shelley, R. R. Vondrak, H. D. Voss, P. F. Bythrow, B. J. Anderson, T. A. Potemra, L. J. Zanetti, D. B. Holland, M. H. Rees, D. Lummerzheim, G. C. Reid, R. G. Roble, C. R. Clauer, and P. M. Banks (1993), The uars particle environment monitor, *Journal of Geophysical Research: Atmospheres*, *98*(D6), 10,649–10,666, doi: https://doi.org/10.1029/93JD00461. 30

Woollings, T., C. Li, M. Drouard, E. Dunn-Sigouin, K. A. Elmestekawy, M. Hell,

B. Hoskins, C. Mbengue, M. Patterson, and T. Spengler (2023), The role of rossby waves in polar weather and climate, *Weather and Climate Dynamics*, *4*(1), 61–80, doi:10.5194/wcd-4-61-2023. 23

Xu, W., R. A. Marshall, H. N. Tyssøy, and X. Fang (2020), A generalized method for calculating atmospheric ionization by energetic electron precipitation, *Journal of Geophysical Research: Space Physics*, *125*(11), e2020JA028,482, doi:10.1029/2020JA028482. 28, 29

Yando, K., R. M. Millan, J. C. Green, and D. S. Evans (2011), A Monte Carlo simulation of the NOAA POES Medium Energy Proton and Electron Detector instrument, *Journal of Geophysical Research: Space Physics*, *116*(A10), doi:10.1029/2011JA016671. 36

Yasyukevich, A. S., M. A. Chernigovskaya, B. G. Shpynev, D. S. Khabituev, and Y. V. Yasyukevich (2022), Features of winter stratosphere small-scale disturbance during sudden stratospheric warmings, *Remote Sensing*, *14*(12), doi:10.3390/rs14122798. 24

Yuan, C. J., and Q.-G. Zong (2012), Quantitative aspects of variations of 1.5–6.0 mev electrons in the outer radiation belt during magnetic storms, *Journal of Geophysical Research: Space Physics*, *117*(A11), doi:https://doi.org/10.1029/2011JA017346. 20

Zawedde, A. E., H. Nesse Tyssøy, J. Stadsnes, and M. I. Sandanger (2018), The Impact of Energetic Particle Precipitation on Mesospheric OH – Variability of the Sources and the Background Atmosphere, *Journal of Geophysical Research: Space Physics*, *123*(7), 5764–5789, doi:10.1029/2017JA025038. 27

Zhang, Y., and L. Paxton (2008), An empirical kp-dependent global auroral model based on timed/guvi fuv data, *Journal of Atmospheric and Solar-Terrestrial Physics*, *70*(8), 1231–1242, doi:https://doi.org/10.1016/j.jastp.2008.03.008. 28

Zhao, H., D. Baker, X. Li, D. Malaspina, A. Jaynes, and S. Kanekal (2019), On the acceleration mechanism of ultrarelativistic electrons in the center of the outer radiation belt: A statistical study, *Journal of Geophysical Research: Space Physics*, *124*(11), 8590–8599, doi:https://doi.org/10.1029/2019JA027111. 16

Zurbuchen, T. H., and I. G. Richardson (2006), In-situ solar wind and magnetic field signatures of interplanetary coronal mass ejections, *Space Science Reviews*, *123*(1), 31–43, doi:10.1007/s11214-006-9010-4. 6

Zúñiga López, H. D., H. N. Tyssøy, C. Smith-Johnsen, and V. Maliniemi (2022), The Direct Effect of Medium Energy Electron Precipitation on Mesospheric Dynamics

During a Sudden Stratospheric Warming Event in 2010, *Geophysical Research Letters*, *49*(13), e2022GL097,812, doi:10.1029/2022GL097812. 29, 31

Ødegaard, L.-K. G., H. N. Tyssøy, M. I. J. Sandanger, J. Stadsnes, and F. Søraas (2016), Space weather impact on the degradation of noaa poes meped proton detectors, *J. Space Weather Space Clim.*, *6*, A26, doi:10.1051/swsc/2016020. 37

Ødegaard, L.-K. G., H. N. Tyssøy, F. Søraas, J. Stadsnes, and M. I. Sandanger (2017), Energetic electron precipitation in weak to moderate corotating interaction region-driven storms, *Journal of Geophysical Research: Space Physics*, *122*(3), 2900–2921, doi:10.1002/2016JA023096. 32, 36

Østgaard, N. and J. Stadsnes and J. Bjordal and R. R. Vondrak and S. A. Cummer and D. L. Chenette and G. K. Parks and M. J. Brittnacher and D. L. McKenzie (1999), Global-scale electron precipitation features seen in uv and x rays during substorms, *Journal of Geophysical Research: Space Physics*, *104*(A5), 10,191–10,204, doi:https://doi.org/10.1029/1999JA900004. 30

Scientific Results

Paper I

Exploring the Predictability of the High-Energy Tail of MEE Precipitation Based on Solar Wind Properties

J. Salice, H. Nesse, E. M. Babu, C. Smith-Johnsen, and I. G. Richardson

JGR Space Physics, **128/Issue 3** (2023). doi: 10.1029/2022JA031194

JGR Space Physics

RESEARCH ARTICLE
10.1029/2022JA031194

Key Points:

- The solar wind parameter ε best predicts the peak flux of the >292 keV electron precipitation independent of solar wind structure
- The delay in the peak flux of >292 keV electron precipitation relative to that of >43 keV electrons is influenced by solar wind speed
- On average, electron precipitation >292 keV persists 2–3 days longer than electron precipitation >43 keV

Correspondence to:
J. A. Salice,
Josephine.Salice@uib.no

Citation:
Salice, J. A., Nesse, H., Babu, E. M., Smith-Johnsen, C., & Richardson, I. G. (2023). Exploring the predictability of the high-energy tail of MEE precipitation based on solar wind properties. *Journal of Geophysical Research: Space Physics*, *128*, e2022JA031194. https://doi.org/10.1029/2022JA031194

Received 29 NOV 2022
Accepted 1 MAR 2023

The copyright line for this article was changed on 29 MAR 2023 after original online publication.

Exploring the Predictability of the High-Energy Tail of MEE Precipitation Based on Solar Wind Properties

J. A. Salice[1], H. Nesse[1], E. M. Babu[1], C. Smith-Johnsen[1], and I. G. Richardson[2,3]

[1]Birkeland Centre for Space Science, Department of Physics and Technology, University of Bergen, Bergen, Norway, [2]Heliophysics Science Division, NASA Goddard Space Flight Center, Greenbelt, MD, USA, [3]Department of Astronomy, University of Maryland, College Park, MD, USA

Abstract Medium Energy Electron (MEE) precipitation ($\gtrsim$30 keV) ionizes the mesosphere and initiates chemical reactions, which ultimately can reduce mesospheric and stratospheric ozone. Currently, there are considerable differences in how existing parameterizations represent flux response, timing, and duration of MEE precipitation, especially considering its high-energy tail ($\gtrsim$300 keV). This study compares the nature of $\gtrsim$300 to $\gtrsim$30 keV electron fluxes to better understand differences within MEE precipitation. The MEE fluxes are estimated from measurements by the Medium Energy Proton and Electron Detector (MEPED) onboard the Polar Orbiting Environmental Satellite (POES) from 2004 to 2014. The fluxes are explored in the context of solar wind drivers: corotating high-speed solar wind streams (HSSs) and coronal mass ejections (CMEs) alongside their associated solar wind properties. Three key aspects of $\gtrsim$300 keV electron fluxes are investigated: maximum response, peak timing, and duration. The results reveal a structure-dependent correlation (0.89) between the peak fluxes of $\gtrsim$30 and $\gtrsim$300 keV electrons. The epsilon coupling function correlates well (0.84) with the $\gtrsim$300 keV peak flux, independent of solar wind structure. The $\gtrsim$300 keV flux peaks 0–3 days after the $\gtrsim$30 keV flux peaks. The highest probability (~42%) occurs for a 1-day delay, while predictive capabilities increase when accounting for solar wind speed. The $\gtrsim$300 keV flux response has the highest probability of lasting 4 days for both CMEs and HSSs. The results form a base for a stochastic MEE parameterization that goes beyond the average picture, enabling realistic flux variability on both daily and decadal scales.

Plain Language Summary Electrons with energies >30 keV precipitating into the Earth's atmosphere is known as medium energy electron (MEE) precipitation. Solar wind properties drive the rate and energy of MEE. MEE precipitation is a relevant solar forcing as it produces ozone-depleting substances. Variations in ozone concentration can modify the atmospheric temperature profile and lead to changes in atmospheric circulation that can map down onto surface climate. The community's capability of parameterizing MEE precipitation is an active field of research. This study aims to build a foundation for an MEE parameterization that represents realistic variability on daily and decadal scales by exploring the variability in the context of different solar wind properties. The study focuses on three key aspects regarding the differences within the energy spectrum of MEE precipitation: maximum response, timing, and duration. The key aspects are evaluated regarding the probability of a specific response. This study looks at an entire solar cycle (11 yr). It is found that solar wind properties, such as solar wind speed, can help determine the probability of a particular MEE response. The results from this paper will be key elements for constructing an MEE precipitation parameterization to be applied in a chemistry-climate model.

1. Introduction

Energetic particle precipitation (EPP) causes chemical changes in the upper atmosphere ($\gtrsim$50 km), for example, by creating NO_x and HO_x gasses (e.g., Smith-Johnsen et al., 2017; Verronen & Lehmann, 2013; Verronen et al., 2006; Zawedde et al., 2018). The increase of NO_x is particularly significant due to its long lifetime during high-latitude winter darkness, allowing for downward transportation and depletion of stratospheric ozone (Damiani et al., 2016; Maliniemi et al., 2021; Solomon et al., 1982). Ozone plays a significant role in stabilizing the atmosphere's radiation balance and climate system by absorbing incoming solar radiation and emitting long-wave infrared radiation. Hence, variation in ozone will cause changes in the atmospheric temperature profile and lead to changes in atmospheric circulation that can potentially map down onto surface climate (Baldwin & Dunkerton, 2001; Kidston et al., 2015; Maliniemi et al., 2016; Seppälä et al., 2016). The strengths of the atmospheric ionization rates and chemical modulation highly depend on the number, energy, and type of particles hitting the atmosphere.

EPP consists of both protons and electrons. Auroral electron ($\lesssim$30 keV) and proton ($\lesssim$1 MeV) precipitation originating from the plasma sheet will ionize the lower thermosphere and upper mesosphere. Medium energy electrons (MEEs; $\gtrsim$30 keV) from the radiation belts deposit their energy throughout the upper mesosphere, whereas the high-energy tail of MEE ($\gtrsim$300 keV) can reach the upper stratosphere (Turunen et al., 2009). Occasionally, high-energetic precipitating protons from solar proton events (SPEs; 1–50 MeV) can ionize the stratosphere, where the production of NO_x and HO_x allows for a direct impact on stratospheric ozone (Jackman et al., 2005; Tyssøy & Stadsnes, 2015; Tyssøy et al., 2013; Zawedde et al., 2018).

The link between electron precipitation at auroral energies and how it affects NO_x in the lower thermosphere is well established (Marsh et al., 2004; Sinnhuber et al., 2011). Similarly, the effects of SPEs are fairly well quantified (Funke et al., 2011; Jackman et al., 2005; Tyssøy & Stadsnes, 2015; Tyssøy et al., 2013). However, knowledge gaps remain regarding the MEE precipitation spectrum, particularly when considering the high-energy tail. MEE precipitation is acknowledged as one of the relevant factors in understanding stratospheric ozone depletion (Matthes et al., 2017). Currently, the community's capability of parameterizing MEE precipitation is an active field of research (Babu et al., 2022; Beharrell et al., 2015; Duderstadt et al., 2021; Mironova et al., 2019; Partamies et al., 2021; Pettit et al., 2019; Tyssøy et al., 2019; Tyssøy, Partamies, Babu, Smith-Johnsen, & Salice, 2021; Tyssøy et al., 2021; van de Kamp et al., 2018, 2016). Instrumental challenges and different data handling result in a wide range of electron flux and ionization rate estimates (Tyssøy et al., 2021). This uncertainty propagates into chemistry-climate model projections of the associated chemical effects (Sinnhuber et al., 2022).

Geomagnetic indices are often used as proxies for precipitation. The lower part of the electron precipitation spectrum is known to correspond well with geomagnetic indices (e.g., Hendrickx et al., 2015; Østgaard et al., 2002; Y. Zhang & Paxton, 2008). The high-energy tail of MEE precipitation is more ambiguous (Turunen et al., 2009; Tyssøy, Babu, Smith-Johnsen, & Salice, 2021). The Coupled Model Intercomparison Project Phase 6 (CMIP6) provides climate projections in a multi-model context (WCRP, 2011). The current CMIP6 solar forcing recommendation utilizes van de Kamp et al. (2016)'s daily resolved model for MEE precipitation (Matthes et al., 2017). The model is based on the 0° Medium Energy Proton and Electron Detector (MEPED) measurements onboard the NOAA Polar Orbiting Environmental Satellites (POES) and is scaled by the Ap index. Several limitations to this approach have been established (e.g., Mironova et al., 2019; Pettit et al., 2019; Tyssøy et al., 2019; Tyssøy et al., 2021).

Tyssøy et al. (2019) find that the Ap-based model falls short in reproducing flux levels, variability associated with strong geomagnetic storms, and the duration of storms. Typically, the high-energy tail of MEE acts differently compared to the lower energies with respect to the timing (Ødegaard et al., 2017) and duration (Longden et al., 2008) of the flux response. Moreover, as the parameterization developed in van de Kamp et al. (2016) is based on an average response to geomagnetic activity, it is likely to downplay the impact of extreme events (Tyssøy et al., 2021). To model the effect of the transient forcing of MEE on the atmosphere, a correct representation of the daily MEE variability over a wide range of energies with respect to both the background drizzle and storm periods is necessary. Additionally, an average representation of the typical storm might not reflect the variability throughout a solar cycle. In particular, the solar wind drivers of MEE exhibit a fairly strong solar cycle dependence (e.g., Asikainen & Ruopsa, 2016; Kilpua, Balogh, et al., 2017; Kilpua, Koskinen, et al., 2017), potentially causing a systematic bias on decadal scales (Tyssøy et al., 2019). An accurate representation of MEE precipitation will allow for better parameterization on both daily and decadal scales.

The solar wind fuels the magnetospheric processes that accelerate and scatter electrons trapped in the radiation belts. Coronal mass ejections (CMEs) and high-speed solar wind streams (HSSs) are the primary large-scale heliospheric solar wind structures driving geomagnetic disturbances (e.g., J. Zhang et al., 2007). These structures occasionally occur in rapid sequences or are merged, leading to intense geomagnetic disturbances (Asikainen & Ruopsa, 2016; Kilpua, Balogh, et al., 2017; Kilpua, Koskinen, et al., 2017). CMEs consist of various components such as shocks, sheaths, ejecta, and clouds (for reviews on CMEs, see e.g., Kilpua, Balogh, et al., 2017; Kilpua, Koskinen, et al., 2017; Zurbuchen & Richardson, 2006). HSSs are often accompanied by a corotating interaction region (CIR) leading the stream (for a review on HSSs and CIRs, see Richardson, 2018). Generally, CMEs tend to be brief (~1 day) and may include strong, slowly varying magnetic field components, while HSSs tend to last longer and have fluctuating magnetic field components (e.g., Borovsky & Denton, 2006; Kataoka &

Miyoshi, 2006; Kilpua, Balogh, et al., 2017; Kilpua, Koskinen, et al., 2017). Throughout a solar cycle, HSSs are nearly always (except at solar maxima) more frequent than CMEs (Asikainen & Ruopsa, 2016). The fundamentally different solar wind properties drive different geomagnetic disturbances as well as different MEE precipitation characteristics (e.g., Borovsky & Denton, 2006; Longden et al., 2008).

This study explores daily MEE precipitation in the context of its solar wind drivers and the associated solar wind properties, such as solar wind speed and interplanetary magnetic field (IMF). Notably, the focus is on the behavior of the high-energy tail compared to low-energy MEE precipitation. The low-energy MEE is generally easier to quantify due to its high correspondence to geomagnetic activity in contrast to the high-energy tail. The MEE bounce loss cone (BLC) fluxes are estimated based on observations from MEPED onboard POES/METOP over 11 yr from 2004 to 2014. Periods of isolated CME- and HSS-driven solar wind structures and periods when they are in close sequence are examined. Three key aspects of ≳300 keV electron flux are investigated:

- The maximum flux response.
- The timing of the maximum flux response.
- The duration of the flux response.

Table 1
Nominal Detector Responses in the Three Electron Channels E1, E2, and E3 of the SEM-2 MEPED Electron Detector (Evans & Greer, 2004) and the New Optimized Integral Energy Limit for the Different Channels (Ødegaard et al., 2017)

Energy channel	Nominal lower limit [keV]	New optimized lower limit [keV]
E1	>30	>43
E2	>100	>114
E3	>300	>292

The key aspects are evaluated regarding the probability of a specific response. The goal is to identify variables that increase the accuracy of a daily MEE parameterization to be applied in a chemistry-climate model. This paper is organized as follows: Section 2 describes the data and methods used, Section 3 presents the results which are discussed in Section 4, and finally, conclusions of this study are provided in Section 5.

2. Data and Method

2.1. MEE Flux

The series of NOAA/POES and EUMETSAT/MetOp satellites are Sun-synchronous, low-altitude polar-orbiting spacecraft. The spacecraft circle at ∼850 km altitude with a period of ∼100 min, resulting in 14–15 orbits per day (Evans & Greer, 2004). The MEPED instrument is mounted on the POES series and three of the MetOp spacecraft. The combined measurements from the different satellites give a near-continuous observation of MEE precipitation from 1979 until today.

MEPED consists of a set of eight separate solid-state particle detector systems. Two are proton solid-state detector telescopes, two are electron solid-state detector telescopes, and the remaining four are omni-directional detector systems for high-energy protons measured over a wide range of angles (Evans & Greer, 2004). The electron detectors monitor the intensity of electrons in three bands from 30 to 2,500 keV (Evans & Greer, 2004). The nominal electron energy limits for the electron telescope in the three bands E1, E2, and E3 as given in Evans and Greer (2004) are listed in Table 1. When in operation, the true electron energy limits depend on the incoming electron energy spectrum (Yando et al., 2011). The new optimized effective integral energy limits and associated geometric factors are based on a series of realistic power laws and exponential spectra and were determined by Ødegaard et al. (2017) by applying the geometric factors given in Yando et al. (2011).

The electron solid-state detector telescopes consist of a 0° and 90° telescope. The 0° telescope is oriented radially outward along the Earth-satellite connecting axis. The 90° telescope is perpendicular to the 0° telescope and anti-parallel to the satellite's velocity vector. Both telescopes are rotated away from the described axis by 9° to ensure a clear field of view (Evans & Greer, 2004). Charged particles gyrate along the magnetic field lines. The angle between the velocity vector of a particle and the magnetic field line is known as the particle's pitch angle. This angle determines whether the particle will be lost to the atmosphere or mirrored back along the magnetic field. The atmospheric BLC is defined as the range of pitch angles at which particles will be lost. The size of the BLC changes with latitude and longitude due to variations in the magnetic field strength. In MEPED, the 0° telescopes will mainly measure atmospheric BLC particles when traveling across high geomagnetic latitude, while the 90° telescopes will mainly measure particles at the edge or outside of the BLC (Rodger et al., 2010).

Separately, the two telescopes do not give an accurate estimate of the BLC electron flux (Tyssøy et al., 2016) as the 90° telescope will give an overestimation and the 0° telescope an underestimation. This is because the energetic electron fluxes are often strongly anisotropic with decreasing fluxes toward the center of the BLC (Tyssøy et al., 2016). Tyssøy et al. (2016) estimated a complete BLC flux for each electron energy channel by combining measurements from both telescopes with electron pitch angle distributions from theories of wave-particle interactions in the magnetosphere. The Focker-Planck equation for particle diffusion (Kennel & Petschek, 1966; Theodoridis & Paolini, 1967) is solved for a wide range of diffusion coefficients. The solutions are then transformed to the satellite altitude and stored in a look-up table. The ratio between the fluxes detected by the 0° and 90° detector is compared to the theoretical solution considering the telescope's viewing directions relative to the magnetic field. Finally, the size of the BLC is predicted based on the International Geomagnetic Reference Field model and is applied to estimate the precipitating fluxes. The BLC flux estimate is done separately for each energy channel, as the level of particle diffusion will vary with energy. A detailed explanation of the method can be found in Tyssøy et al. (2016).

This study applies the BLC fluxes with the new optimized effective integral limits E1 (>43 keV) and E3 (>292 keV). The BLC fluxes represent daily fluxes averaged over 55°–75° corrected geomagnetic (CGM) latitude and all magnetic local times for a full solar cycle from 2004 to 2014. During this period, up to seven satellites have been operational, all with the newest instrument package SEM-2. More details of the operating satellites and data coverage for the specific time period can be found in Babu et al. (2022) and Tyssøy, Partamies, Babu, Smith-Johnsen, and Salice (2021). For simplicity, >43 and >292 keV electron fluxes will be referred to as E1 and E3, respectively.

2.2. Solar Wind Structure and Parameters

The near-Earth solar wind is divided into three basic flow types:
- Corotating high-speed streams that originate from coronal holes at the Sun.
- Transient flows associated with CMEs at the Sun.
- Slower, interstream solar wind typically associated with the streamer belt at the Sun.

Classification of these three structures for every day of the 11 yr period from 2004 to 2014 was made using the same methods discussed by Richardson and Cane (2012). Their list of daily resolution solar wind structures, based on a 1 hr resolution assessment of these structures, includes the day the structure starts to the day it ends, even if that solar wind structure did not predominately occur on these days. The classifications are based on a variety of data, including near-Earth solar wind parameters from the OMNI database, geomagnetic activity data, and energetic (∼0.1–100 MeV) particle and cosmic ray observations (Richardson & Cane, 2012). Since the near-Earth solar wind data is essentially continuous throughout the investigated period, Richardson and Cane (2012)'s classifications are considered representative and suitable for this study.

The corotating high-speed streams, denoted as HSSs in this paper, typically have solar wind speed $v \gtrsim 450$ km/s and include both the high-speed stream and CIR where the leading edge of the high-speed stream interacts with the preceding slower, cooler, and denser solar wind. The transient flows originating with CMEs at the Sun include interplanetary CMEs (ICMEs), the manifestations in the solar wind of the CMEs, and the associated upstream shocks and post-shock/sheath regions (Richardson & Cane, 2012). Richardson and Cane (2012) refer to ICMEs and their upstream shocks and sheaths collectively as "CME-associated" structures. This paper follows the same approach and, for brevity, uses "CME" to refer to these structures. More information on the respective data sets and how the different structures are identified can be found in Richardson and Cane (2012) and references therein.

The solar wind magnetic field strength and direction as well as the solar wind speed are primary drivers of geomagnetic activity. In this paper, the IMF component Bz (in GSM-coordinates) and plasma flow speed, v, were retrieved from the OMNI 2 database with a daily resolution from 2004 to 2014. In addition, the epsilon parameter, ϵ, which is based on Bz and v and which gives a general idea of the energy transfer between the solar wind and the magnetosphere, was retrieved from the SuperMAG database (Gjerloev, 2012) with daily resolution over the same time interval. ϵ is given by:

$$\epsilon = \frac{4\pi}{\mu_0} v B^2 sin^4\left(\frac{\theta}{2}\right) l_0^2 \qquad (1)$$

Equation 1 is based on Akasofu (1981) and is given in SI units (Watt) by Koskinen and Tanskanen (2002). In Equation 1, $4\pi/\mu_0 = 10^7$, v is solar wind velocity, B is the magnitude of the solar wind magnetic field, θ is the clock angle (the angle between geomagnetic north and the projection of the IMF in the plane transverse to the radial direction), and l_0 is seven times the Earth's radius ($l_0 = 7R_E$).

The current parameterization for MEE precipitation recommended for CMIP6 is represented as daily averages based on daily Ap values (Matthes et al., 2017). Moreover, the high-energy tail of the MEE spectra often peaks after 1–2 days (Ødegaard et al., 2017; Tyssøy, Partamies, Babu, Smith-Johnsen, & Salice, 2021). Because of this, the goal of our study is not to attempt to understand the role of solar wind drivers over short time intervals but to reveal their stochastic role in the behavior of precipitating the high-energy tail of MEE. Tyssøy, Partamies, Babu, Smith-Johnsen, and Salice (2021) demonstrate that the MEE precipitating fluxes are determined by accumulated geomagnetic activity. As such, it is not the specific short periods of negative Bz or positive ϵ that determine the daily MEE precipitation. Hence, we apply daily averages of the hourly determined solar wind structures, the 1 min Bz, v, and ϵ parameters alongside daily averaged MEE fluxes.

2.3. Method

In this study, CMEs and HSSs are categorized into single and combined events. The combinations of events include a CME followed by an HSS and vice versa. In the 11 yr of interest, 420 events were selected based on the requirements that they were classified as a structure for at least 1 day and had slower, interstream solar wind the day before and after. However, 12 events were removed because of gaps in the electron flux data. Additionally, 52 events with fluxes falling below 250 electrons/($\mathrm{cm}^2 \cdot \mathrm{s} \cdot \mathrm{sr}$) were removed because they were close to the detectors noise level of around 100 electrons/($\mathrm{cm}^2 \cdot \mathrm{s} \cdot \mathrm{sr}$). Moreover, 107 events, where either E1 or E3 reached their highest flux before the solar wind event, were removed. These events would have given misleading flux responses, as this study evaluates the electron fluxes within the solar wind structure and does not consider pre-event fluxes. Based on these criteria, 249 events within the 11 yr period were retained: 34 CMEs, 181 HSSs, 17 CME + HSSs, and 17 HSS + CMEs.

Figure 1 shows a superposed epoch analysis (SEA) over a 14-day period of E1 and E3 as well as the parameters Bz, v, and ϵ for all 249 events, denoted as the Base. The onset is defined by the peak in E1. Previous studies have shown that the E1 evolution and maximum flux response are fairly well correlated with geomagnetic activity (Tyssøy, Partamies, Babu, Smith-Johnsen, & Salice, 2021; van de Kamp et al., 2016). The evolution of E1 and the three solar wind parameters in Figure 1 confirms this correlation. Hence, this study targets the behavior of the E3 peak relative to the E1 peak and, therefore, defines the onset based on E1. In addition, choosing the flux peak instead of flux rise avoids the pitfall of MEE radiation belt fluxes being subject to adiabatic variability where it is not always evident when the flux rise starts (Ødegaard et al., 2017). Moreover, the peak flux is a pragmatic parameter to apply in a model assuming a fairly consistent rise time. In this study, the peak fluxes refer to the highest flux response within the solar wind structure period.

Figure 1 captures the long duration of elevated fluxes, particularly for E3. Note that other events may occur during the 8 days following onset, which can give rise to some of the features in the SEA. When evaluating the E3 peak, as well as the delay between E1 and E3, activity throughout the 8-day period after the onset does not affect the interpretations. However, when evaluating the duration, events with activity throughout the 8-day period after the onset are discarded (see Section 3.4).

Under the assumption that it is the accumulated effect of solar wind drivers that is responsible for E3 characteristics, we apply a 4-day average of the three parameters Bz, v, and ϵ from 2 days before the onset (−2 days) to 1 day after (+1 day). This captures the main energy transfer period as illustrated by ϵ in the lower panel of Figure 1, which occurs before the average E3 peak. The respective time interval is optimized and confirmed based on regression analysis between E3 and different time intervals for ϵ. Note that Bz averages out around zero as it oscillates between negative and positive values throughout the day. A daily average will not capture the oscillation but can still indicate if Bz was more negative or positive throughout the day and if large negative values occur.

SEAs of the flux response in the E1 (black) and E3 (green) flux channels during the different events are presented in Figure 2. The top panel shows Base events and gives a general picture of how active solar wind periods affect electron precipitation. The four subsequent panels show the flux evolution during CMEs, HSSs, CME + HSSs, and HSS + CMEs. As HSSs make up ~73% of all the events, they will correspond well with the Base. All five panels list the E1 and E3 peaks with the associated timings. In addition, the transition between structures within the combined events is marked on the upper x-axis. Note that one HSS + CME event does not change from an HSS-driven structure to a CME-driven one until after the plotted period of 8 days from onset. This event is not disregarded as we do not differentiate between electron fluxes reaching their peak in a certain structure of the combined events.

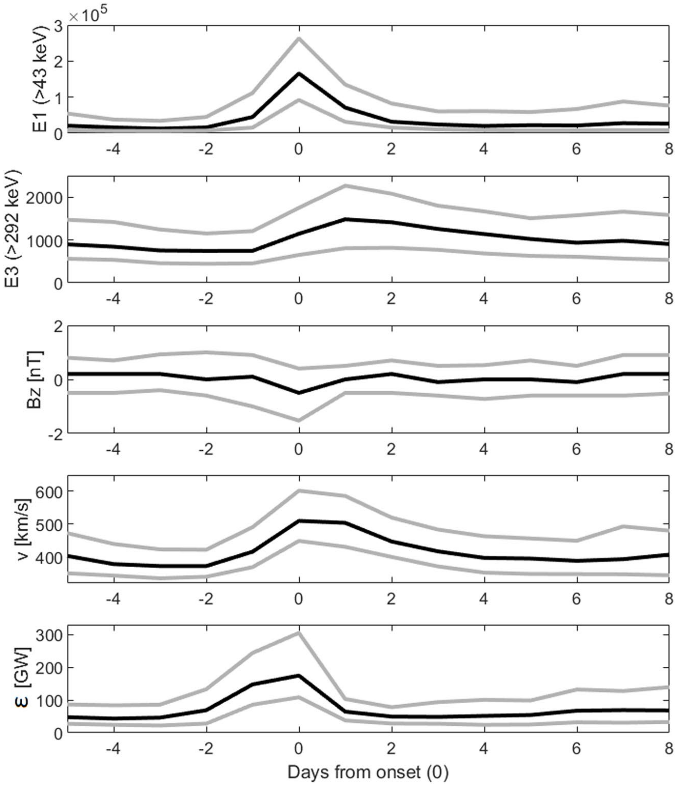

Figure 1. Superposed epoch analysis of the evolution of parameters for all events in this study (Base). From the top: E1 (>43 keV), E3 (>292 keV), Bz, v, and ϵ. The fluxes are in $cm^{-2}s^{-1}sr^{-1}$. The onset is defined as the E1 maximum flux response within the solar wind structure period (denoted as the E1 peak). The gray lines show the lower and upper quartiles.

The electron flux channels E1 and E3 represent two different energy intervals within the MEE range, the latter being the high-energy tail. As the magnetospheric acceleration and scattering processes are energy-dependent (Millan & Thorne, 2007), it is expected that the nature of particles precipitating at these two energy intervals also differs. The E1 maximum response is higher as it not only represents an integral spectrum but naturally has a higher flux due to the flux always decreasing with higher energy. However, it is evident that the broadness of the E1 and E3 peaks typically differs. A prolonged E3 response implies a significant accumulated effect. More time is needed to accelerate and scatter electrons at higher energies (>292 keV) which can lead to a delay in the E3 response compared to that of E1 (Ødegaard et al., 2017; Tyssøy, Partamies, Babu, Smith-Johnsen, & Salice, 2021). As solar wind drives the acceleration and scattering processes of electrons in the magnetosphere, this study will examine to which degree different solar wind structures generate different characteristic flux responses in the high-energy tail (E3) of MEE precipitation.

3. Results

3.1. The General Flux Evolution

The average flux evolution presented in Figures 1 and 2 represents an overview of the data used in this study. The figures demonstrate the expected differences between the two energy channels of MEE precipitation. Both Figures 1 and 2 show that the E3 peak is typically about two orders of magnitude smaller than that of E1. From

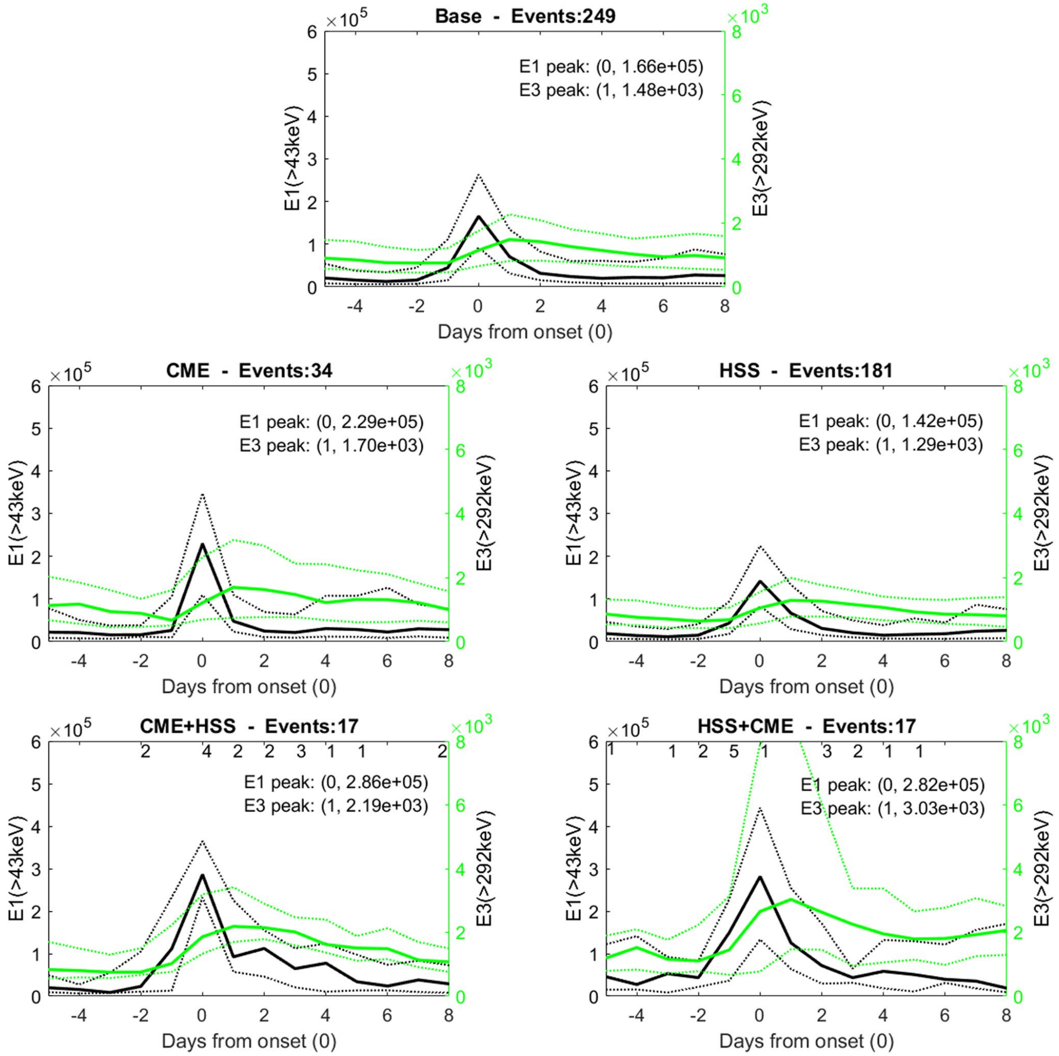

Figure 2. SEAs of the electron flux for the E1 (>43 keV) (black) and E3 (>292 keV) (green) energy channels during different solar wind structures given in $\text{cm}^{-2}\text{s}^{-1}\text{sr}^{-1}$. The *x*-axis indicates days from the onset defined as in Figure 1. The dotted lines show the lower and upper quartiles. The coordinates of the E1 and E3 peaks are presented in the upper right corner. The numbers at the top of the bottom two panels indicate the number of events with a structural solar wind change on a specific day. Note that the *y*-axis scaling of the black and green curves are different; the green *y*-axis is on the right-hand side. However, the *y*-axes are the same for all panels.

Figure 2, the average HSS has considerably lower flux responses than other structures. The two combined structures have higher E1 and E3 average peaks than single structures. HSS + CMEs show large variability in E3 as the upper and lower quartiles indicate extremely high and low flux responses, respectively. E3 typically has the highest flux responses within 1 day after the E1 peak. Also evident is the relatively steep rise and fall of E1 around the onset compared to the broader E3 response. The following results explore potential prediction capabilities for the E3 peak, the delay of the E3 peak relative to that of E1, and the duration of E3 enhancement in relation to solar wind properties.

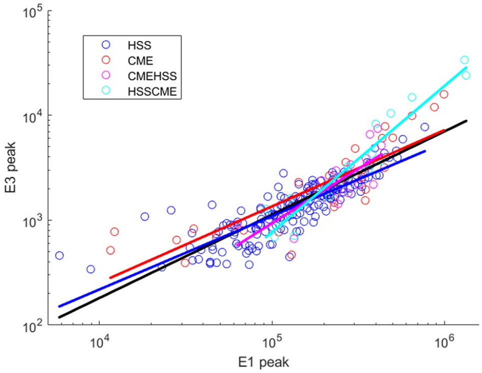

Structure	r	p-value	a	b
BASE	0.89	0	0.79	-2.10
CME	0.94	0	0.73	-1.15
HSS	0.91	0	0.70	-1.04
CME+HSS	0.74	0.0007	1.03	-5.07
HSS+CME	0.96	0	1.39	-9.39

Figure 3. Scatter plot of the dependence the E3 (>292 keV) peak has on the E1 (>43 keV) peak. The two fluxes are given in $\mathrm{cm}^{-2}\mathrm{s}^{-1}\mathrm{sr}^{-1}$. The regression lines for the different structures, including the base (black), are plotted on top. The fluxes are on a log-log scale. The correlation coefficients (r), the statistical significance values (p-value), and the line fitting parameters, a and b, for the different structures are shown in a table to the right.

3.2. The E3 (>292 keV) Peak Flux

Figure 3 shows a log-log scatter plot of how the E3 peak depends on the peak of E1. On the right is a table of the correlation coefficients (r), p-values, and line-fitting parameters a and b. Note that the peak fluxes refer to the maximum flux response within the solar wind structure period. The E3 peak scales consistently to that of the E1 peak with a correlation coefficient of 0.89 for all events (Base). Independently, the solar wind structures also have high correlation coefficients (>0.90), with the exception of CME + HSSs, which have a correlation coefficient of 0.74. CMEs and HSSs have similar rates of change (≈0.70), while the rate of change for the combined structures is higher (>1.00). The E3 peak during HSS + CMEs has a significantly stronger sensitivity to changes in the E1 peak with a rate of change equal to 1.39. For high E1 values ($>3 \times 10^5 \mathrm{cm}^{-2} s^{-1} sr^{-1}$), Figure 3 shows that the fit derived from the Base events would underestimate the strong HSS + CME response due, particularly, to the dominance of the weaker HSS response.

Figure 4 shows the same as Figure 3 just for how the E3 peak depends on different solar wind properties. From top to bottom, the solar wind properties are Bz, v, and ϵ. The properties are averaged over 4 days, from 2 days before to 1 day after onset. As in Figure 3, the correlation between the peak fluxes and the solar wind parameters is portrayed in a scatter plot with the corresponding linear regression lines for each structure. Note that the Bz and v plots are semi-log plots while ϵ is a log-log plot. To the right of each scatter plot is a table with the same content as in Figure 3.

When considering the Base presented in Figure 4, Bz (top panel) and v (middle panel) correlate poorly with the E3 peak as the correlation coefficients are −0.51 and 0.49, respectively. However, the correlation between the Base and ϵ (bottom panel) is high (0.84). ϵ has small p-values (<0.05) and the highest correlation coefficients (r) for the various solar wind structures. An exception is found for CMEs where the correlation coefficient between solar wind speed and E3 is higher (0.75). The relation between the ϵ coupling function and the E3 peak (bottom panel) shows that the rates of change for the different structures are fairly similar, and the lines are nearly superposed. In fact, CMEs and HSSs have the same rate of change (1.16).

The poor correlation between E3 and Bz (top panel in Figure 4) might be due to the negative and positive variations in Bz being averaged over 4 days, whereas it is the negative Bz periods that would most effectively impact E3.

3.3. The Delay of E3

To utilize the correlations presented in Figures 3 and 4, information on the difference in timing between the two peak fluxes is needed. Figure 5 shows the probability of a given delay in the E3 peak for the different structures.

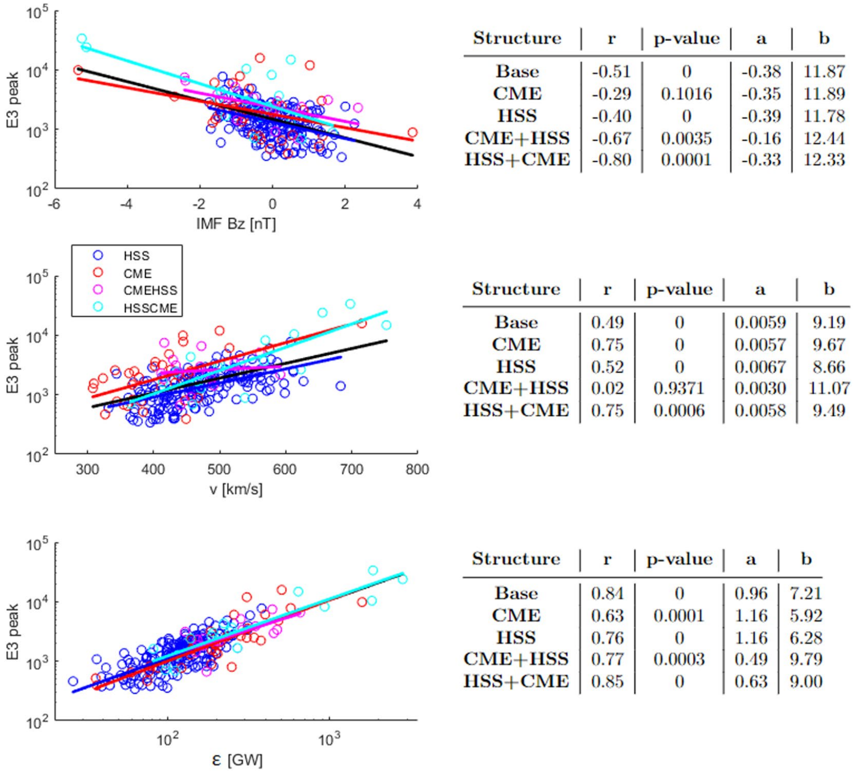

Structure	r	p-value	a	b
Base	-0.51	0	-0.38	11.87
CME	-0.29	0.1016	-0.35	11.89
HSS	-0.40	0	-0.39	11.78
CME+HSS	-0.67	0.0035	-0.16	12.44
HSS+CME	-0.80	0.0001	-0.33	12.33

Structure	r	p-value	a	b
Base	0.49	0	0.0059	9.19
CME	0.75	0	0.0057	9.67
HSS	0.52	0	0.0067	8.66
CME+HSS	0.02	0.9371	0.0030	11.07
HSS+CME	0.75	0.0006	0.0058	9.49

Structure	r	p-value	a	b
Base	0.84	0	0.96	7.21
CME	0.63	0.0001	1.16	5.92
HSS	0.76	0	1.16	6.28
CME+HSS	0.77	0.0003	0.49	9.79
HSS+CME	0.85	0	0.63	9.00

Figure 4. Scatter plots of the dependence the E3 (>292 keV) peak [$\mathrm{cm^{-2}s^{-1}sr^{-1}}$] has on the 4-day averaged IMF Bz (top), v (middle), and ϵ (bottom). The regression lines for the different structures, including the Base (black), are plotted on top. Bz and v are on a log-lin scale while ϵ is on a log-log scale. The correlation coefficients (r), the statistical significance values (p-value), and the line fitting parameters, a and b, for the different structures are shown in a table to the right of each plot.

A 0-day delay indicates that E3 peaks within the same day as E1, a 1-day delay that E3 peaks within the following day, and so on. The highest probability is for a 1-day delay of the E3 peak, independent of solar wind structure (see Figure 5). A high probability for a 1-day delay is expected based on the SEAs shown in Figures 1 and 2. However, the delay varies from zero to 3 days. CMEs have the highest probability (32%) for a 0-day delay and the lowest probability for a 3-day delay (9%). Both CME and HSS + CME events have a higher probability (32% and 29%, respectively) for a 0-day delay than a delay of more than 1 day.

All structures have >60% chance for a 1-day delay of the E3 peak. A higher resolution is needed to see differences within these days. Still, based on daily variability, this study targets parameters that influence the timing of the maximum response in E3 from 0 to 3 days.

Figure 6 shows the average Bz, v, ϵ, and E1 peak values for the different delays in the E3 peak for CMEs (red) and HSSs (blue). (The low statistics of the combined structures resulted in large errors and insignificant results, and are therefore not shown here.) In general, none of the parameters show a significant trend in influencing the delay of the E3 peak. Still, a weak tendency is evident in the solar wind speed, where slower speed might be associated with a longer delay.

Figure 7 shows the probabilities of different delays in the E3 peak with regard to solar wind speed. The x-axis indicates the speeds at which the 4-day average v exceeds. The y-axis for the two top panels shows the probability of the indicated delay with a solar wind speed above the given x-value, while the bottom panels show the number

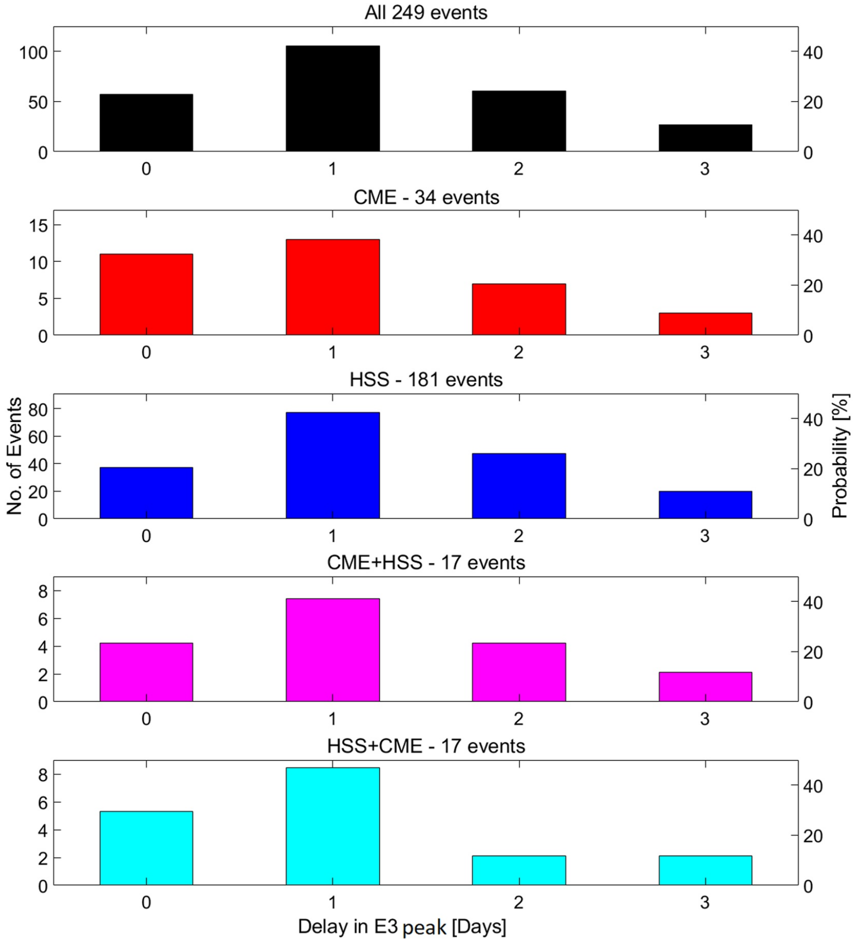

Figure 5. The delay in the E3 (>292 keV) peak relative to the E1 (>43 keV) peak associated with the different solar wind structures showed in days on the *x*-axis. The left *y*-axis shows the number of events with a certain E3 delay, and the right *y*-axis shows the probability of this delay.

of events with an average v above the given x-value. Only results for v are shown as Bz, ϵ, and E1 showed little influence on the delay when examined in the same manner as presented in Figure 7.

Figure 7 shows that there is a threshold in the solar wind speed at $v > 400$ km/s and $v > 550$ km/s for CMEs and HSSs, respectively, above which the probability of a 0-day delay increases substantially. For CMEs, this probability increases from 47% at $v > 400$ km/s to 75% at $v > 475$ km/s, while $v > 350$ km/s reduces the chance of a two- and 3-day delay to below 10%. For HSSs, a 1-day delay is dominant up until ~425 km/s, where the probability of a 0-day delay increases consistently and reaches the same probability (41%) of a 1-day delay at $v > 550$ km/s.

3.4. The Duration of the Precipitation Events

To evaluate the duration of the flux responses, the full width at the half-maximum value of the peak for both E1 and E3 was calculated. Twelve events were discarded as E1, E3, or both did not fall below this value within 8 days

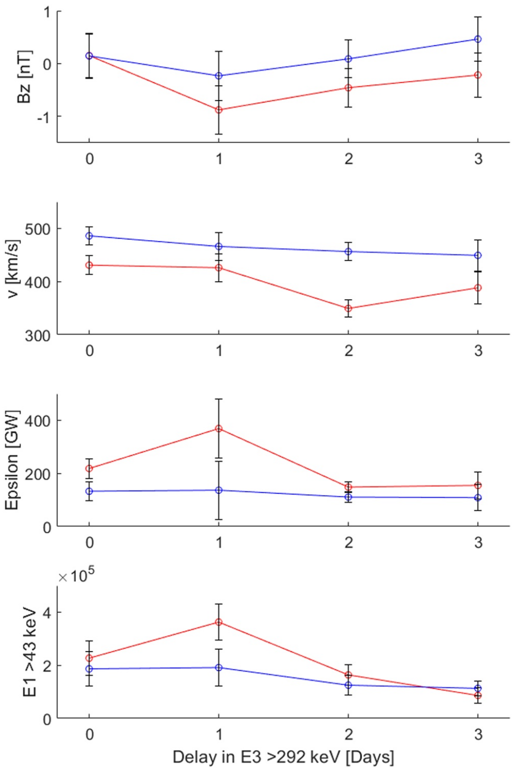

Figure 6. The average Bz, v, ϵ, and maximum E1 (>43 keV) [$\mathrm{cm^{-2}s^{-1}sr^{-1}}$] values associated with the delay of the E3 (>292 keV) peak for CMEs (red) and HSSs (blue). The error bars show the standard deviations of the average values.

from the onset due to new activity. This led to a loss of 17 HSSs and three HSS + CMEs. The duration of the E1 and E3 responses and their occurrence probability are presented in Figure 8.

Generally, when considering the Base (top), the E3 response lasts longer (>2 days) compared to the duration of the E1 response (<3 days). Figure 8 also shows that CMEs have the highest probability (62%) for an elevated E1 response of just 1 day, while for HSSs, CME + HSSs, and HSS + CMEs, a duration of 2 days is most common. The duration of the high-energy tail (E3) is most likely to last 4 days for both CMEs and HSSs, with a probability of 32% and 23%, respectively. Even though CMEs have a higher probability for a shorter E1 response, the highest probability of the E3 duration is still 4 days. In fact, 79% of CMEs have an E3 duration of 3 days or longer. The combined structures, though having low statistics, also indicate longer flux enhancements of the high-energy tail compared to E1.

No significant tendency was evident between the duration of E3 and Bz, v, or ϵ when examined in the same manner as delay in Figures 6 and 7.

4. Discussion

In this study, the high-energy tail of MEE precipitation has been compared to the E1 response and investigated in the context of solar wind drivers and the associated v, Bz, and ϵ parameters concerning the following features.

- The maximum flux response
- The delay in maximum flux response
- The duration of the flux response

An in-depth understanding of these three key parameters is necessary to represent the entire MEE precipitation spectrum realistically. Evaluating each parameter's potential in determining the probability of a specific response paves the way for understanding which variables can be applied to increase the accuracy of an MEE parameterization on both daily and decadal scales.

4.1. The Maximum Precipitating Fluxes

On average, HSSs have lower MEE flux responses than CMEs and combined structures (see Figure 2). Consistent with our results, Asikainen and Ruopsa (2016) showed that the average precipitating fluxes in 2004–2014 were higher for CMEs compared to HSSs for the E1 and E3 energy channels. The relatively low HSS flux response might be partly because the precipitating MEE flux is averaged over a wide latitude band from 55° to 75°N and the precipitation region associated with HSS typically does not expand as widely as CMEs (Babu et al., 2022). The upper quartile of the MEE flux for HSS + CMEs in Figure 2 demonstrates that these structures can trigger extreme MEE flux levels in both E1 and E3. Kilpua, Balogh, et al. (2017) and Kilpua, Koskinen, et al. (2017) also pointed out the potential of severe geomagnetic storms associated with the combination of solar wind structures. Moreover, Asikainen and Ruopsa (2016) found that the efficiency of both HSSs and CMEs in producing MEE precipitation peaks in the declining phase of the solar cycle, where these events often occur simultaneously or in close sequence.

HSSs are more frequent throughout a solar cycle than CMEs (Asikainen & Ruopsa, 2016) and, in this study, constitute 73% of the identified structures during the investigated 11 yr. As the average HSS has considerably weaker flux responses compared to CME-related events, an MEE parameterization based on "the average event" will underestimate the potentially strong impact associated with CME-related activity and exaggerate flux levels associated with the common HSSs. Hence, such a model will not be able to represent the variability associated with MEE precipitation for daily and decadal scales. Tyssøy et al. (2019) showed that van de Kamp et al. (2016)'s ApEEP model, which is scaled by the geomagnetic index Ap based on median flux responses, falls short in reproducing the flux levels and variability associated with strong geomagnetic storms. Additionally, Tyssøy

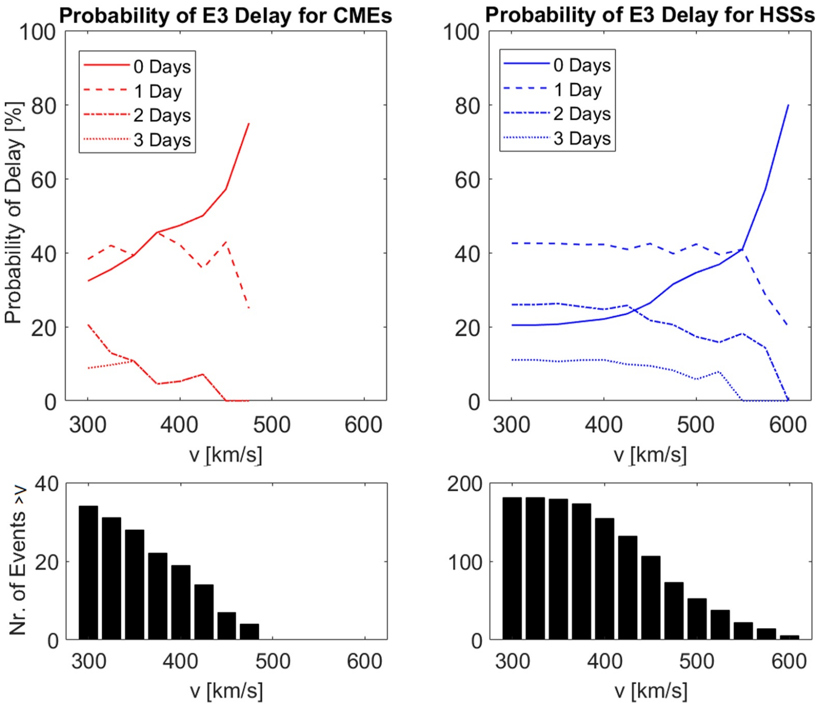

Figure 7. The solar wind speed-dependent probability of the delay in the E3 (>292 keV) peak for CMEs (red) and HSSs (blue). The *y*-axis of the two top panels shows the probability of the indicated delay dependent on events with average solar wind speeds that exceed the indicated *x*-axis value. The *y*-axis of the two bottom panels shows the number of events with average solar wind speeds which exceed the indicated *x*-value.

et al. (2021) compared eight different ionization rates, all based on MEPED observations, during an active period of March/April 2010, including a period of combined events. The comparison showed that the ApEEP-based model predicts significantly weaker ionization rates than other estimates, particularly when considering the high-energy tail. Hence, a more realistic representation of MEE precipitation might be achieved by considering the probability of flux response variations regarding solar wind structure.

Figure 3 implies that knowledge of the E1 peak will enable the prediction of the peak flux of the high-energy tail as the correlation coefficient for the Base events is 0.89. Independently, the solar wind structures all have a high correlation (>0.90), with the exception of CME + HSSs, which have a low correlation (0.74). The E3 peak during combined structures stands out as it has a stronger sensitivity to changes in E1. Particularly, HSS + CMEs stand out with a significantly higher rate of change of 1.39. As HSSs strongly dominate the average structure, a model based on the average relationship will systematically underestimate the high-energy tail of MEE precipitation during combined events when the E1 response is high ($>3 \times 10^5 \mathrm{cm}^{-2}\mathrm{s}^{-1}\mathrm{sr}^{-1}$).

Figure 4 reveals ϵ as a key parameter to determine the peak of E3, independent of solar wind structure. Ødegaard et al. (2017) reported a linear relationship between the energy input into the magnetosphere and precipitation of relativistic electrons by studying 41 weak and moderate geomagnetic storms driven by CIRs. Our study suggests, however, that this relationship is independent of the driving solar wind structure. This is not self-evident as multiple studies suggest that the energy partitioning within the magnetosphere might be different for different solar wind structures (N. E. Turner et al., 2009).

Note that to utilize the dependency between either the E1 and E3 peaks or the E3 peak and the ϵ parameter in a model, the timing of the flux peaks needs to be known. The timing of the E1 peak corresponds well with the

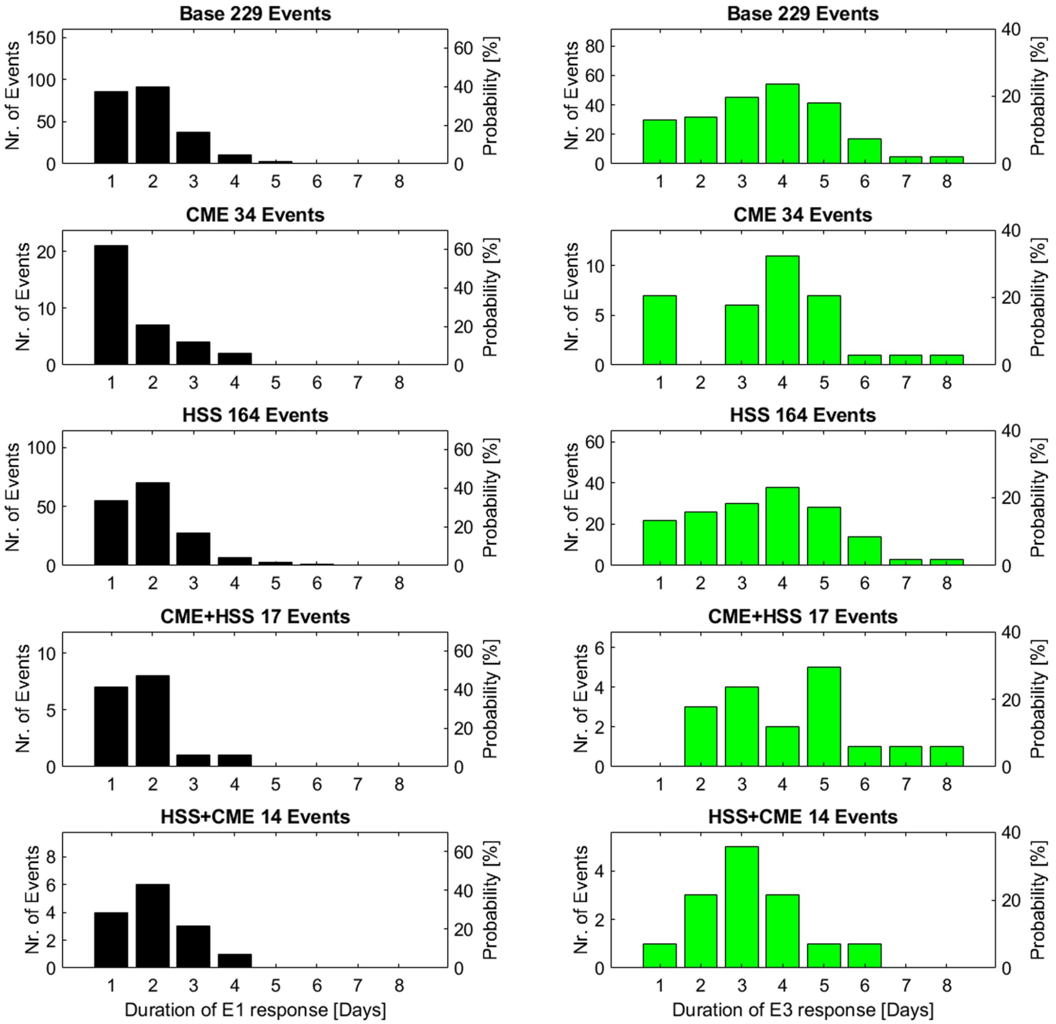

Figure 8. Probability of the duration [days] of E1 (>43 keV) and E3 (>292 keV) for the four different solar wind structures. E1 is presented in black to the left, and E3 in green to the right. From top to bottom, the solar wind structures are Base, CME, HSS, CME + HSS, and HSS + CME.

indices Bz, v, and ϵ (see Figure 1). Previous studies have also shown that the E1 peak and timing are fairly well correlated with geomagnetic activity (Tyssøy, Partamies, Babu, Smith-Johnsen, & Salice, 2021; van de Kamp et al., 2016). However, the timing of the E3 peak differs from that of E1.

4.2. Delay

Figure 5 shows that the E3 peak has the highest probability of occurring 1 day after onset. Evidence of delayed electron flux responses with increasing electron energy has also been documented in other studies (Li et al., 2005; Longden et al., 2008; Ødegaard et al., 2017; Tyssøy, Partamies, Babu, Smith-Johnsen, & Salice, 2021). Li et al. (2005) found solar wind speed to be a dominant controlling parameter for electron energies from 50 keV to 6 MeV. They identified an energy-dependent time shift of approximately 1 day between 50–75 and 225–300 keV, consistent with our findings. A similar time shift for the MEE high-energy tail was also found by Longden et al. (2008) and Ødegaard et al. (2017). Moreover, Tyssøy, Partamies, Babu, Smith-Johnsen, and Salice (2021) investigated the predictability of the AE index for MEE precipitation. They demonstrated how high predictability could be achieved when accounting for the delayed response of the high-energy tail ($\gtrsim$300 keV) by accumulating the geomagnetic activity over time, taking into account the electron flux lifetimes.

The presence of a time delay is consistent with the view of electrons in the radiation belts being accelerated to progressively higher energies over time (Horne et al., 2005). Both Horne et al. (2005) and Rodger et al. (2010) observed the delay in trapped electron particle energies and found an energy-dependent time delay.

This study finds a spread of 0–3 days in the delay of the E3 peak. CMEs have higher probabilities for a fast response than the other solar wind structures as the high-energy tail peaks within a day for 71% of the events. In contrast, HSSs are more likely to have a 2-day delayed E3 peak than a 0-day delay. The varying time delay makes it difficult to produce a representative MEE precipitation climatology. Information about solar wind speed increases the prediction capabilities for both CMEs and HSSs. However, different speed thresholds need to be applied for the different structures to determine the probability of delay (see Figure 7).

The lower energies in the MEE fluxes are often associated directly with substorm injection. However, the high-energy tail (E3) needs additional energizing (Li et al., 2005; Tyssøy, Partamies, Babu, Smith-Johnsen, & Salice, 2021). Therefore, the physical mechanisms that link solar wind velocity to MEE precipitation are likely to be two-fold. Larger solar wind velocities can produce more intense ULF waves within the magnetosphere (Engebretson et al., 1998), providing radial diffusion and energizing the lower energy electrons (Barker et al., 2005; Schulz & Lanzerotti, 1974). Simultaneously, high solar wind speed is a good predictor of the substorm onset probability (Newell et al., 2016). Substorms will fuel VLF chorus waves, and the injected seed particles can be energized as they drift across the substorm-induced electric field on the night side.

Miyoshi et al. (2013) highlighted the importance of the southward (negative) IMF Bz component in accelerating the high-energy tail of the radiation belt population. Miyoshi et al. (2013) showed that HSS dominated by a southward IMF are associated with large flux enhancements of relativistic electrons. However, the role of Bz in our analysis is less evident due to the daily resolution wherein the average Bz is near zero, as it is likely to have both positive and negative values throughout the day. Nonetheless, as ϵ emphasizes negative Bz values, it will better represent the geoeffectiveness throughout a day which might be relevant in terms of peak flux levels and delay.

The timing of the E3 peaks is a product of both the acceleration processes and the lifetime of the respective electron enhancement. A short delay of zero or 1 day is typically linked to both high E1 values and high solar wind velocity based on Figure 6. This implies that an efficient acceleration process needs to be accompanied by an efficient loss process.

The lifetimes of MEE in the radiation belts depend on the energy, radial distance from Earth, and the level of geomagnetic activity. The lifetimes for 100 keV electrons at a radial distance of about four earth radii from the center of the Earth are approximately 3.6 days and 13 hr for quiet and active geomagnetic conditions, respectively (Orlova et al., 2016). Hence, a short lifetime is likely to follow the strength of the coupling functions, ϵ, which is closely linked to geomagnetic activity (Newell et al., 2016). This link is consistent with the average ϵ values for HSSs in Figure 6, whereas the average ϵ values for CMEs are a bit more ambiguous. The expected lifetime can, however, also be rapidly reduced in the case of magnetopause shadowing, where trapped particles over several radial distances are lost to the magnetopause. Magnetopause shadowing is a consequence of a sudden dynamic pressure increase in the solar wind, alongside convection-driven outward radial transport (D. L. Turner et al., 2012), both commonly associated with CME events.

4.3. Duration

Similar to the flux peaks, the duration of the MEE precipitation events will depend on a combination of the acceleration and loss mechanisms. Figure 8 shows longer flux enhancements of the high-energy tail compared to E1. CMEs have a higher probability for a short E1 duration (62% chance of lasting 1 day) compared to the other structures, which are more likely to be associated with durations of 2 days. Similarly, Longden et al. (2008) found that the mean electron flux intensity for 50–500 keV electrons during geomagnetic storms driven by CMEs typically return to pre-storm levels after 1–2 days from zero epoch (the first minimum in Dst), while CIR-driven storms do not return to pre-storm values within their 3-day analysis after zero epoch. In our study, all structures, including CMEs, showed that the high-energy tail of the MEE precipitation had the highest probability of lasting 3–5 days, indicating the possibility of strong, long-lasting precipitation of E3 electrons in all structures, including CMEs. The shorter E1 duration associated with CMEs does not appear to suggest a shorter E3 duration. Note that the conclusion about the duration of the flux responses during CMEs is based on a few events but still seems to have a solid trend.

When examining the different solar wind parameters, it was concluded that they have no significant correlation with the duration of the flux responses and were, therefore, not included in this study. Tyssøy, Partamies, Babu, Smith-Johnsen, & Salice (2021) found the >292 keV precipitation fluxes to correlate well with the accumulated geomagnetic activity, assuming a lifetime of 9 days. Hence, the flux response and its duration are likely to be an accumulated effect of the preceding geomagnetic activity. This feature cannot be accounted for in the present analysis focusing on isolated events.

Moreover, Tyssøy et al. (2019) discussed the implication of underestimating the duration of the MEE precipitation events. It is, therefore, essential that an MEE precipitation parameterization applied in chemistry-climate models reflects the variability found in Figure 8.

5. Conclusion

Motivated by the demand to create a MEE parameterization that goes beyond the average picture, this study targets three key aspects needed to understand the high-energy tail of MEE precipitation: peak flux, delay, and duration. MEE precipitation is explored in the context of its solar wind drivers and the associated solar wind properties. The BLC measurements of the E1 (>43 keV) and E3 (>292 keV) MEE fluxes based on the MEPED detectors for the years 2004–2014 (one solar cycle) at 55°–75° CGM latitude are used. These energy channels reflect the general behavior of MEE and its high-energy tail. The key aspects are evaluated concerning the probability of a specific response.

The high occurrence frequency of HSSs compared to CMEs implies that they will strongly dominate the average event throughout a solar cycle in terms of flux strength, the delay of the high-energy tail, and the duration. In this study, HSSs constitute 73% of all 249 events selected in the 11 yr and are found to have lower flux responses than CME and combined events. Hence, the average event will best represent HSSs and underestimate stronger precipitation events.

There is a strong link between the peak fluxes in E1 and E3, with a correlation of 0.89. Information on the delay is needed to utilize their temporal relationship in a model. Moreover, higher correlations can be achieved when considering the respective solar wind driver. ϵ is a good parameter to use if the solar wind structure is unknown as the relation between ϵ and the E3 peak is the same for CMEs and HSSs.

E3 peaks 0–3 days after E1 peaks. The highest probability of ~42% occurs for a 1-day delay, independent of solar wind structure. CMEs and HSS + CMEs have higher probabilities for faster E3 responses (>70% for a zero-one-day delay) compared to the other structures. Considering solar wind speed will increase the capability of predicting the delay for both CMEs and HSSs. Different speed thresholds for the different structures need to be applied.

All structures are associated with longer flux enhancements of the high-energy tail compared to E1. The duration of the E1 response has the highest probability of lasting 1 day for CMEs, whereas there is a higher probability of durations of 2 days for other structures. Nevertheless, the duration of the E3 response has the highest probability of lasting 4 days for both CMEs and HSSs. None of the applied solar wind parameters correlated with the duration of the MEE events.

A future MEE precipitation parameterization should represent the variability on both daily and decadal scales more realistically, allowing a better description of the subsequent atmospheric and chemical impact. This could be achieved by implementing a stochastic MEE parameterization accounting for the range of possible flux responses, delay, and duration. This is particularly important to understand the impact of the high-energy tail of the MEE spectrum.

Data Availability Statement

The NOAA/POES MEPED data used in this study are available from the National Oceanic and Atmospheric Administration (https://www.ngdc.noaa.gov/stp/satellite/poes/dataaccess.html). The bounce loss cone fluxes used in this study are available at Zenodo via https://doi.org/10.5281/zenodo.6590387. Geomagnetic indices and solar wind parameters were obtained from NASA Omniweb at https://omniweb.gsfc.nasa.gov/form/dx1.html.

The authors gratefully acknowledge the SuperMAG collaborators (https://supermag.jhuapl.edu/info/?page=acknowledgement) where the epsilon (ϵ) parameter was downloaded.

Acknowledgments
The study is supported by the Norwegian Research Council (NRC) under contracts 223252 and 302040. HNT further acknowledges the Young CAS (Centre for Advanced Studies) fellow program. The authors thank the Space Weather Prediction Center (SWPC), NOAA for providing the MEPED data. IGR acknowledges support from the ACE mission.

References

Akasofu, S. I. (1981). Energy coupling between the solar wind and the magnetosphere. *Space Science Reviews*, *28*(2). https://doi.org/10.1007/BF00218810

Asikainen, T., & Ruopsa, M. (2016). Solar wind drivers of energetic electron precipitation. *Journal of Geophysical Research: Space Physics*, *121*(3), 2209–2225. https://doi.org/10.1002/2015JA022215

Babu, E. M., Tyssøy, H. N., Smith-Johnsen, C., Maliniemi, V., Salice, J. A., Millan, R. M., & Richardson, I. G. (2022). Determining latitudinal extent of energetic electron precipitation using MEPED on-board NOAA/POES. *Journal of Geophysical Research: Space Physics*, *127*(9). https://doi.org/10.1029/2022JA030489

Baldwin, M. P., & Dunkerton, T. J. (2001). Stratospheric harbingers of anomalous weather regimes. *Science*, *294*(5542), 581–584. https://doi.org/10.1126/science.1063315

Barker, A. B., Li, X., & Selesnick, R. S. (2005). Modeling the radiation belt electrons with radial diffusion driven by the solar wind. *Space Weather*, *3*(10). https://doi.org/10.1029/2004SW000118

Beharrell, M. J., Honary, F., Rodger, C. J., & Clilverd, M. A. (2015). Substorm-induced energetic electron precipitation: Morphology and prediction. *Journal of Geophysical Research: Space Physics*, *120*(4), 2993–3008. https://doi.org/10.1002/2014JA020632

Borovsky, J. E., & Denton, M. H. (2006). Differences between CME-driven storms and CIR-driven. *Journal of Geophysical Research: Space Physics*, *111*(A7), A07S08. https://doi.org/10.1029/2005JA011447

Damiani, A., Funke, B., López-Puertas, M., Santee, M. L., Cordero, R. R., & Watanabe, S. (2016). Energetic particle precipitation: A major driver of the ozone budget in the Antarctic upper stratosphere. *Geophysical Research Letters*, *43*(7), 3554–3562. https://doi.org/10.1002/2016GL068279

Duderstadt, K. A., Huang, C.-L., Spence, H. E., Smith, S., Blake, J. B., Crew, A. B., et al. (2021). Estimating the impacts of radiation belt electrons on atmospheric chemistry using FIREBIRD II and Van Allen Probes observations. *Journal of Geophysical Research: Atmospheres*, *126*(7). https://doi.org/10.1029/2020JD033098

Engebretson, M., Glassmeier, K.-H., Stellmacher, M., Hughes, W. J., & Lühr, H. (1998). The dependence of high-latitude PcS wave power on solar wind velocity and on the phase of high-speed solar wind streams. *Journal of Geophysical Research: Space Physics*, *103*(A11), 26271–26283. https://doi.org/10.1029/97JA03143

Evans, D. S., & Greer, M. S. (2004). Polar orbiting environmental satellite space environment monitor - 2: Instrument descriptions and archive data documentation. NOAA Technical Memorandum version 1.4.

Funke, B., Baumgaertner, A., Calisto, M., Egorova, T., Jackman, C. H., Kieser, J., et al. (2011). Composition changes after the “Halloween” solar proton event: The High Energy Particle Precipitation in the Atmosphere (HEPPA) model versus MIPAS data intercomparison study. *Atmospheric Chemistry and Physics*, *11*(17), 9089–9139. https://doi.org/10.5194/acp-11-9089-2011

Gjerloev, J. W. (2012). The SuperMAG data processing technique. *Journal of Geophysical Research*, *117*(A9). https://doi.org/10.1029/2012JA017683

Hendrickx, K., Megner, L., Gumbel, J., Siskind, D. E., Orsolini, Y. J., Tyssøy, H. N., & Hervig, M. (2015). Observation of 27 days solar cycles in the production and mesospheric descent of EPP-produced NO. *Journal of Geophysical Research: Atmospheres*, *120*(10), 8978–8988. https://doi.org/10.1002/2015JA021441

Horne, R. B., Thorne, R. M., Glauert, S. A., Albert, J. M., Meredith, N. P., & Anderson, R. R. (2005). Timescale for radiation belt electron acceleration by whistler mode chorus waves. *Journal of Geophysical Research*, *110*(A3), A03225. https://doi.org/10.1029/2004JA010811

Jackman, C. H., DeLand, M. T., Labow, G. J., Fleming, E. L., Weisenstein, D. K., Ko, M. K. W., & Russell, J. M. (2005). Neutral atmospheric influences of the solar proton events in October–November 2003. *Journal of Geophysical Research*, *110*(A9). https://doi.org/10.1029/2004ja010888

Kataoka, R., & Miyoshi, Y. (2006). Flux enhancement of radiation belt electrons during geomagnetic storms driven by coronal mass ejections and corotating interaction regions. *Space Weather*, *4*(9). https://doi.org/10.1029/2005SW000211

Kennel, C. F., & Petschek, H. E. (1966). Limit on stably trapped particle fluxes. *Geophysical Research*, *71*, 1–28. https://doi.org/10.1029/JZ071i001p00001

Kidston, J., Scaife, A. A., Hardiman, S. C., Mitchell, D. M., Butchart, N., Baldwin, M. P., & Gray, L. J. (2015). Stratospheric influence on tropospheric jet streams, storm tracks, and surface weather. *Nature Geoscience*, *8*(6), 433–440. https://doi.org/10.1038/ngeo2424

Kilpua, E. K. J., Balogh, A., von Steiger, R., & Liu, Y. D. (2017). Geoeffective properties of solar transients and stream interaction regions. *Space Science Reviews*, *212*(3–4), 1271–1314. https://doi.org/10.1007/s11214-017-0411-3

Kilpua, E. K. J., Koskinen, H. E. J., & Pulkkinen, T. I. (2017). Coronal mass ejections and their sheath regions in interplanetary space. *Living Reviews in Solar Physics*, *14*(1), 5. https://doi.org/10.1007/s41116-017-0009-6

Koskinen, H. E. J., & Tanskanen, E. I. (2002). Magnetospheric energy budget and the epsilon parameter. *Journal of Geophysical Research: Space Physics*, *107*(A11), 1415. https://doi.org/10.1029/2002JA009283

Li, X., Baker, D. N., Temerin, M., Reeves, G., Friedel, R., & Shen, C. (2005). Energetic electrons, 50 keV to 6 MeV, at geosynchronous orbit: Their responses to solar wind variations. *Space Weather*, *3*(4). https://doi.org/10.1029/2004SW000105

Longden, N., Denton, M. H., & Honary, F. (2008). Particle precipitation during ICME-driven and CIR-driven geomagnetic storms. *Journal of Geophysical Research*, *113*(A6). https://doi.org/10.1029/2007JA012752

Maliniemi, V., Asikainen, T., & Mursula, K. (2016). Effect of geomagnetic activity on the northern annular mode: QBO dependence and the Holton-Tan relationship. *Journal of Geophysical Research: Atmospheres*, *121*(17), 10043–10055. https://doi.org/10.1002/2015JD024460

Maliniemi, V., Nesse Tyssøy, H., Smith-Johnsen, C., Arsenovic, P., & Marsh, D. R. (2021). Effects of enhanced downwelling of NO_x on Antarctic upper-stratospheric ozone in the 21st century. *Atmospheric Chemistry and Physics*, *21*(14), 11041–11052. https://doi.org/10.5194/acp-21-11041-2021

Marsh, D., Solomon, S., & Reynolds, A. (2004). Empirical model of nitric oxide in the lower thermosphere. *Journal of Geophysical Research*, *109*(A7), A07301. https://doi.org/10.1029/2003ja010199

Matthes, K., Funke, B., Andersson, M. E., Barnard, L., Beer, J., Charbonneau, P., et al. (2017). Solar forcing for CMIP6. *Geoscientific Model Development*, *10*(6), 2247–2302. https://doi.org/10.5194/gmd-10-2247-2017

Millan, R. M., & Thorne, R. M. (2007). Review of radiation belt relativistic electron losses. *Journal of Atmospheric and Solar-Terrestrial Physics*, *69*(3), 362–377. https://doi.org/10.1016/j.jastp.2006.06.019

Mironova, I. A., Artamonov, A. A., Bazilevskaya, G. A., Rozanov, E. V., Kovaltsov, G. A., Makhmutov, V. S., et al. (2019). Ionization of the polar atmosphere by energetic electron precipitation retrieved from balloon measurements. *Geophysical Research Letters*, *46*(2), 990–996. https://doi.org/10.1029/2018GL079421

Miyoshi, Y., Kataoka, R., Kasahara, Y., Kumamoto, A., Nagai, T., & Thomsen, M. F. (2013). High-speed solar wind with southward interplanetary magnetic field causes relativistic electron flux enhancement of the outer radiation belt via enhanced condition of whistler waves. *Geophysical Research Letters*, *40*(17), 4520–4525. https://doi.org/10.1002/grl.50916

Newell, P., Liou, K., Gjerloev, J., Sotirelis, T., Wing, S., & Mitchell, E. (2016). Substorm probabilities are best predicted from solar wind speed. *Journal of Atmospheric and Solar-Terrestrial Physics*, *146*, 28–37. https://doi.org/10.1016/j.jastp.2016.04.019

Ødegaard, L.-K. G., Tyssøy, H. N., Søraas, F., Stadsnes, J., & Sandanger, M. I. (2017). Energetic electron precipitation in weak to moderate corotating interaction region driven storms. *Journal of Geophysical Research: Space Physics*, *122*(3), 2900–2921. https://doi.org/10.1002/2016JA023096

Orlova, K., Shprits, Y., & Spasojevic, M. (2016). New global loss model of energetic and relativistic electrons based on Van Allen Probes measurements. *Journal of Geophysical Research: Space Physics*, *121*(2), 1308–1314. https://doi.org/10.1002/2015JA021878

Østgaard, N., Vondrak, R. R., Gjerloev, J. W., & Germany, G. (2002). A relation between the energy deposition by electron precipitation and geomagnetic indices during substorms. *Journal of Geophysical Research*, *107*(A9), 1246. https://doi.org/10.1029/2001JA002003

Partamies, N., Tesema, F., Bland, E., Heino, E., Nesse Tyssøy, H., & Kallelid, E. (2021). Electron precipitation characteristics during isolated, compound, and multi-night substorm events. *Annales Geophysicae*, *39*(1), 69–83. https://doi.org/10.5194/angeo-39-69-2021

Pettit, J., Randall, C., Peck, E., Marsh, D., van de Kamp, M., Fang, X., et al. (2019). Atmospheric effects of >30 keV energetic electron precipitation in the Southern Hemisphere winter during 2003. *Journal of Geophysical Research: Space Physics*, *124*(10), 8138–8153. https://doi.org/10.1029/2019JA026868

Richardson, I. G. (2018). Solar wind stream interaction regions throughout the heliosphere. *Living Reviews in Solar Physics*, *15*(1), 1. https://doi.org/10.1007/s41116-017-0011-z

Richardson, I. G., & Cane, H. V. (2012). Near-Earth solar wind flows and related geomagnetic activity during more than four solar cycles (1963–2011). *Journal of Space Weather and Space Climate*, *2*, A02. https://doi.org/10.1051/swsc/2012003

Rodger, C., Clilverd, M. A., Green, J. C., & Lam, M. M. (2010). Use of POES SEM-2 observations to examine radiation belt dynamics and energetic electron precipitation into the atmosphere. *Journal of Geophysical Research*, *115*(A4). https://doi.org/10.1029/2008JA014023

Schulz, M., & Lanzerotti, L. J. (1974). *Particle diffusion in the radiation belts*. Springer.

Seppälä, A., Randall, C. E., Clilverd, M. A., Rozanov, E., & Rodger, C. J. (2016). Geomagnetic activity and polar surface air temperature variability. *Journal of Geophysical Research*, *114*(A10). https://doi.org/10.1029/2008JA014029

Sinnhuber, M., Kazeminejad, S., & Wissing, J. M. (2011). Interannual variation of NO$_x$ from the lower thermosphere to the upper stratosphere in the years 1991–2005. *Journal of Geophysical Research*, *116*(A2). https://doi.org/10.1029/2010ja015825

Sinnhuber, M., Nesse Tyssøy, H., Asikainen, T., Bender, S., Funke, B., Hendrickx, K., et al. (2022). Heppa III intercomparison experiment on electron precipitation impacts: 2. Model-measurement intercomparison of nitric oxide (NO) during a geomagnetic storm in April 2010. *Journal of Geophysical Research: Space Physics*, *127*(1). https://doi.org/10.1029/2021JA029466

Smith-Johnsen, C., Tyssøy, H. N., Hendrickx, K., Orsolini, Y., Kumar, G. K., Ødegaard, L.-K. G., et al. (2017). Direct and indirect electron precipitation effect on nitric oxide in the polar middle atmosphere, using a full-range energy spectrum. *Journal of Geophysical Research: Space Physics*, *122*(8), 8679–8693. https://doi.org/10.1002/2017JA024364

Solomon, S., Crutzen, P. J., & Roble, R. G. (1982). Photochemical coupling between the thermosphere and the lower atmosphere: 1. Odd nitrogen from 50 to 120 km. *Journal of Geophysical Research*, *87*(C9), 7206–7220. https://doi.org/10.1029/JC087iC09p07206

Theodoridis, G. C., & Paolini, F. R. (1967). Pitch angle diffusion of relativistic outer belt electrons. *Annales Geophysicae*, *23*, 375–381.

Turner, D. L., Shprits, Y., Hartinger, M., & Angelopoulos, V. (2012). Explaining sudden losses of outer radiation belt electrons during geomagnetic storms. *Nature Physics*, *8*(3), 208–212. https://doi.org/10.1038/nphys2185

Turner, N. E., Cramer, W. D., Earles, S. K., & Emery, A. B. (2009). Geoefficiency and energy partitioning in CIR-driven and CME-driven storms. *Journal of Atmospheric and Solar-Terrestrial Physics*, *71*(10–11), 1023–1031. https://doi.org/10.1016/j.jastp.2009.02.005

Turunen, E., Verronen, P. T., Seppälä, A., Rodger, C. J., Clilverd, M. A., Tamminen, J., et al. (2009). Impact of different energies of precipitating particles on NO$_x$ generation in the middle and upper atmosphere during geomagnetic storms. *Journal of Atmospheric and Solar-Terrestrial Physics*, *71*(10–11), 1176–1189. https://doi.org/10.1016/j.jastp.2008.07.005

Tyssøy, H. N., Haderlein, A., Sandanger, M. I., & Stadsnes, J. (2019). Intercomparison of the POES/MEPED loss cone electron fluxes with the CMIP6 parametrization. *Journal of Geophysical Research: Space Physics*, *124*(1), 628–642. https://doi.org/10.1029/2018JA025745

Tyssøy, H. N., Partamies, N., Babu, E. M., Smith-Johnsen, C., & Salice, J. A. (2021). The predictive capabilities of the auroral electrojet index for medium energy electron precipitation. *Frontiers in Astronomy and Space Sciences*, *8*. https://doi.org/10.3389/fspas.2021.714146

Tyssøy, H. N., Sandanger, M. I., Ødegaard, L. G., Stadsnes, J., Aasnes, A., & Zawedde, A. E. (2016). Energetic electron precipitation into the middle atmosphere—Constructing the loss cone fluxes from MEPED POES. *Journal of Geophysical Research: Space Physics*, *121*(6), 5693–5707. https://doi.org/10.1002/2016JA022752

Tyssøy, H. N., Sinnhuber, M., Asikainen, T., Bender, S., Clilverd, M. A., Funke, B., et al. (2021). HEPPA III intercomparison experiment on electron precipitation impacts: 1. Estimated ionization rates during a geomagnetic active period in April 2010. *Journal of Geophysical Research: Space Physics*, *127*. https://doi.org/10.1029/2021JA029128

Tyssøy, H. N., & Stadsnes, J. (2015). Cutoff latitude variation during solar proton events: Causes and consequences. *Journal of Geophysical Research: Space Physics*, *120*(1), 553–563. https://doi.org/10.1002/2014JA020508

Tyssøy, H. N., Stadsnes, J., Søraas, F., & Sørbø, M. (2013). Variations in cutoff latitude during the January 2012 solar proton event and implication for the distribution of particle energy deposition. *Geophysical Research Letters*, *40*(16), 4149–4153. https://doi.org/10.1002/grl.50815

van de Kamp, M., Rodger, C. J., Seppälä, A., Clilverd, M. A., & Verronen, P. T. (2018). An updated model providing long-term data sets of energetic electron precipitation, including zonal dependence. *Journal of Geophysical Research: Atmospheres*, *123*(17), 9891–9915. https://doi.org/10.1029/2017JD028253

van de Kamp, M., Seppälä, A., Clilverd, M. A., Rodger, C. J., Verronen, P. T., & Whittaker, I. C. (2016). A model providing long-term data sets of energetic electron precipitation during geomagnetic storms. *Journal of Geophysical Research: Atmospheres*, *121*(20), 12520–12540. https://doi.org/10.1002/2015JD024212

Verronen, P. T., & Lehmann, R. (2013). Analysis and parameterization of ionic reactions affecting middle atmospheric HO$_x$ and NO$_y$ during solar proton events. *Annales Geophysicae*, *31*(5), 909–956. https://doi.org/10.5194/angeo-31-909-2013

Verronen, P. T., Seppälä, A., Kyrölä, E., Tamminen, J., Pickett, H. M., & Turunen, E. (2006). Production of odd hydrogen in the mesosphere during the January 2005 solar proton event. *Geophysical Research Letters*, *33*(24), L24811. https://doi.org/10.1029/2006GL028115

(WCRP), W. C. R. P. (2011). WCRP Coupled Model Intercomparison Project (CMIP). Retrieved from https://www.wcrp-climate.org/wgcm-cmip

Yando, K., Millan, R. M., Green, J. C., & Evans, D. S. (2011). A Monte Carlo simulation of the NOAA POES medium energy proton and electron detector instrument. *Journal of Geophysical Research: Space Physics*, *116*(A10). https://doi.org/10.1029/2011JA016671

Zawedde, A. E., Tyssøy, H. N., Stadsnes, J., & Sandanger, M. I. (2018). The impact of energetic particle precipitation on mesospheric OH—Variability of the sources and the background atmosphere. *Journal of Geophysical Research: Space Physics*, *123*(7), 5764–5789. https://doi.org/10.1029/2017JA025038

Zhang, J., Richardson, I. G., Webb, D. F., Gopalswamy, N., Huttunen, E., Kasper, J. C., et al. (2007). Solar and interplanetary sources of major geomagnetic storms (Dst ≤ −100 nT) during 1996–2005. *Journal of Geophysical Research*, *112*(A10). https://doi.org/10.1029/2007JA012321

Zhang, Y., & Paxton, L. (2008). An empirical *Kp*-dependent global auroral model based on TIMED/GUVI FUV data. *Journal of Atmospheric and Solar-Terrestrial Physics*, *70*(8–9), 1231–1242. https://doi.org/10.1016/j.jastp.2008.03.008

Zurbuchen, T. H., & Richardson, I. G. (2006). In-situ solar wind and magnetic field signatures of interplanetary coronal mass ejections. *Space Science Reviews*, *123*(1–3), 31–43. https://doi.org/10.1007/s11214-006-9010-4

Paper II

The High-Energy Tail of Energetic Electron Precipitation: Solar Wind Drivers and Geomagnetic Responses

J. Salice, H. Nesse, N. Partamies, E. Kilpua, A. Kavanagh, M. Decotte, E. Babu, and C. Smith-Johnsen

Front. Astron. Space Sci., **11** (2024). doi: 10.3389/fspas.2024.1352020

frontiers | Frontiers in Astronomy and Space Sciences

TYPE Original Research
PUBLISHED 07 March 2024
DOI 10.3389/fspas.2024.1352020

The high-energy tail of energetic electron precipitation: solar wind drivers and geomagnetic responses

Josephine Salice[1]*, Hilde Nesse[1], Noora Partamies[2], Emilia Kilpua[3], Andrew Kavanagh[4], Margot Decotte[1], Eldho Babu[1] and Christine Smith-Johnsen[1]

[1]Department for Physics and Technology, University of Bergen, Bergen, Norway, [2]Department of Artic Geophysics, The University Centre in Svalbard, Longyearbyen, Norway, [3]Department of Physics, University of Helsinki, Helsinki, Finland, [4]Space Weather and Atmosphere, British Antarctic Survey, Cambridge, United Kingdom

Check for updates

OPEN ACCESS

EDITED BY
Dogacan Ozturk,
University of Alaska Fairbanks, United States

REVIEWED BY
Luisa Capannolo,
Boston University, United States
Aaron Breneman,
National Aeronautics and Space Administration, United States
Yangyang Shen,
University of California, Los Angeles, United States

*CORRESPONDENCE
Josephine Salice,
✉ josephine.salice@uib.no

RECEIVED 07 December 2023
ACCEPTED 13 February 2024
PUBLISHED 07 March 2024

CITATION
Salice J, Nesse H, Partamies N, Kilpua E, Kavanagh A, Decotte M, Babu E and Smith-Johnsen C (2024), The high-energy tail of energetic electron precipitation: solar wind drivers and geomagnetic responses. *Front. Astron. Space Sci.* 11:1352020. doi: 10.3389/fspas.2024.1352020

Compositional NOx changes caused by energetic electron precipitation (EEP) at a specific altitude and those co-dependent on vertical transport are referred to as the EEP direct and indirect effect, respectively. The direct effect of EEP at lower mesospheric and upper stratospheric altitudes is linked to the high-energy tail of EEP ($\gtrsim$ 300 keV). The relative importance of this direct effect on NOx, ozone, and atmospheric dynamics remains unresolved due to inadequate particle measurements and scarcity of polar mesospheric NOx observations. An accurate parameterization of the high-energy tail of EEP is, therefore, crucial. This study utilizes EEP flux data from MEPED aboard the POES/Metop satellites from 2004–2014. Data from both hemispheres (55–70° N/S) are combined in daily flux estimates. 164 peaks above the 90th percentile of the $\gtrsim$ 30 keV flux are identified. These peaks are categorized into absolute E1 and E3 events representing weak and strong $\gtrsim$ 300 keV responses, respectively. A subset of absolute E1 and E3 events with similar $\gtrsim$ 30 keV responses is termed overlapping events. Additionally, relative E1 and E3 events are determined by the relative strength of the $\gtrsim$ 300 keV response, scaled by the initial $\gtrsim$ 30 keV flux. A comparison between E1 and E3 events aims to identify solar wind and geomagnetic conditions leading to high-energy EEP responses and to gain insight into the conditions that generate a high-energy tail, independent of the initial $\gtrsim$ 30 keV flux level. Superposed epoch analysis of mesospheric NO density from SOFIE confirms an observable direct impact on lower mesospheric chemistry associated with the absolute E3 events. A probability assessment based on absolute events identifies specific thresholds in the solar wind-magnetosphere coupling function (epsilon) and the geomagnetic indices Kp*10 and Dst, capable of determining the occurrence or exclusion of absolute E1 and E3 events. Elevated solar wind speeds persisting in the recovery phase of a deep Dst trough appear characteristic of overlapping and relative E3 events. This study provides insight into which parameters are important for accurately modeling the high-energy tail of EEP.

KEYWORDS

energetic electron precipitation (EEP), medium energy electrons, high-energy tail electrons, solar wind parameters, geomagnetic indices, electron flux, MEPED

1 Introduction

Energetic electron precipitation (EEP) creates chemically reactive species that can catalyze ozone loss in the polar mesosphere and stratosphere, altering the radiation budget and atmospheric dynamics. EEP refers to accelerated electrons in the magnetosphere that are guided down into the mid-to-high latitude atmosphere by Earth's magnetic field. The electrons deposit their energy in the atmosphere by ionization, dissociation, or excitation of atmospheric gasses. These reactions can lead to the production of the chemically reactive NO_x (N, NO, and NO_2) and HO_x (H, OH, and HO_2) species (Sinnhuber et al., 2012) that can catalytically destroy mesospheric and stratospheric ozone. Altering the ozone concentration will affect the local temperature, initiating complex dynamical feedback loops. These atmospheric changes impact upper atmospheric circulation by strengthening the stratospheric polar vortex, which ultimately can map down onto regional surface climate during winter (Baldwin and Dunkerton, 2001; Seppälä et al., 2009; Seppälä et al., 2013; Maliniemi et al., 2016).

NO_x species are particularly important due to their long lifetime of several days to weeks during high-latitude winter darkness (Solomon et al., 1982). EEP-produced NO_x can influence mesospheric and stratospheric ozone concentrations through direct and indirect mechanisms dictated by the energy spectrum of the precipitating electrons. Compositional changes due to EEP-induced production of NO_x at lower mesospheric and upper stratospheric altitudes are known as the EEP direct effect, while changes due to downward transportation of NO_x are known as the EEP indirect effect (Randall et al., 2007).

A main driver of the EEP indirect effect is the frequent auroral electron precipitation. These electrons originate predominantly from the plasmasheet and have energies up to about 30 keV (Newell et al., 2004; Khazanov and Glocer, 2020), reaching the lower thermosphere and upper mesosphere. During polar winter darkness, auroral precipitation leads to an abundant NO_x concentration in the lower thermosphere around 100 km altitude. The residual circulation during polar winters allows NO_x to be dynamically transported to lower mesospheric and stratospheric altitudes, where it can efficiently destroy ozone (Solomon et al., 1982; Damiani et al., 2016; Maliniemi et al., 2021).

On the other hand, medium energy electron (MEE) precipitation, with energies from about 30 keV to 1 MeV, can play a direct role in altering lower mesospheric and upper stratospheric ozone concentration (Smith-Johnsen et al., 2017). MEE precipitation originates predominantly from the ring current and radiation belts (Li and Hudson, 2019) and deposits energy in the mesosphere below 90 km altitude. Moreover, the high-energy tail of MEE, characterized by energies surpassing 300 keV, can reach the lower mesosphere and even touch the stratosphere (Turunen et al., 2009), between altitudes of 70 to 50 km (Xu et al., 2020; Pettit et al., 2023). At these low altitudes, the production of NO_x from the high-energy tail of MEE can directly impact ozone concentrations (Damiani et al., 2016; Zawedde et al., 2019).

High-energy protons (1–50 MeV) originating directly from the Sun, known as solar proton events (SPEs), can also precipitate all the way down to the stratosphere, leading to intense NO_x production and a direct impact on stratospheric ozone (Jackman et al., 2005; Seppälä et al., 2008; Funke et al., 2011; Nesse Tyssøy et al., 2013; Nesse Tyssøy and Stadsnes, 2015; Zawedde et al., 2018). The effects of the infrequent SPEs on the production of NO_x have been widely explored. Similarly, the effects of the frequent auroral EEP on thermospheric NO_x are fairly well established (Marsh et al., 2004; Sinnhuber et al., 2011). The MEE precipitation spectrum is, however, harder to parameterize, especially when considering its high-energy tail. The Medium Energy Proton and Electron Detectors (MEPED) aboard the Polar Operational Environmental Satellites (POES) and European Organisation for the Exploitation of Meteorological Satellites (EUMETSAT) MetOp have the advantage of observing within the bounce loss cone (BLC) at polar latitudes, with several operational satellites over multiple solar cycles. Nonetheless, due to instrumental challenges and different data handling within the community, parameterization of MEE leads to a large range of ionization and electron flux estimates (Nesse Tyssøy et al., 2022; Sinnhuber et al., 2022) and is currently a highly active field of research (Beharrell et al., 2015; van de Kamp et al., 2016; van de Kamp et al., 2018; Mironova et al., 2019; Pettit et al., 2019; Tyssøy et al., 2019; Duderstadt et al., 2021; Partamies et al., 2021; Tyssøy et al., 2021; Tyssøy et al., 2021; Babu et al., 2022; Nesse Tyssøy et al., 2022; Zúñiga López et al., 2022; Babu et al., 2023; Nesse et al., 2023; Salice et al., 2023). Other initiatives, such as the UARS satellite (Winningham et al., 1993) and the ELFIN twin CubeSats (Angelopoulos et al., 2023), have also monitored high-energy EEP within the BLC but not with the same coverage.

EEP is acknowledged as one of the relevant factors in understanding stratospheric ozone depletion, and a parameterization of EEP is now an official input to the Coupled Model Intercomparison Project phase 6 (CMIP6) (Matthes et al., 2017). However, the difficulties and uncertainties in parameterizing the MEE aspect of EEP propagate into the chemistry-climate model projections, and hence, their chemical effect is not fully captured (Sinnhuber et al., 2022). Particularly, today's models are underestimating the amount of NO_x in the lower mesosphere and stratosphere (Randall et al., 2015; Pettit et al., 2019; Sinnhuber et al., 2022). Research highlights the importance of considering the full spectrum of EEP to fully understand its impact on the atmosphere (Randall et al., 2015; Smith-Johnsen et al., 2017; Pettit et al., 2019; Zúñiga López et al., 2022).

The MEE ionization rates in CMIP6 are based on van de Kamp et al. (2016)'s daily resolved model, designed for 30–1,000 keV radiation belt-driven EEP. This model utilizes all three electron energy detectors from the 0° MEPED onboard the NOAA POES from 2002 to 2012. The model is scaled by the daily Ap index and is meant to give the average expected flux spectra used to calculate atmospheric ionization on a daily scale (van de Kamp et al., 2016). One of the advantages of this model is that the Ap index can be reconstructed back until 1850 (Matthes et al., 2017), allowing for MEE parameterization way beyond satellite measurements. However, the accuracy of the model's representation of flux and ionization rate levels is a highly active discussion (Mironova et al., 2019; Pettit et al., 2019; Tyssøy et al., 2019; Nesse Tyssøy et al., 2022; Sinnhuber et al., 2022), and improvements are suggested by the community for CMIP7 (Funke et al., 2023).

Tyssøy et al. (2019) compared the CMIP6 Ap-based model with estimates of loss cone fluxes using both the 0° and 90°

MEPED detectors combined with pitch angle distributions from wave-particle interaction theory. They found that by only using measurements from the 0° detector, the Ap model underestimates flux strength by one order of magnitude. The HEPPA III Intercomparison project compared eight estimates of MEE ionization rates (Nesse Tyssøy et al., 2022) and NO observations (Sinnhuber et al., 2022) during an extreme geomagnetic storm in 2010. They found that the Ap model provides the lowest ionization rates of all the eight models and, consequently, the lowest NO concentrations in the mesosphere. Tyssøy et al. (2019) also found that the Ap model struggles to accurately represent flux levels during intense geomagnetic storms, as its performance plateaus for Ap values greater than 40. It also falls short in capturing the duration of flux levels during extended recovery phases (Tyssøy et al., 2019). Given that Coronal Mass Ejections (CMEs) frequently result in intense geomagnetic storms and High-speed Solar Wind Streams (HSSs) are recognized for their extended duration, the Ap model's shortcomings introduce a systematic bias throughout a solar cycle. This bias arises because CMEs are prevalent during solar maxima, while HSSs dominate the declining phase of the solar cycle (Asikainen and Ruopsa, 2016).

Tyssøy et al. (2019) suggested that the caveats of the Ap model regarding the general underestimation of flux could be solved by utilizing the estimates of loss cone fluxes from both the 0° and 90° detectors. However, a further understanding of MEE and its properties is necessary to capture the variability during especially strong flux responses, not only when it comes to the absolute flux response but also its duration. Research has found that the high-energy tail of MEE behaves differently compared to lower energies regarding quantity, timing, and duration (Ødegaard et al., 2017; Salice et al., 2023). The significance of MEE precipitation on atmospheric chemistry, debated in various studies (Clilverd et al., 2009; Newnham et al., 2011; Sinnhuber et al., 2011; Daae et al., 2012; Sinnhuber et al., 2014; Kirkwood et al., 2015), stems partly from limited particle measurements and scarce NO observations in the polar atmosphere, and partly from the significantly lower fluxes compared to auroral precipitation. This leads to lower production rates, further complicating assessing their atmospheric effects (Randall et al., 2007; Sinnhuber et al., 2014; Randall et al., 2015). Recent research, however, indicates that even weak fluxes of MEE precipitation can markedly impact atmospheric chemistry and dynamics under specific atmospheric conditions (Smith-Johnsen et al., 2017; Ozaki et al., 2022; Zúñiga López et al., 2022; Nesse et al., 2023).

This study aims to understand the distinct characteristics of the high-energy tail of MEE precipitation ($\gtrsim$ 300 keV) compared to its lower-energy counterpart ($\gtrsim$ 30 keV). The motivation stems from the observed underestimation of EEP flux parameterization, especially during periods of strong solar and geomagnetic activity. To address this, the BLC MEE fluxes, derived from observations by both the 0° and 90° MEPED instruments onboard the POES/MetOp satellite series, are employed with a daily resolution. Flux peaks in the > 43 keV electron flux that exceed the 90th percentile from 2004 to 2014 are identified and categorized based on their corresponding absolute and relative >292 keV flux responses. Selecting these peaks allows the study to specifically focus on strong events that are often averaged out in EEP parameterization. The specific aim is to identify predictive parameters of the high-energy tail of MEE, enabling a better parameterization of the full range of EEP. Such improvements are crucial for achieving a more accurate depiction of both the magnitude and altitude-specific distributions of the chemical impact driven by EEP. Moreover, a better understanding of the behavior of the high-energy tail of MEE will further illuminate its fundamental physics and driving mechanisms.

This paper is organized as follows: Section 2 and Section 3 describe the data and methods used, Section 4 presents the results, Section 5 provides a discussion, and lastly, Section 6 provides the conclusions.

2 Data

2.1 MEPED on the POES/MetOp satellites

The Polar Operational Environmental Satellite (POES) series and the Meteorological Operational (MetOp) satellites are Sun-synchronous, low-altitude polar-orbiting spacecraft operated by the National Oceanic and Atmospheric Administration (NOAA) and the European Organisation for the Exploration of Meteorological Satellites (EUMETSAT), respectively. The spacecraft orbit at ~850 km altitude with a period of ~100 min, resulting in 14–15 orbits per day (Evans and Greer, 2004). From 2007 to 2014, six satellites were operational: NOAA 15, NOAA 16, NOAA 17 (up until 2013), NOAA 18 (from 2005 and onward), NOAA 19 (from 2009 and onward), and MetOp-02 (from 2006 and onward). All six satellites operated with the newest instrument package SEM-2 of the Medium Energy Proton and Electron Detector (MEPED). The combined measurements from the different satellites give a near-continuous observation of MEE precipitation from 1979 until today.

MEPED has two proton and two electron solid-state detector telescopes. The electron detectors measure MEE fluxes in three bands within the range 30–2,500 keV (Evans and Greer, 2004). The nominal electron energy limits as given in Evans and Greer (2004) are >30, >100, and >300 keV denoted as E1, E2, and E3, respectively. When in operation, the true electron energy limits depend on the incoming electron energy spectrum (Yando et al., 2011). Applying the geometric factors given in Yando et al. (2011), Ødegaard et al. (2017) determined new optimized-effective integral energy limits and associated geometric factors based on a series of realistic power laws and exponential spectra. The highest MEPED proton channel (P6) gets contaminated by relativistic electrons. Yando et al. (2011) confirmed that P6 can detect relativistic electron precipitation during little to no high-energy proton fluxes. Table 1 shows the new optimized lower energy limits for the three electron channels and the highest proton channel.

The electron and proton solid-state detectors consist of a 0° and a 90° telescope. When the satellites travel across high geomagnetic latitudes, the 0° telescope will mainly measure particle fluxes that will be lost to the atmosphere. In contrast, the 90° telescope will mainly measure particles trapped in the radiation belts (Rodger et al., 2010). The energetic electron fluxes are often strongly anisotropic with decreasing fluxes towards the center of the bounce loss cone (BLC, the region where particles will be lost to the atmosphere) (Nesse Tyssøy et al., 2016). Hence, the 0°

TABLE 1 Nominal detector responses in the three electron channels E1, E2, and E3 and the highest proton energy channel, P6, of the SEM-2 MEPED (Evans and Greer, 2004) and the new optimized integral energy limits for the different channels (Ødegaard et al., 2017).

Energy channel	Nominal lower limit [keV]	New optimized lower limit [keV]
E1	>30	>43
E2	>100	>114
E3	>300	>292
P6	-	>756

telescope will underestimate, and the 90° telescope will overestimate the precipitating electron fluxes.

Separately, the two telescopes do not accurately estimate the precipitating electron fluxes. Combining measurements from the 0° and 90° telescopes with electron pitch angle distributions from theories of wave-particle interactions in the magnetosphere, Nesse Tyssøy et al. (2016) estimated a complete BLC flux for each electron energy channel. Low-energy proton contamination is removed based on the proton telescope data. First, the proton observations are corrected for degradation due to radiation damage by applying correction factors derived by Sandanger et al. (2015) and Ødegaard et al. (2016). Subsequently, the proton flux in the energy intervals known to impact the respective electron channels (Evans and Greer, 2004) is subtracted from the originally measured electron fluxes (Nesse Tyssøy et al., 2016). The Fokker-Planck equation for electron diffusion (Kennel and Petschek, 1966; Theodoridis and Paolini, 1967) is solved for a wide range of diffusion coefficients and transformed to the satellite altitude. Taking into account the viewing directions of the telescopes relative to the magnetic field and the detector response function for different viewing angles through the detector collimator, the ratio between the fluxes detected by the 0° and 90° detector is used to identify the theoretical pitch angle distribution that best corresponds to the observations. Finally, the flux corresponding to the pitch angle range of the BLC is estimated. The size of the BLC is calculated using the International Geomagnetic Reference Field (IGRF) model. For further details on the method used to estimate the BLC fluxes, see Nesse Tyssøy et al. (2016).

This study utilizes the BLC fluxes with the new optimized effective integral limits >43, >114, >292, and >756 keV, denoted as E1, E2, E3, and P6. Figure 1 shows the coverage of the three operating NOAA satellites on the 25th of March 2004 for the Northern Hemisphere (NH) and Southern Hemisphere (SH). In the NH, data scarcity is observed around the midnight sector, corresponding to 0 magnetic local time (MLT). In the SH, the data gap is prominent around midday or 12 MLT.

To achieve a robust global daily average flux for 2004–2014, measurements from both hemispheres for all available MEPED data are used (see example to the right in Figure 1). This approach offers more comprehensive data points and enhanced MLT coverage. However, as different MLT sectors still have varying coverage, the daily average flux calculation is first segmented into four distinct MLT sectors: 0–6, 6–12, 12–18, and 18–24 MLT. The global daily flux is then determined by averaging the values across these four MLT sectors over the corrected geomagnetic (CGM) latitude bands: 55°–70° in the NH and −55°–70° in the SH.

During large SPEs, proton contamination dominates the counts in the MEPED electron detector, making the remaining electron fluxes after the respective proton correction uncertain (Nesse Tyssøy et al., 2016). As such, the electron fluxes with SPEs exceeding 200 particle flux units (pfu), equivalent to 200 protons $cm^{-2}s^{-1}sr^{-1}$, have been excluded from the flux data from the SPE onset to 20°days after. The long “buffer” period after an SPE event minimizes the impact on the NO climatology and prevents SPE NO production from being misinterpreted as an EEP effect.

Overall, the BLC fluxes are an optimized estimate based on known physics and available instrumentation. Still, the pitch angle diffusion theory by Kennel and Petschek (1966) assumes steady-state conditions, which can lead to uncertainties in geomagnetic active periods (Shen et al., 2023). Moreover, a recent idealized model study by Selesnick et al. (2020) points out that the sensitivity of the 0° detector outside the nominal field of view may cause it to be susceptible to quasi-trapped or trapped electrons during periods of weak pitch angle diffusion, hence exaggerating the fluxes. Although the method applied in our study does not assume a uniform angular response, some contamination from electrons outside the nominal field of view affecting the loss cone estimates cannot be excluded.

2.2 SOFIE on the AIM satellite

The Solar Occultation For Ice Experiment (SOFIE) instrument onboard NASA’s Aeronomy of Ice in the Mesosphere (AIM) satellite has been measuring temperature, ice water content, and trace gases (H_2O, CO_2, O_3, CH_4, and NO) in the polar middle atmosphere since its launch in May 2007 (Gordley et al., 2009). The satellite has a polar, Sun-synchronous orbit with a period of 96 min, giving 15 orbits per day. The SOFIE instrument measures vertical NO profiles twice per orbit, one in the NH and one in the SH, during local sunset and sunrise, respectively. The latitudinal coverage depends on the time of year and varies from 65° to 85°. The vertical profiles of NO are from 30 up to 150 km with a vertical resolution of 1 km taken every 0.2 km.

During Northern Hemisphere sunrise measurements, large thermal oscillations in the SOFIE detector lead to non-retrievable NO data below 80 km [see Gómez-Ramírez et al. (2013) for further details on retrieval methods and applied corrections for the NO signal measured by SOFIE]. Additionally, sudden stratospheric warming events occur more commonly in the NH, complicating the typical polar vortex descent by bringing NO-enriched air down to the middle atmosphere. In the investigated period, no sudden stratospheric warming events occurred in the SH (Hendrickx et al., 2015). Hence, this study limits it is NO measurements to the SH, where instrument complications and sudden stratospheric warming events do not affect the NO data profiles.

This study utilizes the complete SOFIE NO data (version 1.2) publicly accessible on https://sofie.gats-inc.com/getdata, focusing on observations made over the SH from 2007 to 2014. Figure 2 presents the vertical profile of NO density, with data points provided at a daily resolution and covering an altitude range from 35 km to 150 km. One of the noteworthy features displayed in the Figure is the NO reservoir, which is consistently evident around an altitude

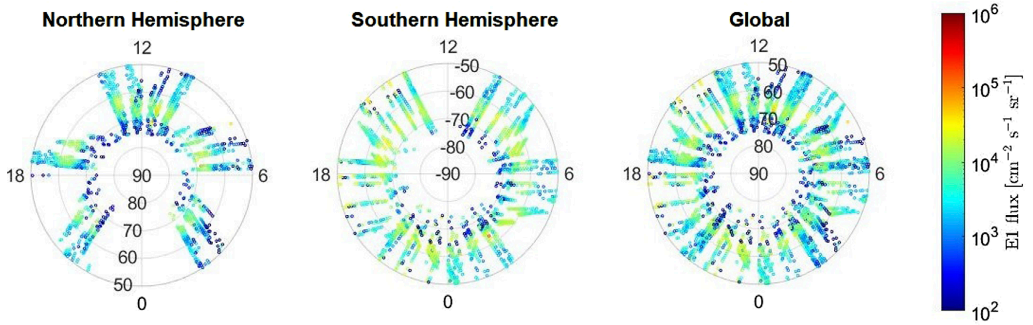

FIGURE 1
The satellite coverage of the three NOAA satellites, 15, 16, and 17, over a full day on 25 March 2004, for the Northern, Southern, and both hemispheres combined to represent a global flux. The >43 keV flux measurements for each point are indicated by the color bar.

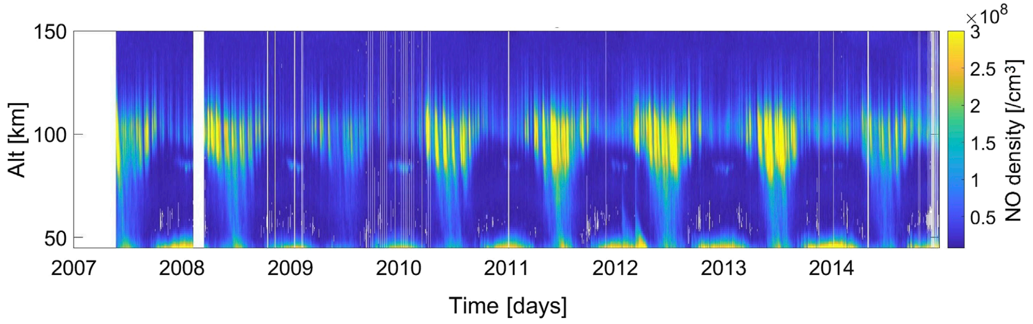

FIGURE 2
The Southern Hemisphere NO density [/cm^3] data retrieved from the SOFIE instrument onboard NASA's AIM satellite from 2007 to 2014. The data has a daily resolution from 35 to 150 km altitude.

of 100 km. This reservoir persists even during the SH's summer months but becomes more prominent and extends further down into the atmosphere during winter. Additionally, the Figure shows an increased concentration of NO extending to an altitude of 50 km, a particularly noticeable phenomenon in the winter months.

2.3 Solar wind classification

Three primary types of solar wind flow are distinguished based on their origins from the Sun and by near-Earth solar wind parameters. Richardson and Cane (2012)'s definitions of solar wind structures are as follows:

- High-speed streams (HSSs), which originate from the Sun's coronal holes. Solar wind speeds of $v \gtrsim 450$ km/s characterize these streams. Co-rotating interaction regions (CIR) are compressed regions between the fast streams and the preceding slower, cooler, and denser solar wind. Both the fast stream itself and the co-rotating interaction are under the term HSS.
- Transient flows connected with coronal mass ejections (CMEs). These flows comprise interplanetary CMEs (ICMEs, e.g., Kilpua et al., 2017), which are solar wind manifestations of the CMEs, as well as their associated upstream shocks and post-shock/sheath regions. CMEs, their shocks, and sheaths are collected under the term "CMEs".
- The slower, inter-stream solar wind, typically affiliated with the Sun's streamer belt.

This study uses an extended solar wind structure list from 2004 to 2014 based on the classification presented in Richardson and Cane (2012), and references therein).

3 Methods

In this study, flux peaks above the 90th percentile of the >43°keV flux are identified before being categorized by the associated absolute or relative >292 keV peak flux:

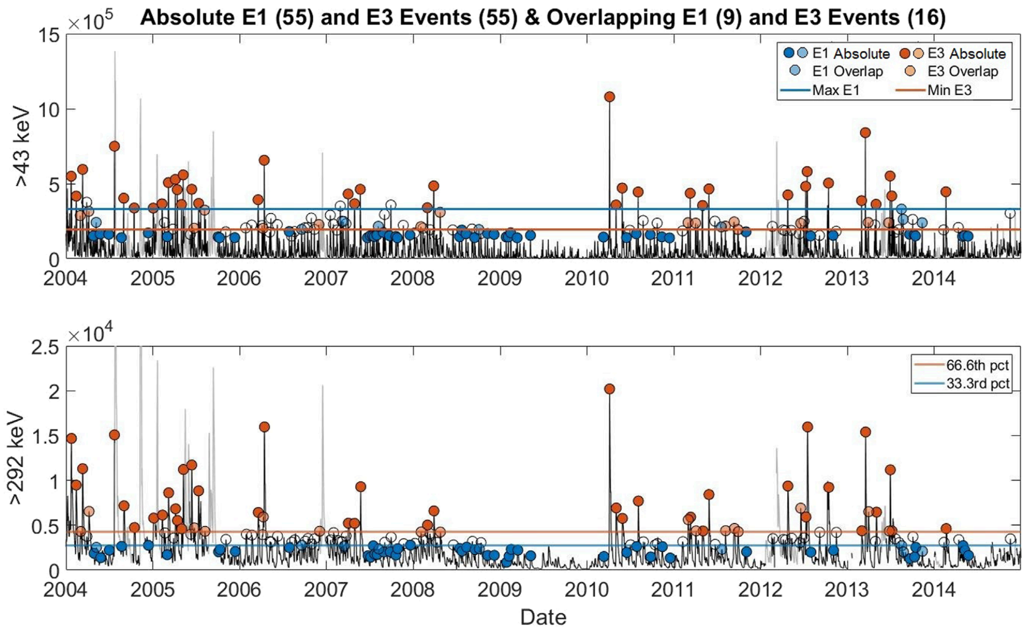

FIGURE 3
Electron fluxes for >43 keV (top) and >292 keV (bottom) energy channels from 2004 to 2014 are shown as black lines, with light grey segments indicating SPE exceeding 200 pfu. Circles mark the 164 flux peaks above the 90th percentile of >43 keV flux, with filled and subdued blue/red circles representing absolute E1/E3 events, respectively. The subset of overlapping E1 and E3 events is shown by just the subdued blue and red circles. In the bottom panel, blue and red lines indicate the 33.3rd and 66.6th percentiles of the 164 peak fluxes in the >292 keV channel corresponding to absolute E1 and E3 event thresholds. In contrast, in the top panel, the lines represent the strongest and weakest >43 keV fluxes for absolute E1 and E3 events, corresponding to overlapping E1 and E3 thresholds. Flux units are in $cm^{-2}s^{-1}sr^{-1}$.

- Events with a weak or strong >292 keV peak flux are termed absolute E1 and E3 events.
- Events with a weak or strong >292 keV peak flux scaled by the >43 kev flux peak are termed relative E1 and E3 events.

Focusing on flux peaks above the 90th percentile of the >43°keV flux specifically targets the most intense events, which are often averaged out in EEP parametrizations. The aim of studying the absolute events is to identify how strong solar wind properties and geomagnetic disturbances need to be to give high >292 keV flux responses. Additionally, by examining a subset of absolute E1 and E3 events with similar/overlapping >43 keV peak fluxes, we seek to gain a deeper understanding of the specific conditions associated with acceleration and precipitation of the high-energy tail. The >292 keV peak flux correlates with the >43 keV peak flux; however, for a specific >43 keV value, the corresponding >292 keV peak flux can vary by an order of magnitude (Salice et al., 2023). Hence, exploring the relative increase between >43 and >292 keV peak fluxes allows for further insight into the conditions favorable for generating a high-energy tail, independent of the initial >43 keV flux level and total energy flux. This section will offer comprehensive details on the selection criteria for absolute, overlapping, and relative E1 and E3 events.

3.1 Identifying absolute and overlapping E1 and E3 events

Figure 3 displays the global daily >43 keV (top panel) and >292 keV (bottom panel) flux data from both the Northern and Southern Hemispheres over a complete solar cycle spanning 2004 to 2014. The black lines represent the global flux values, with excluded SPEs shown in light grey. Peaks in the >43 keV electron flux exceeding the 90th percentile ($\sim 1.4 \times 10^5$ $cm^{-2}s^{-1}sr^{-1}$) were identified. For peak isolation, the >43 keV flux had to fall below its median value ($\sim 2.2 \times 10^4$ $cm^{-2}s^{-1}sr^{-1}$) before considering the next peak. Additionally, there had to be no missing data up to 5 days after the identified peak. This resulted in 164 distinct peaks. The associated flux peaks in the >292 keV channel were identified based on a window from the day of the >43 keV peaks to 4 days later (Ødegaard et al., 2017; Salice et al., 2023). The 164 peaks are shown in Figure 3 in both energy channels by circles, both empty and filled.

From the identified 164 peaks, two types of events are categorized based on the corresponding >292 keV flux peaks. Absolute E1 events comprise the third with the lowest >292 keV flux peaks, while absolute E3 events represent the third with the highest. The dividing thresholds between the events in the >292 keV flux are marked in the bottom panel: the 33.3rd percentile (blue line) at

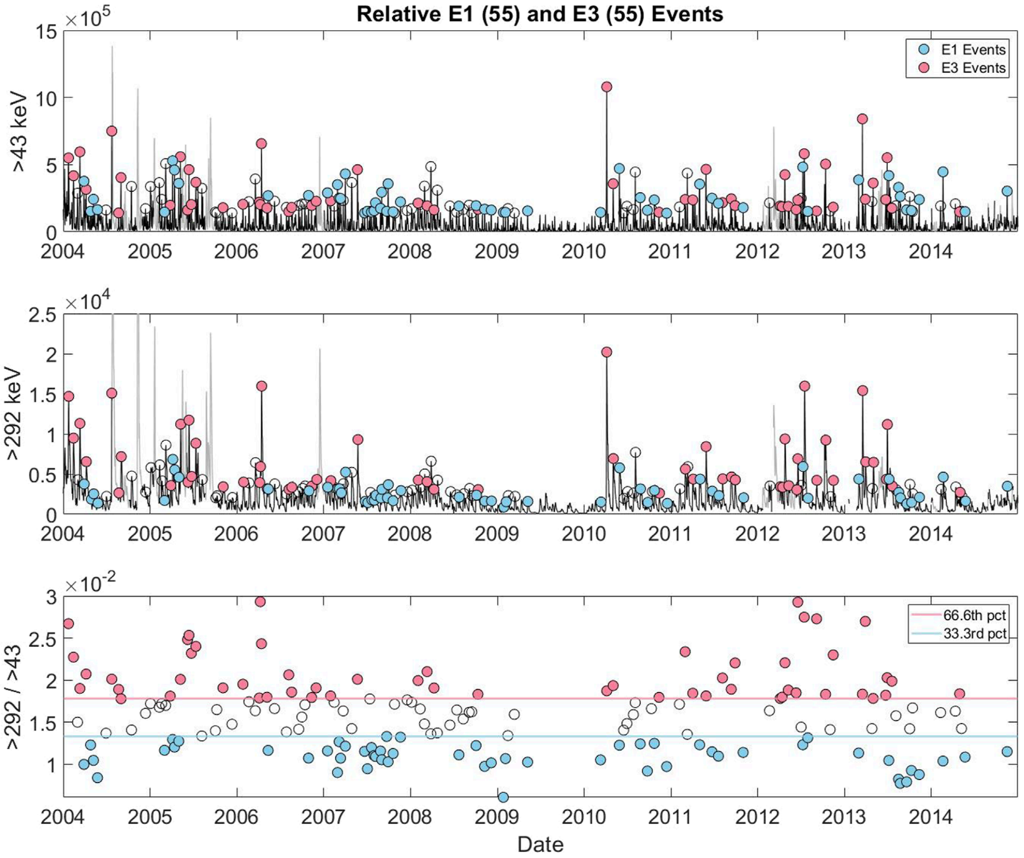

FIGURE 4
The top panel shows the >43 keV flux with circles representing the 164 flux peaks exceeding the 90th percentile. The middle panel mirrors this representation for the >292 keV flux. The bottom panel shows the ratio of >292 keV to >43 keV peak fluxes for the 164 peaks. In all panels, circles filled in light blue and pink circles denote the relative E1 and E3 events, categorized by the lowest and highest third ratios, respectively. The horizontal lines in the bottom panel mark the 33.3rd (light blue) and 66.6th (pink) percentile thresholds of the ratios. Flux units are in cm^{-2}s^{-1}sr^{-1}.

~2.8×10^3 cm^{-2}s^{-1}sr^{-1} and the 66.6th percentile (red line) at ~4.2×10^3 cm^{-2}s^{-1}sr^{-1}. This results in 55 absolute E1 and 55 absolute E3 events, shown as blue and red circles in Figure 3, respectively. The event peaks are shown in both energy channels and include the faded blue and red peaks as well.

The absolute E3 events shown in Figure 3 generally have higher >43 keV fluxes than absolute E1 events, though multiple exceptions exist. Figure 3 further distinguishes a subset of absolute E1 and E3 events with similar >43 keV fluxes, termed overlapping E1 and E3 events. This subset of overlapping events is determined by two boundaries in the >43 keV flux. The upper boundary is represented by the blue line in the top panel of Figure 3, denoting the strongest >43 keV flux peak among absolute E1 events on the 16th of August 2013 at ~3.3×10^5 cm^{-2}s^{-1}sr^{-1}. The lower boundary is marked by the red line, indicating the weakest >43 keV flux peak within absolute E3 events on the 28th of September 2011, at ~1.9×10^5 cm^{-2}s^{-1}sr^{-1}. 9 overlapping E1 and 16 overlapping E3 events fall within these boundaries. The subset of overlapping events is shown by the faded blue and red circles in both panels of Figure 3, respectively.

Note that the low number of overlapping events only provides a preliminary insight. The following discussion and conclusion will mainly rely on the more extensive dataset.

3.2 Identifying relative E1 and E3 events

In Figure 4, as in Figure 3, the top panel displays the >43 keV flux with the 164 flux peaks above the 90th percentile as circles, both empty and filled. The middle panel mirrors this representation for the >292 keV flux. The bottom panel shows the ratio of >292 keV and >43 keV peak flux for the 164 peaks. Relative E3 events are defined as the third with the highest ratio, while relative E1 events are defined as the third with the lowest ratio. This results in 55 relative E1 and 55

TABLE 2 Overview of the number of absolute, overlapping, and relative E1 and E3 events primarily driven by CMEs or HSSs.

		Nr. of events	CME	HSS
Absolute events	E1	55	9	44
	E3	55	26	28
Overlapping events	E1	9	2	7
	E3	16	6	10
Relative events	E1	55	11	43
	E3	55	27	27

relative E3 events, shown as light blue and pink circles in Figure 4, respectively.

Among the 110 absolute and 110 relative events, 77 are designated as both. 32 events are classified as absolute E1 and relative E1 events, meaning they have a >292 keV flux response that is both low and relatively low compared to the >43 keV flux. 32 events are classified as absolute and relative E3 events with high and relatively high >292 keV flux response. There are, in total, 13 events that are absolute E1 and relative E3 or absolute E3 and relative E1 events. A comprehensive event list is provided in the data availability section for reference.

3.3 Classifying events by solar wind structure

For absolute, overlapping, and relative event peaks in the >43 keV energy channel, the dominant solar wind structure on that day and the preceding day were retrieved based on the classification described in Section 2.3. The classification follows Richardson and Cane (2012)'s definitions and list of solar wind structures from 2004 to 2014. In this study, an event is categorized as CME-driven if a CME drives either day. If neither day is a CME but at least one is an HSS, the event is classified as HSS-driven. Events not fitting these criteria are not categorized with a specific solar wind structure. The distribution of these classifications for the events is summarized in Table 2. Notably, two absolute and one relative E1 event, as well as one absolute and one relative E3 event, are not associated with any solar wind structure.

Out of the 55 absolute E1 events, 44 are driven by HSSs, while only 9 are driven by CMEs. In contrast, absolute E3 events display a more balanced distribution between the two solar wind structures, with 28 driven by HSSs and 26 by CMEs. This pattern is also observed in the relative events, while the overlapping events are largely HSS-driven.

4 Results—superposed epoch analysis

In this section, a superposed epoch analysis (SEA) for the absolute E1 and E3 events, the associated subset of overlapping E1 and E3 events, and the relative E1 and E3 events are performed. The median epoch values and the 25th and 75th percentiles are calculated for all variables. For both E1 and E3 events, the epoch time (onset) is defined as the peak in the >43 keV electron flux (see top panels of Figures 3, 4). The time ranges from 5 days before to 10 days after onset. Section 4.1 presents the SEA of the global MEE flux data and observed NO density for selected events, and Section 4.2 shows the SEA for the associated solar wind and geomagnetic data. Further, Section 4.3 sorts the selected events by their solar wind drivers, reproducing the SEA for flux response, solar wind parameters, and geomagnetic indices. Lastly, in Section 4.4, the occurrence probability of absolute E1 and E3 events for specific solar wind and geomagnetic parameters is analyzed.

4.1 MEE fluxes and associated atmospheric NO impact

4.1.1 Flux response

Figure 5 presents a SEA of the daily flux evolution for absolute, overlapping, and relative E1 (blue/light blue) and E3 (red/pink) events across the various integral electron energy channels.

The left panels in Figure 5 reveal a distinct response in the >43 keV energy channel for both absolute event categories, but with the E3 events having a peak flux 2.6 times that of E1 (~3.9×10^5 vs. ~1.5×10^5 cm^{-2}s^{-1}sr^{-1}) and a longer period of elevation. In the higher energy channels, the flux during E3 events remains 2.5 to 3.5 times stronger than during E1 events. Specifically in the >292 keV channel, the E3 events have a median flux 3 times greater, peaking at ~5.9×10^3, whereas E1 events peak at ~2.0×10^3 cm^{-2}s^{-1}sr^{-1}.

As anticipated based on our selection criteria, the middle panels present the overlapping E1 and E3 events with similar peak fluxes in the >43 keV energy channel. Here, E1 and E3 events register a peak flux both at ~2.4×10^5 cm^{-2}s^{-1}sr^{-1}. Notably, the overlapping E3 events in this channel portray a wider peak, indicating a prolonged period of heightened flux compared to the E1 events. As the energy increases, the difference between the fluxes grows, with the E3 peaks being 1.8 times that of the E1 peaks in the >292 keV channel, with ~4.3×10^3 and ~2.4×10^3 cm^{-2}s^{-1}sr^{-1}, respectively.

The right panels show that the relative E1 and E3 events have similar >43 keV peak fluxes at ~2.2×10^5 and ~2.3×10^5 cm^{-2}s^{-1}sr^{-1}, respectively. These values correspond to the flux level of the overlapping events, however, with a wider percentile range. Analog to the overlapping events, the peak is wider in relative E3 events than in relative E1 events. The discrepancy between the SEA fluxes increases with energy as seen for overlapping events, resulting in the relative E3 events peaking at 1.8 times that of E1 events in the >292 keV channel (~4.3×10^3 vs. ~2.4×10^3 cm^{-2}s^{-1}sr^{-1}).

For all three event categories, E3 events consistently display elevated >292 keV fluxes in the days preceding the onset compared to E1 events. This suggests a higher baseline flux associated with the E3 event periods.

A noteworthy observation from Figure 5 is the temporal delay in flux peaks as energy increases, a trend evident in all three sets of panels. In particular, the peak of the high-energy tail (>292 keV) is about 1–2 days delayed compared to the >43 keV flux peak.

Figure 6 displays the temporal differences between peak fluxes in the >43 keV and >292 keV energy channels. Delays span from

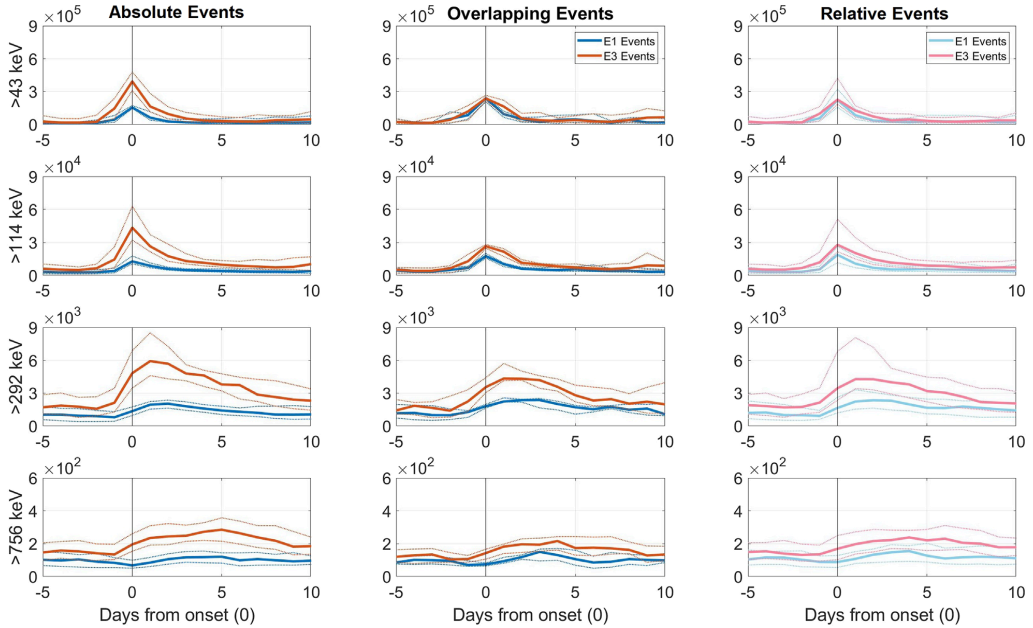

FIGURE 5
SEA of daily median electron flux evolution in various energy channels for absolute/relative E1 (blue/light blue) and E3 (red/pink) events. The left panels show the 110 absolute E1 and E3 events, the middle panels show the 25 overlapping E1 and E3 events, while the right panels display the 110 relative E1 and E3 events. Dotted lines in corresponding colors represent the 25th and 75th percentiles. The onset is the peak flux in the >43 keV electron channel for each event. Flux units are in cm^{-2}s^{-1}sr^{-1}.

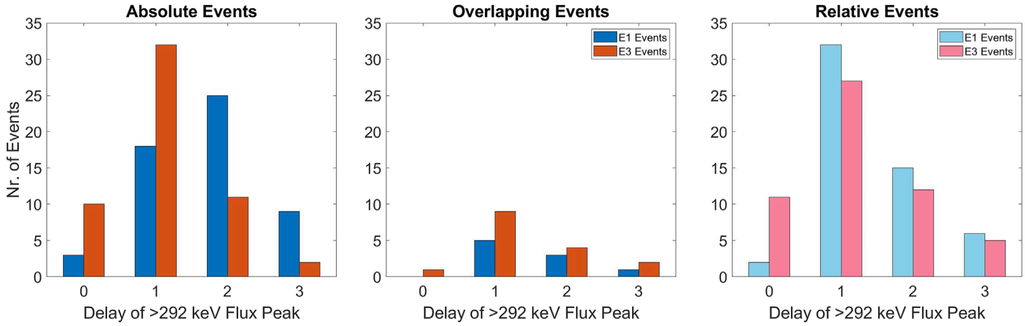

FIGURE 6
The occurrence rate of the zero-to 3-day delay in the >292 keV flux peak compared to the peak in the >43 keV flux. The absolute, overlapping, and relative categories are shown in the same sequence and colors as in Figure 5.

zero to 3 days. In this context, e.g., a 1-day delay indicates that the >292 keV peak occurs between day one and day two from onset.

Most notably, 45% of absolute events (left panel) have a 1-day delay in the >292 keV flux peak relative to the >43 keV peak. Absolute E3 events predominantly display a 1-day delay (58%), whereas absolute E1 events have the highest probability of a 2-day delay (45%). A majority (76%) of absolute E3 events have short delays of up to 1 day. Comparatively, most absolute E1 events have longer delays of more than 1 day (62%).

When focusing on overlapping events (middle panel), the delay spectrum remains zero to 3 days, with both E1 and E3 events having the highest probability of a 1-day delay (both 56%). Similarly, a 1-day delay is most common for the relative E1 (58%) and E3 (49%) events shown in the right panel. Relative E3 events also exhibit a high likelihood of rapid >292 keV peak responses with 20% demonstrating a 0-day delay. Conversely, the relative E1 events tend to have longer delays as only 4% have a 0-day delay.

These findings align well with existing literature (Salice et al., 2023, and references therein), which reports a high likelihood of a 1-day delay between the >43 keV and >292 keV electron flux peaks. Salice et al. (2023) also corroborates the influence of solar wind structures on these delays, indicating shorter delays for CME-driven events and longer delays for HSS-driven events. As about 80% of the absolute and relative E1 events are associated with HSSs (see Table 2), this analysis confirms the tendency for longer delays in >292 keV fluxes for HSS-driven events.

4.1.2 NO impact

In this subsection, we focus on variations in atmospheric nitric oxide (NO) concentrations, a crucial parameter that can further illuminate the distinct characteristics of E1 and E3 events.

Figure 7 presents a SEA of the mean SH change in NO relative to a 30-day smoothed mean baseline for each kilometer. The analysis spans altitudes from 60 to 150 km to capture NO variations throughout the mesosphere and lower thermosphere. Below 60 km, the variability in NO concentrations is influenced by dynamic atmospheric processes that can push NO to these altitudes. This fluctuating boundary layer of NO introduces noise into the data, obscuring the signals related to energetic electron precipitation, which is the focus of this study. The plots display isolated increases in NO concentration, separate from primary electron-induced enhancements; these are regarded as potential noise or phenomena unrelated to the events in question. Two dashed horizontal white lines mark the altitudes of 90 km and 70 km, which correspond to the approximate altitudes of the highest deposition rates for >43 keV and >292 keV precipitating electrons, respectively (Xu et al., 2020; Pettit et al., 2023). When analyzing the NO data, we focus on the days between 0 and 5 days from onset to identify the direct effect of EEP associated with the selected events.

The left-hand panels of Figure 7 show that both absolute E1 and E3 events exhibit at least a 60% increase in NO production above 90 km altitude from the onset day to 2 days later. There are, however, notable differences. For the E3 events, the intense increase in NO production covers a broader altitude range and persists through the third day. Though subtle, absolute E3 events display a tendency for NO production directly down to 60 km at two and 3 days from onset. Direct production for absolute E1 events is only visible down to 80 km on the second day from onset. Additionally, the EEP indirect effect, visible as a descending tail in the NO density profiles from the third-day post-onset, is more pronounced in E3 events. This notable tail suggests substantial NO transport from higher altitudes where its intensity is mainly scaled to the strength of the >43 keV fluxes. Although direct production cannot be entirely excluded, the >292 keV and >756 keV fluxes are orders of magnitude lower than the >43 keV fluxes and do not align with the observed intensity or depth of the NO tail (see Figure 5).

Given the smaller sample size of overlapping events shown in the middle panels of Figure 7, the data in these panels are more susceptible to statistical fluctuations due to factors such as season and noise, making it hard to draw strong conclusions. Additionally, the wide altitude ranges of NO increase visible 5 days from onset might be caused by new geomagnetic activity. Despite these challenges, the signature characteristic of a direct EEP effect down to 60 km 2 and 3 days after onset is still evident in the overlapping E3 events, as shown in the middle bottom panel. The middle top panel shows the overlapping E1 events with hints of NO production at low altitudes between zero to 4 days from onset, though not as pronounced as for the overlapping E3 events.

In the right panels of Figure 7, both the relative E1 and E3 events are associated with direct NO production below 70 km. For the E1 events, this is visible on the second day, and for E3 events, it is visible on the second and third days from onset. It is expected that both categories of relative events show direct production at low altitudes, as it is the absolute level of direct ionization that will influence the NO production. The relative E1 events with strong >292 keV fluxes have the potential to produce NO directly below 70 km. Similarly, there will be E3 events with insufficient >292 keV to contribute to observable NO densities. This is also shown in Figure 5, where there is a overlap between percentiles in the >292 keV flux channel for relative events.

Figure 5 shows that absolute E3 events tend to exhibit higher fluxes compared to absolute E1 events. Additionally, overlapping and relative E3 events display stronger >292 keV fluxes than their E1 counterparts despite having comparable >43 keV peak fluxes. Consistent with the flux observations, Figure 7 emphasizes the distinctions between E1 and E3 events regarding NO production's duration, intensity, and depth. Notable, absolute and overlapping E3 events have stronger NO responses reaching further down into the atmosphere over a longer time than their E1 counterparts. Both relative events show direct production down to 60 km but with the effect lasting longer for relative E3 events. In the next section, we will examine solar wind and geomagnetic data to explore the root causes of these observed disparities in Figures 5, 7 between E1 and E3 events.

4.2 Solar wind and geomagnetic responses

To model the distinct differences found in Section 4.1 between E1 and E3 events, the daily averaged solar wind and geomagnetic data as potential predictive variables for high-energy EEP are examined. To describe the solar wind forcing, the interplanetary magnetic field (IMF) component Bz [nT] in GSM coordinates, the solar wind bulk speed v [km/s], and the epsilon parameter ϵ [GW] measuring the coupling efficiency between the IMF and the magnetosphere are used. To describe the level of geomagnetic activity, we use the ring current sensitive Dst [nT] index, the Kp*10 index measuring global geomagnetic disturbances, and the AE [nT] index, which tracks magnetic activity in the auroral regions. All indices but epsilon are retrieved from the OMNI2 (formally OMNI) database with a daily resolution from 2004–2014. Epsilon is retrieved with a minute resolution from the SuperMAG database (Gjerloev,

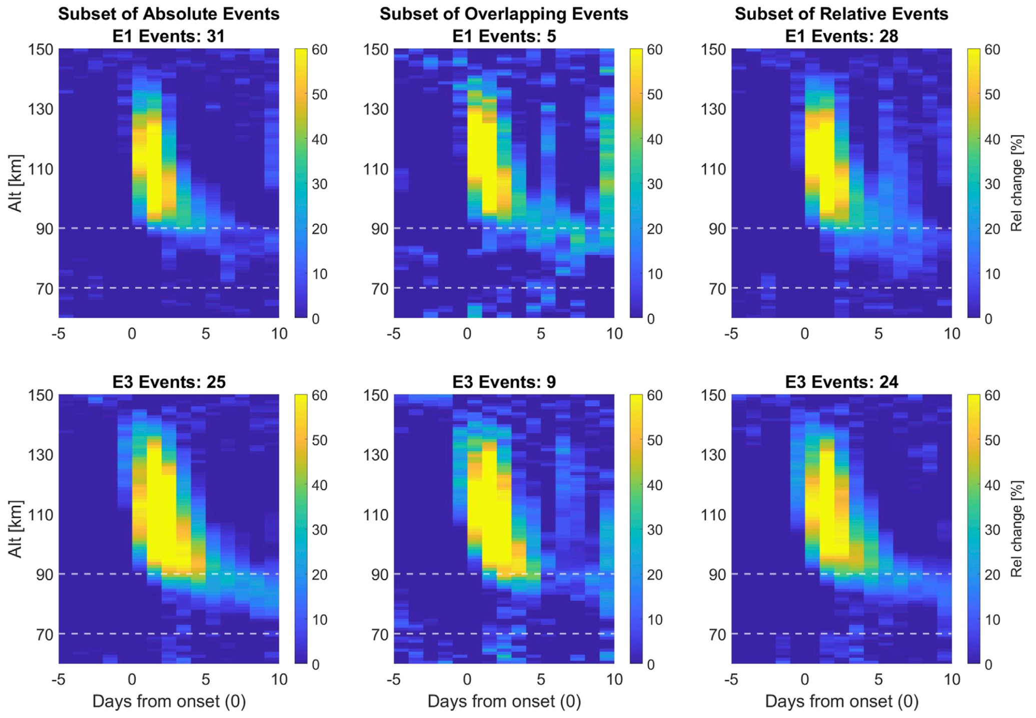

FIGURE 7
SEA comparing the daily relative increase in atmospheric NO concentrations for each category of E1 (top) and E3 (bottom) events. Data is displayed as a percentage above a 30-day smoothed mean for altitudes ranging from 60 to 150 km. The onset of events is defined consistently with Figure 5. All panels cover the time range of SOFIE measurements from May 2007 to 2014. Events with substantial missing data from onset to 4 days after are excluded. The subset of events included in each panel is indicated in their respective headings.

2012) and re-calculated to a daily average for the same period. Epsilon is given by:

$$\epsilon = \frac{4\pi}{\mu_0} \mathrm{v} \mathrm{B}^2 sin^4 \left(\frac{\theta}{2}\right) l_0^2 \tag{1}$$

The formulation of Eq. 1 draws from the work of Akasofu (1981) and is expressed in SI units (Watt) as specified by Koskinen and Tanskanen (2002). In this equation, the term $4\pi/\mu_0 = 10^7$, v represents the solar wind velocity, B denotes the total magnetic field in the solar wind, θ is the clock angle, and $l_0 = 7R_E$. Understanding the drivers is crucial for uncovering the mechanisms responsible for the distinct characteristics of E1 and E3 events, including their varied abilities to produce NO over specific time frames and altitudes. This section presents SEAs of solar wind parameters and geomagnetic indices associated with the E1 and E3 events.

4.2.1 Solar wind response

Figure 8 offers a SEA of the key solar wind parameters, Bz, v, and epsilon, where panels are organized as in Figure 5.

The left-hand panels in Figure 8 provide insights into the behavior of the three solar wind parameters for the absolute events, which tend to be stronger for E3. More specifically, absolute E3 events have, on average, a 3.8 times stronger southward orientation of Bz and a 2.2 times higher epsilon value than absolute E1 events. However, for solar wind speed, both event types display a 2-day plateaued peak with similar values where absolute E3 events are only 1.1 times faster. Elevated responses in the solar wind parameters tend to last longer for absolute E3 events. The 3-day southward trend of Bz surpasses the 1-day tendency of absolute E1 events, indicating a more prolonged southward alignment of the interplanetary magnetic field during absolute E3 events. Additionally, absolute E3 events exhibit a slightly higher speed from several days before to 4 days after onset and elevated epsilon values from the day before to the day after onset, exceeding the duration of E1 events by 2 days.

The middle and right panels in Figure 8 examine the overlapping and relative E1 and E3 events, respectively. The Bz parameter is similar through all three panels, with only relative E3 events showing a shorter duration of the southward alignment. For solar wind speed, the overlapping and relative E1 events show almost a 1.2 and 1.1 times stronger tendency, respectively, than the speed for the corresponding E3 events. However, overlapping and relative E3 events typically demonstrate a delayed peak or sustained elevation in solar wind speed 1 day post-onset, followed by a more gradual recovery than their E1 counterparts. This

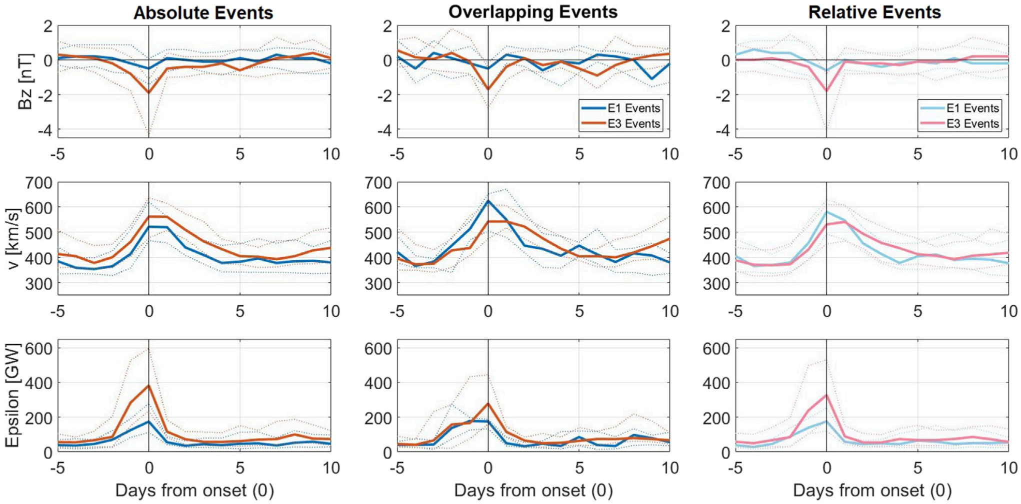

FIGURE 8
SEA of median daily solar wind properties for E1 and E3 events where the absolute, overlapping, and relative categories are shown in the same sequence and colors as in Figure 5. Solar wind properties displayed from top to bottom are the interplanetary magnetic field component in the *z*-direction (Bz), the solar wind bulk speed (v), and the solar wind-magnetosphere coupling function (epsilon).

time shift and prolonged impact for overlapping and relative E3 events is not evident for absolute events. The epsilon parameter for the relative events resembles that of absolute events, though with slightly weaker responses in the relative E3 events. For overlapping events, however, the responses between E1 and E3 are similar for the 2 days pre-onset. The overlapping E3 events still have tendencies for a higher energy transfer from onset to 1 day after.

The intersecting percentiles in the plots indicate that E1 and E3 events can have similar solar wind driving factors. Hence, the median values suggest probable differences rather than absolute distinctions.

4.2.2 Geomagnetic response

Figure 9 adopts the same layout and time-window structure as Figure 8 but focuses on the key geomagnetic indices Dst, Kp*10, and AE. For absolute events, the geomagnetic indices Dst, Kp*10, and AE consistently show stronger peak/trough responses during E3 events compared to E1. The average minimum Dst response for the E3 events reaches 2.4 times deeper than for E1 events, emphasizing the most significant variance among the indices. The Kp*10 and AE peaks for absolute E3 events are 1.3 and 1.6 times those of E1 events, respectively. The more intense geomagnetic deflections highlight the stronger geomagnetic activity associated with absolute E3 events. On the day before onset, a pronounced divergence between the events is visible, with absolute E3 events consistently registering stronger responses. This difference continues post-onset, where Kp*10 and AE return to comparable levels about 4 days later and Dst takes even longer.

For the overlapping (middle panels) and relative (right panels) events, the differences in Kp*10 and AE converge, with E3 responses being less than 1.2 times higher with a large percentile overlap. The differences in Dst, however, remain; overlapping and relative E3 events show a minimum that is twice as strong as E1 events, with less percentile overlap compared to the other indices. Overlapping and relative E3 events tend to show stronger responses post-onset (2–4 days) across all indices and pre-onset (2–3 days) for Dst. Notably, relative E3 events also exhibit increased AE activity pre-onset compared to E1.

Although not depicted, the pressure-corrected Dst index and the RC index—derived from the Dst index and previously demonstrated to offer a more accurate portrayal of global geomagnetic variations than Dst (Olsen et al., 2014)—were also subjected to SEAs. However, the outcomes from this analysis did not reveal any notable distinctions from those obtained using Dst. Similarly, an evaluation of the substorm rate, known to correlate strongly with the AE index, did not yield additional insights when analyzed in this manner.

In examining key solar wind and geomagnetic parameters, no single parameter can distinguish between E1 and E3 events. However, distinctive patterns emerge. Dst is the only geomagnetic index showing potential for distinguishing between E1 and E3 events across all categories. This indicates that Dst might be best linked to the variations in the >292 keV flux. Stronger southward Bz orientations and heightened epsilon responses over longer times also tend to be characteristic of all types of E3 events. Only solar wind speed exhibits a distinct pattern between the overlapping/relative and absolute events.

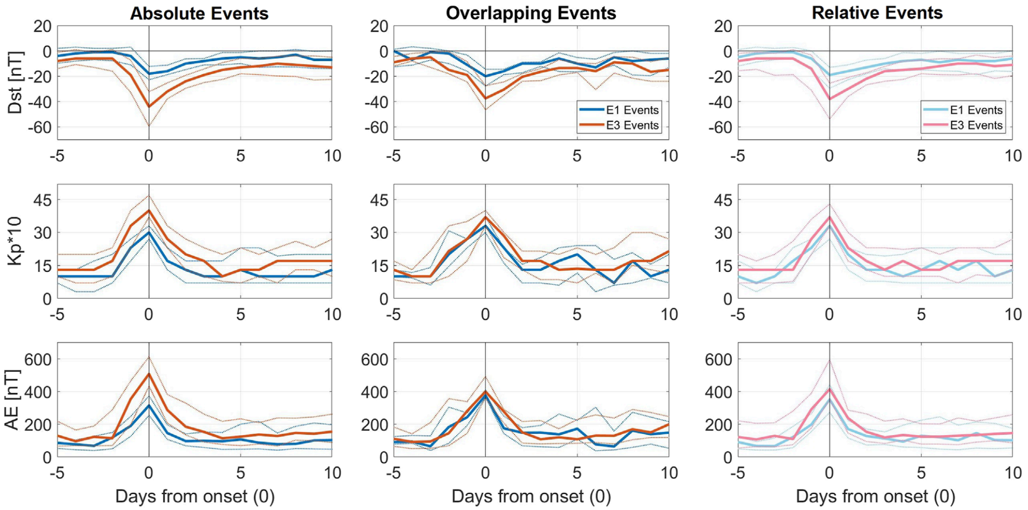

FIGURE 9
The same as in Figure 8 just for geomagnetic indices. From top to bottom, the Dst, Kp*10, and AE indices are shown.

4.3 Solar wind structure

This subsection presents SEAs of MEE fluxes, solar wind, and geomagnetic indices, including the categorization of E1 and E3 events by their specific solar wind structure, HSS, or CME. The aim is to identify whether the discrepancies between E1 and E3 events are influenced by their respective solar wind structure as listed in Table 2. Note that the respective separation results in a very weak statistic for the overlapping events. Hence, the resulting SEAs are shown only for completeness, but potential findings regarding overlapping events are disregarded in the text.

4.3.1 Flux response

Figure 10 shows the precipitating MEE fluxes as in Figure 5 but with the E1 and E3 events separated into HSSs and CMEs. In general, the difference between absolute E1 and E3 events is still prominent, as shown in the left panels of Figure 5. The HSS- (light blue) and CME-driven (blue) absolute E1 events show similar flux levels in all energy channels. The absolute E3 events, however, show visible differences where the fluxes associated with CMEs (red) are higher than those associated with HSSs (orange). The relative CME-driven E3 events have higher flux responses in all channels than HSS-driven E3 events (right panels). This includes the >43 keV channel where in Figure 5, all average flux peaks were the same.

4.3.2 Solar wind response

Figure 11 presents the same solar wind properties as in Figure 8 but with the E1 and E3 events separated into HSS- or CME-driven as in Figure 10. CME-driven events have larger Bz and epsilon deflections than their HSS-driven counterparts. An exception occurs in the solar wind speed, where the opposite is true.

The absolute events in the left panels of Figure 11 show that CME-driven absolute E1 (blue) and HSS-driven absolute E3 (orange) events have the same peak responses in Bz and epsilon, but the HSS-driven E3 events last longer with a broader peak. However, the differences between CME-driven E3 (red) and HSS-driven E1 (light blue) events are substantial for these parameters. For solar wind speed, it is the opposite. The CME-driven E1 events and HSS-driven E3 events are associated with the lowest and highest solar wind speeds, respectively. The CME-driven E3 events and HSS-driven E1 events have similar speed levels. It demonstrates that the overlapping percentiles in Figure 8 can largely be ascribed to different solar wind drivers.

The solar wind parameters for the relative E1 and E3 events in the right panels resemble the absolute events, demonstrating that it is the CME-driven E1 events and HSS-driven E3 events that are responsible for the overlap between the event types in Bz and epsilon. For all solar wind parameters, the HSS-driven E1 and E3 events converge, giving the weakest responses in Bz and epsilon and the strongest in solar wind speed. Delayed or prolonged solar wind speeds following onset are evident for both the CME- and HSS-driven relative E3 events.

4.3.3 Geomagnetic response

In Figure 12, the geomagnetic indices are portrayed in the same manner as in Figure 9, and the events are separated into solar wind drivers as in Figures 10, 11.

The absolute events in the left panels of Figure 12 show that Dst has clear structure-dependent variations. CME-driven E1 (blue) and HSS-driven E3 (orange) events have similar Dst troughs, but the HSS-driven E3 events show a longer recovery time. The largest differences are between CME-driven E3 (red) and HSS-driven E1 (light blue) events. Kp*10 and AE show no

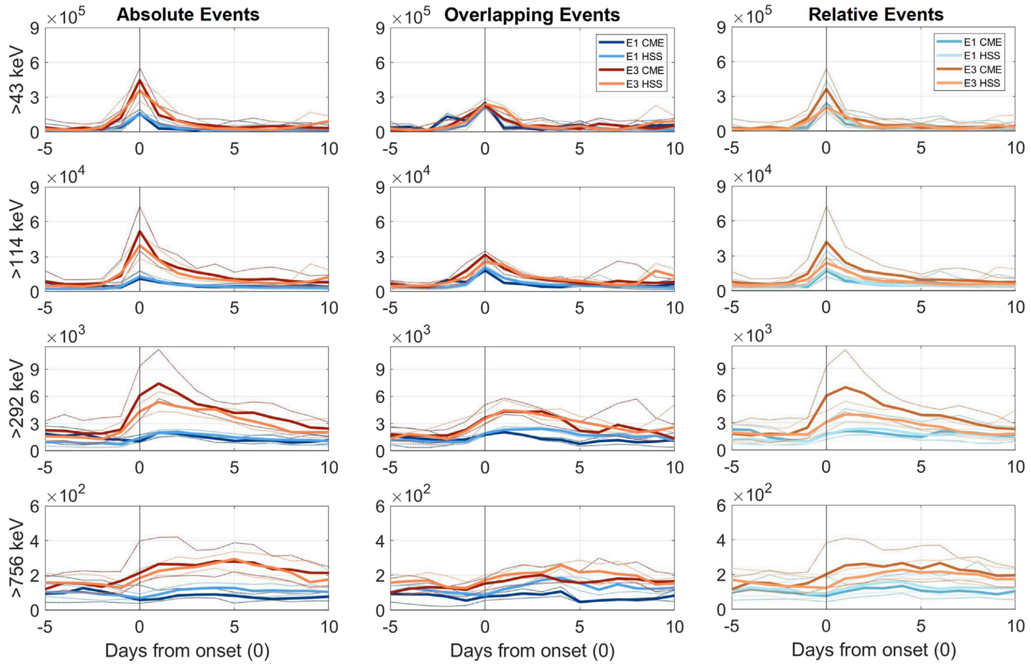

FIGURE 10
The same as Figure 5 but with events separated into solar wind drivers. For the absolute and overlapping E1 and E3 events, CMEs are in blue and red, and HSSs are in light blue and orange, respectively. Relative events are in similar offset colors. Note that the >292 keV flux channel is on a different scale than in Figure 5.

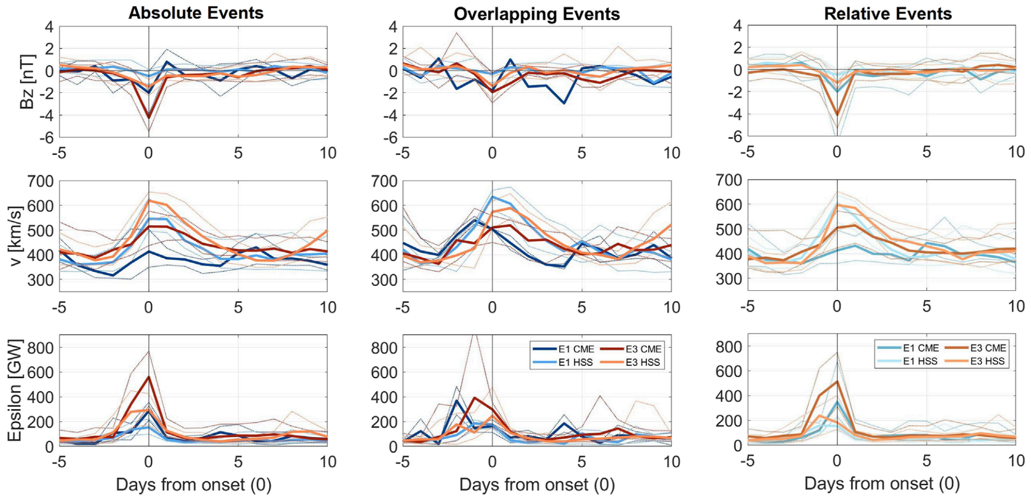

FIGURE 11
The same as Figure 8 but with E1 and E3 events separated into solar wind drivers as in Figure 10. Note that Bz and Epsilon are on a different scale than in Figure 8.

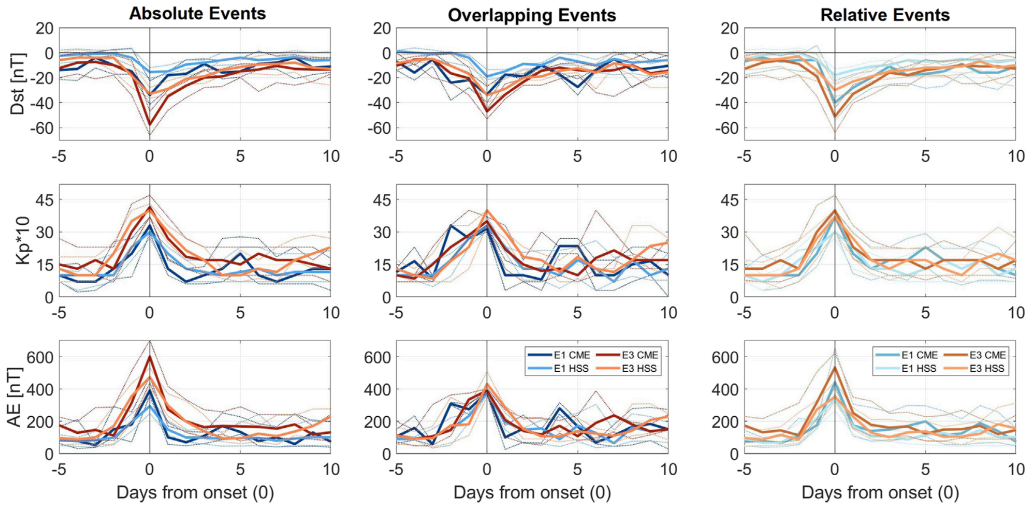

FIGURE 12
The same as in Figure 9 separated into solar wind drivers in the same way as in Figures 10, 11.

dependency on structure, with the absolute E3 events having stronger responses than E1 events independent of the solar wind driver. However, tendencies for stronger and sharper responses for the CME-driven events compared to the HSS-driven ones are evident.

The relative events in the right panels of Figure 12 show that the CME-driven E1 and E3 events tend to have stronger responses than the HSS-driven ones in Dst and AE. In Kp*10, all but the HSS-driven E1 events show the same peak response.

In summary, as shown in Figures 8, 9, there is a significant overlap between the percentiles of E1 and E3 events. Based on the findings in Figures 11, 12, some of this percentile overlap can be ascribed to solar wind structures, as a clearer separation of E1 and E3 events is possible if the solar wind structure is known. The Dst index especially exhibits pronounced structure-dependent variations among E1 and E3 events. It suggests that knowing the underlying solar wind structure is crucial for establishing specific thresholds for the occurrence of E3 events.

4.4 Predictive probabilities of absolute events

The absolute events allow a general assessment of which geomagnetic deflections or solar wind parameters are associated with high and low >292 keV fluxes. This subsection explores the predictive probability of the solar wind parameters and geomagnetic indices with respect to the occurrence of absolute E1 or E3 events, as depicted in the top panels of Figure 13. These panels illustrate the occurrence probabilities for the 55 absolute E1 events (blue) and the 55 absolute E3 events (red) based on the largest daily average values of epsilon, Dst, and Kp*10, observed from 2 days before to 2 days after the event onset. Moreover, the probabilities for events driven by CMEs and HSSs are shown with dashed lines in darker and lighter shades of the corresponding colors, respectively. The bottom panels of the figure present the number of events included in each bin. For the epsilon parameter, the bins are segmented in 200 GW increments, ranging from 0 to 4,600 GW. It is important to note that the plot does not include three E3 events with peak epsilon values of 1,900, 2,700, and 4,500 GW, as the *x*-axis extends only up to 1,700 GW. For Dst and Kp*10, the bins are set at intervals of 10 nT and 5, with ranges from −110 to 0 nT and 20 to 75, respectively.

The three panels of Figure 13 identify distinct thresholds at which the probability of absolute E1 or E3 event diverges. For epsilon, Dst, and Kp*10, this divergence occurs at approximately 400 GW, −30 nT, and 35, respectively. Beyond these points, the likelihood of an E3 event increases with greater geomagnetic activity and the likelihood of an E1 event with weaker. Furthermore, there are specific value ranges where the analysis guarantees or excludes an event with >95% probability: epsilon values below 200 GW, Dst values above −20 nT, and Kp*10 values below 30 will almost certainly correspond to an E1 event, while for an E3 event, the corresponding thresholds are epsilon values above 700 GW, Dst below −50 nT, and Kp*10 above 40. For epsilon, Dst, and Kp*10, 36%, 52%, and 55% of the events are within these high-probability ranges, respectively. The events not included in these ranges vary slightly for the different parameters. Hence, applying more than one index could lead to fewer events falling in the high-uncertainty region.

When analyzing the events sorted by their solar wind drivers, as indicated by the dashed lines, the divergence threshold in Dst exhibits notable variation. For events driven by HSSs, the threshold slightly shifts, only a few nT above the non-separated event threshold. In contrast, for CME-driven events, the divergence threshold shifts to around −40 nT, presenting a 10 nT discrepancy

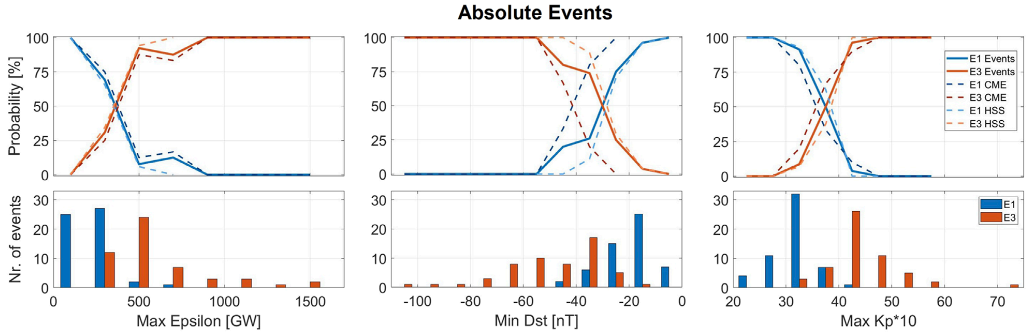

FIGURE 13
Probability of absolute E1 (blue) and E3 (red) event occurrence based on the largest daily average values of epsilon, Dst, and Kp*10 (top panels). Events driven by CMEs and HSSs are differentiated with dashed lines in darker and lighter corresponding colors, respectively. The lower panels show the distribution of events within each bin.

from the combined event analysis. Furthermore, with the solar wind structure known, Dst can, with >95% certainty, account for up to 65% of the 110 absolute events. If CME-driven, the high probability threshold shifts from −50 to −45 nT, and if HSS-driven, it shifts from −20 to −25 nT. In the case of epsilon and Kp*10, however, a clear separation based on different solar wind structures is not as evident.

The Bz, v, and AE parameters were subjected to the same probabilistic analysis as in Figure 13. Bz did not yield significant insights, as its short range of daily averaged values could not meaningfully differentiate between E1 and E3 events. AE demonstrated trends similar to Kp*10 but with a larger range of values that could correspond to both E1 and E3 events. The solar wind speed presented a broad spectrum of values that could correspond to both events, indicating significant overlap. Notably, the distinction between solar wind drivers increased the prediction quality but was not comparable to the shown parameters epsilon, Dst, and Kp.

This subsection investigated the occurrence probability of absolute E1 and E3 events, revealing that for peak values of epsilon, Dst, and Kp*10, there are thresholds in which one becomes more likely than the other. Additionally, there are specific threshold values that can almost ensure the classification of E1 or E3 events. Based on the 110 absolute events, 36% for epsilon, 52% for Dst, and 55% for Kp*10 are within this high probability range. However, when solar wind structure is considered, Dst is the only index that increases its accuracy to include 65% of events in the high probability range.

5 Discussion

The overarching objective of this study is to unravel the characteristics of solar wind properties and geomagnetic indices associated with the high-energy tail of MEE precipitation, enabling a better parameterization of the full energy range of EEP. This implies a parameterization that can determine the true range of flux variability, not averaging out strong events as demonstrated in Nesse Tyssøy et al. (2022) and Sinnhuber et al. (2022). Such parameterization will allow for an understanding of the importance of EEP's direct effect on the lower mesosphere and upper stratosphere chemistry, which further affects both the strength and timing of the subsequent impact on atmospheric dynamics.

From the 164 flux peaks exceeding the 90th percentile of the >43 keV flux, absolute and relative E1 and E3 events are defined based on the absolute >292 keV flux and the ratio of >292 keV and >43 keV fluxes, respectively. The absolute events allow a general assessment of which geomagnetic deflections or solar wind parameters are associated with high and low >292 keV fluxes. Moreover, the relative events allow for the investigation of favorable conditions for enhanced >292 keV fluxes, independent of the >43 keV response. The latter also applies to the subset of absolute events with overlapping >43 keV fluxes. These distinctions are further established through SEAs of NO observations, confirming both direct and indirect effects on NO density, with a notable direct impact in the lower mesosphere predominantly associated with absolute E3 events (see Figure 7).

5.1 Energy transfer from the solar wind to the magnetosphere

The solar wind fuels the energy driving the magnetospheric processes that increase the population of high-energy tail electrons ($\gtrsim 300$ keV) and subsequently scatter them into the loss cone. A southward IMF (negative Bz) induces a large-scale electric field that transports electrons from the magnetotail into the inner magnetosphere, where they become part of the electron source population in the plasmasheet. Fast solar wind speed has been considered one of the most important predictors for transporting fluxes of the electron source population from the plasmasheet to the radiation belt region, trapping $\gtrsim 300$ keV electrons in the inner magnetosphere (Katsavrias et al., 2021; Stepanov et al., 2021). Combined, Bz and solar wind speed can be used to estimate the bulk energy transfer from the solar wind into the magnetosphere via dayside reconnection rate by applying coupling functions such as the widely used epsilon parameter by Akasofu (1981).

Figure 8 confirms that all three types of E3 events tend to have a stronger southward IMF component and stronger energy transfer into the magnetosphere compared to E1 events. How much energy is required to guarantee an absolute E3 event is, however, more uncertain. Figure 13 shows that for epsilon peak values above 700 GW and below 200 GW, there is >95% probability of an E3 and E1 event, respectively. These thresholds result in an uncertainty range of 500 GW, encompassing 64% of the identified events. Salice et al. (2023) explored the same daily precipitation fluxes in the NH and found that the epsilon coupling function accumulated over 4 days correlates well (0.84) with the >292 keV peak flux. Figure 4 in Salice et al. (2023) shows, however, that the spread in potential flux responses is typically about an order of magnitude, consistent with the wide band of epsilon values corresponding to absolute E1 and E3 events.

Moreover, the overlapping and relative events where similar levels of >43 keV fluxes result in very different high-energy tail fluxes confirm that neither Bz, solar wind speed, nor epsilon alone can predict the occurrence of high-energy tail precipitation. Figure 8 shows that solar wind speed tends to be similar for E1 and E3 events. However, the elevated (>500 km/s) plateau in the solar wind speed for overlapping and relative E3 events starts at the onset, 1 day after that of E1 events, and declines slower, implying higher speeds in the recovery phase of the storm. Figure 11 shows that E1 and E3 events driven by CMEs, in general, are associated with lower speed compared to E1 and E3 events driven by HSSs. However, for relative events, both CME- and HSS-driven E3 events show high speeds 1 day after onset with a gradual recovery. This suggests that the timing and/or duration of elevated solar wind speed is a potential factor for driving the high-energy tail of MEE precipitation by providing a persistent magnetospheric acceleration mechanism after the flux rise of the $\gtrsim$ 30 keV electron source population.

5.2 Magnetospheric energy dissipation

The energy transfer to the magnetosphere from the solar wind is dissipated into three main sinks: Joule heating, auroral particle precipitation, and ring current injection (e.g., Tenfjord and Østgaard, 2013). The magnetospheric energy loss to Joule heating and auroral particle precipitation typically occurs in the main phase of a strong geomagnetic disturbance, while the ring current energy is “temporarily stored” in the magnetosphere. Assuming that the AE index represents energy dissipation of Joule heating and auroral particle precipitation and the Dst index the ring current growth, Figure 9 confirms that more energy is dissipated into the ring current during E3 events, compared to E1 events. In fact, for relative and overlapping events, the AE and Kp*10 values converge while the Dst remains notably deflected for E3 events compared to E1 events. This suggests a larger build-up of ring current particles associated with both absolute and relative E3 events.

The subsequent decay of the ring current is caused by several particle loss processes, such as scattering by Coulomb collisions, charge exchange, wave-particle interactions, and convection transporting the ions across the magnetopause (Søraas et al., 2004). The ring current decay begins when Bz turns less southward as the large-scale convection electric field will no longer transport particles to the inner magnetosphere (Jaynes et al., 2015). This is clear in the SEAs shown for Bz and Dst in Figures 8, 9, respectively. After the typical fast initial decay, the decay becomes more gradual depending on the charge exchange between the ring current ions and the geocorona as well as wave-particle interaction at or near the plasmapause forcing particles into the atmospheric loss cone (Søraas et al., 1999). The loss processes result in a ring current decay time of about 7–10 h (Søraas et al., 2004).

Based on Figure 6, the >292 keV flux peak typically occurs one and 2 days after the zero epoch. This delay corresponds to the strongest positive gradient of Dst after its deep minima on the zero epoch day. As such, there might be a physical link between the Dst recovery phase and MEE precipitation, including the high-energy tail. This would, however, require elevated substorm occurrence rates in the storm recovery phase to generate chorus waves that will scatter the ring current electrons into the loss cone. The respective chorus waves will simultaneously be responsible for electron loss in the MEE range in the radiation belts. Notably, Newell et al. (2016) demonstrated a close link between substorm probabilities and solar wind speed, reinforcing the earlier suggestion that elevated solar wind speeds in the recovery phase of a storm contribute to high >292 keV fluxes.

The Auroral Electrojet (AE) index is also found to be well correlated to the substorm occurrence rate on a daily scale (Tyssøy et al., 2021). From the SEA in Figure 9, all three categories of E3 events are associated with a higher AE response in the recovery phase of the Dst than E1 events. A higher substorm onset rate for E3 events is confirmed by examining the daily average from the substorm list provided by the number of substorms per day based on Newell and Gjerloev (2011). There is, however, not a significant difference across all categories of events. Tyssøy et al. (2021) created an AE-based MEE proxy by accumulating the AE activity over multiple days, including terms counting for the associated lifetimes. The results showed that AE-based proxies can predict at least 70% of the observed MEE precipitation variance at all energies. Applying the AE-based model to our events does capture the general features of our SEA flux analysis. It is, however, not able to identify the individual E3 events. Hence, a higher substorm onset rate in the recovery phase alone does not appear to be exclusively able to explain the high-energy tail of MEE precipitation found for E3 events.

Kp has been found to correlate well with >30 keV EEP and is commonly used in models due to its availability and long existence, e.g., as in van de Kamp et al. (2016), van de Kamp et al. (2018)’s model. The probability assessment presented in Figure 13 revealed Kp*10 as one of the best parameters independent of the solar structure as it can exclude or guarantee 55% of absolute E1 and E3 events. However, as shown in Figures 9, 12, Kp*10 is less effective in differentiating between overlapping and relative E1 and E3 events with similar >43 keV peak fluxes.

5.3 Probability assessment

Figure 13 reveals the effectiveness of Dst in predicting up to 65% of events when the solar wind structure is considered. It has long been known that Dst has different characteristics for HSSs and CMEs (Borovsky and Steinberg, 2006). For CME-driven events, E1 or E3 events can be determined or excluded with 95% probability above −25 and below −50 nT. For HSS-driven events, these thresholds are above −20 and below −45 nT. The latter nominates the Dst index to most accurately predict if a specific geomagnetic disturbance will lead to a large MEE precipitation response in the >292 keV channel. If combined with consideration of the timing and/or duration of elevated solar wind speed in the recovery phase of the storms, there is a potential for even better prediction capabilities and an understanding of the physical mechanisms responsible for the high-energy tail of the MEE precipitation in the atmosphere. To fully examine if a specific storm will generate high-energy MEE precipitation requires case studies, which is beyond the scope of the current paper.

6 Conclusion

The overarching objective of this study is to explore and better understand the high-energy tail of MEE precipitation in the context of solar wind properties and geomagnetic responses. The research contributes to refining EEP parameterization by offering insights into the high-energy tail that can be used to improve the accuracy of the full energy range of EEP parameterization in chemistry-climate models. The electron flux data is retrieved from MEPED aboard the POES/Metop satellite series over an entire solar cycle from 2004 to 2014.164 peaks in the >43 keV electron flux exceeding the 90th percentile are categorized into absolute, overlapping, and relative E1 and E3 events. This selection of events allows for a concentrated study on intense electron flux occurrences, addressing a gap in current understanding and limitations.

Of the 164 peaks, absolute E1 and E3 events are defined by the third highest and lowest peaks in the >292 keV flux, respectively. Overlapping events, sharing similar >43 keV peak responses, were also identified, though their low number necessitates cautious interpretation. Moreover, relative E1 and E3 events are defined as the third with the lowest and highest ratio between >292 keV and >43 keV flux peaks, respectively. Overlapping and relative events provide insight into which conditions generate a high-energy tail independent of the initial $\gtrsim$ 30 keV flux level. Observations of the NO density estimated from the SOFIE instrument on board the AIM satellite confirm that absolute E3 events will directly impact the lower mesosphere, which motivates the need to parameterize the full range of EEP.

Based on our SEAs, no single solar wind nor geomagnetic parameter captures the differences between E1 and E3 events across the absolute, overlapping, and relative categories. However, tendencies are visible, allowing us to suggest the following hypothesis.

The high-energy tail ($\gtrsim$ 300 keV) of electron precipitation requires an increased source population ($\gtrsim$ 30 keV) in the main phase of the storm. These $\gtrsim$ 30 keV electrons will first be accelerated and then precipitate into the atmosphere or contribute to the ring current and radiation belt populations. A sustained elevation in solar wind speed during the recovery phase of a storm increases the substorm onset rate, which ensures electron acceleration to high energies and subsequent scattering into the loss cone from both the ring current and radiation belts. Hence, overlapping and relative E3 events are likely associated with elevated solar wind speeds persisting in the recovery phase of a deep Dst trough. The magnetospheric processes that accelerate and scatter electrons in the recovery phase of a storm further explain the delay often found in the >292 keV peak compared to the >43 keV peak.

As single predictors for absolute E1 or E3 events, epsilon is the best solar wind parameter, and Dst and Kp*10 are the best geomagnetic indices. Each of the three variables has a specific threshold where the probability of an E3 (E1) event becomes more likely with increasing (decreasing) activity. For epsilon, Dst, and Kp*10, the thresholds are at 400 GW, −30 nT, and 35,respectively.

Furthermore, Dst and Kp*10 have defined thresholds where the probability of either an absolute E1 or E3 event occurring is >95%, accounting for over half of the events. Specifically, 52% of absolute events fall within this high-probability range for Dst and 55% for Kp*10. The thresholds for an E1 event are for Dst values above −20 nT and Kp*10 values below 30. For E3 events they are for Dst values below −50 nT and Kp*10 values above 40.

Solar wind speed and the Dst index exhibit pronounced structure-dependent variations compared to other parameters. Knowledge of the solar wind structure confines the high probability limits, increasing Dst's predictive accuracy to 65%. The 35% of events within the ambiguous range of Dst values might be determined by examining solar wind speed. Future studies will focus on case studies to explore the high-energy tail response in relation to elevated solar wind speed and the Dst recovery phase.

Data availability statement

The original contributions presented in the study are included in the article/Supplementary Material, further inquiries can be directed to the corresponding author. The NOAA/POES MEPED data used in this study are available from the National Oceanic and Atmospheric Administration (https://www.ngdc.noaa.gov/stp/satellite/poes/dataaccess.html). The bounce loss cone fluxes used in this study are available at Zenodo via https://doi.org/10.5281/zenodo.6590387. Geomagnetic indices and solar wind parameters were obtained from NASA Omniweb at https://omniweb.gsfc.nasa.gov/form/dx1.html. We gratefully acknowledge the SuperMAG collaborators (https://supermag.jhuapl.edu/info/?page=acknowledgement) where the epsilon parameter was downloaded. The AIM-SOFIE data (version 1.2) are found online at https://sofie.gats-inc.com/getdata.

Author contributions

JS: Writing–original draft, Writing–review and editing. HN: Supervision, Writing–original draft, Writing–review and editing. NP: Writing–review and editing. EK: Writing–review and editing. AK: Writing–review and editing. MD: Writing–review and editing. EB: Writing–review and editing. CS-J: Writing–review and editing.

Funding

The author(s) declare that financial support was received for the research, authorship, and/or publication of this article. The study is supported by the Norwegian Research Council (NRC) under contracts 223252 and 302040.

Acknowledgments

HN further acknowledges the Young CAS (Centre for Advanced Studies) fellow program. EK acknowledges the Finnish Centre of Excellence in Research of Sustainable Space, Project 1336807, for supporting this research. The authors thank NOAA for providing the MEPED data, OMNIWeb for solar wind and geomagnetic data, and the AIM mission for providing SOFIE data. The authors thank Ian G. Richardson for providing the list of solar wind classifications.

Conflict of interest

The authors declare that the research was conducted in the absence of any commercial or financial relationships that could be construed as a potential conflict of interest.

Publisher's note

Supplementary material

The Supplementary Material for this article can be found online at: https://www.frontiersin.org/articles/10.3389/fspas.2024.1352020/full#supplementary-material

SUPPLEMENTARY TABLE S1

Overview of the dates for the >43 keV peaks for absolute (left-hand side) and relative (right-hand side) E1 and E3 events. '*' indicates the subset of absolute events that are also overlapping events. Purple dates indicate that the event is CME-driven, while those without color are HSS-driven. The events marked with a "!" are not associated with a solar wind structure. Bold dates, both black and purple, show the events that are both in the absolute data set and in the relative data set. Dates that are in both datasets but in different categories, e.g., absolute E1 and relative E3 or absolute E3 and relative E1, are bold and italic.

References

Akasofu, S. I. (1981). Energy coupling between the solar wind and the magnetosphere. *Space Sci. Rev.* 28. doi:10.1007/BF00218810

Angelopoulos, V., Zhang, X.-J., Artemyev, A. V., Mourenas, D., Tsai, E., Wilkins, C., et al. (2023). Th: energetic electron precipitation driven by electromagnetic ion cyclotron waves from ELFIN's low altitude perspective. *Space Sci. Rev.* 219, 37. doi:10.1007/s11214-023-00984-w

Asikainen, T., and Ruopsa, M. (2016). Solar wind drivers of energetic electron precipitation. *J. Geophys. Res. Space Phys.* 121, 2209–2225. doi:10.1002/2015JA022215

Babu, E. M., Nesse, H., Hatch, S. M., Olsen, N., Salice, J. A., and Richardson, I. G. (2023). An updated geomagnetic index-based model for determining the latitudinal extent of energetic electron precipitation. *J. Geophys. Res. Space Phys.* 128. doi:10.1029/2023JA031371

Babu, E. M., Tyssøy, H. N., Smith-Johnsen, C., Maliniemi, V., Salice, J. A., Millan, R. M., et al. (2022). Determining latitudinal extent of energetic electron precipitation using MEPED on-board NOAA/POES. *J. Geophys. Res. Space Phys.* 127. doi:10.1029/2022JA030489

Baldwin, M. P., and Dunkerton, T. J. (2001). Stratospheric harbingers of anomalous weather regimes. *Science* 294, 581–584. doi:10.1126/science.1063315

Beharrell, M. J., Honary, F., Rodger, C. J., and Clilverd, M. A. (2015). Substorm-induced energetic electron precipitation: morphology and prediction. *J. Geophys. Res. Space Phys.* 120, 2993–3008. doi:10.1002/2014JA020632

Borovsky, J. E., and Steinberg, J. T. (2006). The "calm before the storm" in CIR/magnetosphere interactions: occurrence statistics, solar wind statistics, and magnetospheric preconditioning. *J. Geophys. Res. Space Phys.* 111. doi:10.1029/2005JA011397

Clilverd, M. A., Seppälä, A., Rodger, C. J., Mlynczak, M. G., and Kozyra, J. U. (2009). Additional stratospheric NO_x production by relativistic electron precipitation during the 2004 spring NO_x descent event. *J. Geophys. Res. Space Phys.* 114. doi:10.1029/2008JA013472

Daae, M., Espy, P., Nesse Tyssøy, H., Newnham, D., Stadsnes, J., and Søraas, F. (2012). The effect of energetic electron precipitation on middle mesospheric night-time ozone during and after a moderate geomagnetic storm. *Geophys. Res. Lett.* 39. doi:10.1029/2012GL053787

Damiani, A., Funke, B., López Puertas, M., Santee, M. L., Cordero, R. R., and Watanabe, S. (2016). Energetic particle precipitation: a major driver of the ozone budget in the Antarctic upper stratosphere. *Geophys. Res. Lett.* 43, 3554–3562. doi:10.1002/2016GL068279

Duderstadt, K. A., Huang, C.-L., Spence, H. E., Smith, S., Blake, J. B., Crew, A. B., et al. (2021). Estimating the impacts of radiation belt electrons on atmospheric chemistry using FIREBIRD II and van allen probes observations. *J. Geophys. Res. Atmos.* 126. doi:10.1029/2020JD033098

Evans, D. S., and Greer, M. S. (2004). *Polar orbiting environmental satellite Space environment monitor - 2: instrument descriptions and archive data documentation, NOAA technical memorandum version 1.4.*

Funke, B., Baumgaertner, A., Calisto, M., Egorova, T., Jackman, C. H., Kieser, J., et al. (2011). Composition changes after the Halloween solar proton event: the High Energy Particle Precipitation in the Atmosphere (HEPPA) model versus MIPAS data intercomparison study. *Atmos. Chem. Phys.* 11, 9089–9139. doi:10.5194/acp-11-9089-2011

Funke, B., Dudok de Wit, T., Ermolli, I., Haberreiter, M., Kinnison, D., Marsh, D., et al. (2023). Towards the definition of a solar forcing dataset for CMIP7. *Geosci. Model Dev. Discuss.* 2023, 1–14. doi:10.5194/gmd-2023-100

Gjerloev, J. W. (2012). The SuperMAG data processing technique. *J. Geophys. Res.* 117. doi:10.1029/2012JA017683

Gómez-Ramírez, D., McNabb, J. W. C., Russell, J. M., Hervig, M. E., Deaver, L. E., Paxton, G., et al. (2013). Empirical correction of thermal responses in the Solar Occultation for Ice Experiment nitric oxide measurements and initial data validation results. *Appl. Opt.* 52, 2950–2959. doi:10.1364/AO.52.002950

Gordley, L. L., Hervig, M. E., Fish, C., Russell, J. M., Bailey, S., Cook, J., et al. (2009). The solar occultation for ice experiment. *J. Atmos. Solar-Terrestrial Phys.* 71, 300–315. doi:10.1016/j.jastp.2008.07.012

Hendrickx, K., Megner, L., Gumbel, J., Siskind, D. E., Orsolini, Y. J., Tyssøy, H. N., et al. (2015). Observation of 27-day solar cycles in the production and mesospheric descent of EPP-produced NO. *J. Geophys. Res. Space Phys.* 120, 8978–8988. doi:10.1002/2015JA021441

Jackman, C. H., DeLand, M. T., Labow, G. J., Fleming, E. L., Weisenstein, D. K., Ko, M. K. W., et al. (2005). Neutral atmospheric influences of the solar proton events in October–November 2003. *J. Geophys. Res. Space Phys.* 110. doi:10.1029/2004JA010888

Jaynes, A. N., Baker, D. N., Singer, H. J., Rodriguez, J. V., Loto'aniu, T. M., Ali, A. F., et al. (2015). Source and seed populations for relativistic electrons: their roles in radiation belt changes. *J. Geophys. Res. Space Phys.* 120, 7240–7254. doi:10.1002/2015JA021234

Katsavrias, C., Aminalragia–Giamini, S., Papadimitriou, C., Sandberg, I., Jiggens, P., Daglis, I., et al. (2021). On the interplanetary parameter schemes which drive the variability of the source/seed electron population at GEO. *J. Geophys. Res. Space Phys.* 126, e2020JA028939. doi:10.1029/2020JA028939

Kennel, C. F., and Petschek, H. E. (1966). Limit on stably trapped particle fluxes. *J. Geophys. Res.* 71, 1–28. doi:10.1029/JZ071i001p00001

Khazanov, G. V., and Glocer, A. (2020). How magnetically conjugate atmospheres and the magnetosphere participate in the formation of low-energy electron precipitation in the region of diffuse aurora. *J. Geophys. Res. Space Phys.* 125, e2020JA028057. doi:10.1029/2020JA028057

Kilpua, E., Koskinen, H. E. J., and Pulkkinen, T. I. (2017). Coronal mass ejections and their sheath regions in interplanetary space. *Living Rev. Sol. Phys.* 14, 5. doi:10.1007/s41116-017-0009-6

Kirkwood, S., Osepian, A., Belova, E., Urban, J., Pérot, K., and Sinha, A. K. (2015). Ionization and NO production in the polar mesosphere during high-speed solar wind streams: model validation and comparison with NO enhancements observed by Odin-SMR. *Ann. Geophys.* 33, 561–572. doi:10.5194/angeo-33-561-2015

Koskinen, H. E. J., and Tanskanen, E. I. (2002). Magnetospheric energy budget and the epsilon parameter. *J. Geophys. Res. Space Phys.* 107. doi:10.1029/2002JA009283

Li, W., and Hudson, M. (2019). Earth's van allen radiation belts: from discovery to the van allen probes era. *J. Geophys. Res. Space Phys.* 124, 8319–8351. doi:10.1029/2018JA025940

Maliniemi, V., Asikainen, T., and Mursula, K. (2016). Effect of geomagnetic activity on the northern annular mode: QBO dependence and the Holton-Tan relationship. *J. Geophys. Res. Atmos.* 121, 10,043–10,055. doi:10.1002/2015JD024460

Maliniemi, V., Nesse Tyssøy, H., Smith-Johnsen, C., Arsenovic, P., and Marsh, D. R. (2021). Effects of enhanced downwelling of NO_x on Antarctic upper-stratospheric ozone in the 21st century. *Atmos. Chem. Phys.* 21, 11041–11052. doi:10.5194/acp-21-11041-2021

Marsh, D. R., Solomon, S. C., and Reynolds, A. E. (2004). Empirical model of nitric oxide in the lower thermosphere. *J. Geophys. Res. Space Phys.* 109. doi:10.1029/2003JA010199

Matthes, K., Funke, B., Andersson, M. E., Barnard, L., Beer, J., Charbonneau, P., et al. (2017). Solar forcing for CMIP6 (v3.2). *Geosci. Model Dev.* 10, 2247–2302. doi:10.5194/gmd-10-2247-2017

Mironova, I. A., Artamonov, A. A., Bazilevskaya, G. A., Rozanov, E. V., Kovaltsov, G. A., Makhmutov, V. S., et al. (2019). Ionization of the polar atmosphere by energetic electron precipitation retrieved from balloon measurements. *Geophys. Res. Lett.* 46, 990–996. doi:10.1029/2018GL079421

Nesse, H., Babu, E. M., Salice, J. A., and Funke, B. (2023). Energetic electron precipitation during slot region filling events. *J. Geophys. Res. Space Phys.* 128, e2023JA031606. doi:10.1029/2023JA031606

Nesse Tyssøy, H., Sandanger, M. I., Ødegaard, L.-K. G., Stadsnes, J., Aasnes, A., and Zawedde, A. E. (2016). Energetic electron precipitation into the middle atmosphere—constructing the loss cone fluxes from MEPED POES. *J. Geophys. Res. Space Phys.* 121, 5693–5707. doi:10.1002/2016JA022752

Nesse Tyssøy, H., Sinnhuber, M., Asikainen, T., Bender, S., Clilverd, M. A., Funke, B., et al. (2022). HEPPA III intercomparison experiment on electron precipitation impacts: 1. Estimated ionization rates during a geomagnetic active period in april 2010. *J. Geophys. Res. Space Phys.* 127, e2021JA029128. doi:10.1029/2021JA029128

Nesse Tyssøy, H., and Stadsnes, J. (2015). Cutoff latitude variation during solar proton events: causes and consequences. *J. Geophys. Res. Space Phys.* 120, 553–563. doi:10.1002/2014JA020508

Nesse Tyssøy, H., Stadsnes, J., Søraas, F., and Sørbø, M. (2013). Variations in cutoff latitude during the January 2012 solar proton event and implication for the distribution of particle energy deposition. *Geophys. Res. Lett.* 40, 4149–4153. doi:10.1002/grl.50815

Newell, P., Liou, K., Gjerloev, J., Sotirelis, T., Wing, S., and Mitchell, E. (2016). Substorm probabilities are best predicted from solar wind speed. *J. Atmos. Solar-Terrestrial Phys.* 146, 28–37. doi:10.1016/j.jastp.2016.04.019

Newell, P. T., and Gjerloev, J. W. (2011). Evaluation of SuperMAG auroral electrojet indices as indicators of substorms and auroral power. *J. Geophys. Res. Space Phys.* 116, A12211. doi:10.1029/2011JA016779

Newell, P. T., Ruohoniemi, J. M., and Meng, C.-I. (2004). Maps of precipitation by source region, binned by IMF, with inertial convection streamlines. *J. Geophys. Res. Space Phys.* 109. doi:10.1029/2004JA010499

Newnham, D. A., Espy, P. J., Clilverd, M. A., Rodger, C. J., Seppälä, A., Maxfield, D. J., et al. (2011). Direct observations of nitric oxide produced by energetic electron precipitation into the Antarctic middle atmosphere. *Geophys. Res. Lett.* 38. doi:10.1029/2011GL048666

Ødegaard, L.-K. G., Tyssøy, H. N., Sandanger, M. I. J., Stadsnes, J., and Søraas, F. (2016). Space Weather impact on the degradation of NOAA POES MEPED proton detectors. *J. Space Weather Space Clim.* 6, A26. doi:10.1051/swsc/2016020

Ødegaard, L.-K. G., Tyssøy, H. N., Søraas, F., Stadsnes, J., and Sandanger, M. I. (2017). Energetic electron precipitation in weak to moderate corotating interaction region-driven storms. *J. Geophys. Res. Space Phys.* 122, 2900–2921. doi:10.1002/2016JA023096

Olsen, N., Lühr, H., Finlay, C. C., Sabaka, T. J., Michaelis, I., Rauberg, J., et al. (2014). The CHAOS-4 geomagnetic field model. *Geophys. J. Int.* 197, 815–827. doi:10.1093/gji/ggu033

Ozaki, M., Shiokawa, K., Kataoka, R., Mlynczak, M., Paxton, L., Connors, M., et al. (2022). Localized mesospheric ozone destruction corresponding to isolated proton aurora coming from Earth's radiation belt. *Nature* 12, 16300. doi:10.1038/s41598-022-20548-2

Partamies, N., Tesema, F., Bland, E., Heino, E., Nesse Tyssøy, H., and Kallelid, E. (2021). Electron precipitation characteristics during isolated, compound, and multi-night substorm events. *Ann. Geophys.* 39, 69–83. doi:10.5194/angeo-39-69-2021

Pettit, J., Elliott, S., Randall, C., Halford, A., Jaynes, A., and Garcia-Sage, K. (2023). Investigation of the drivers and atmospheric impacts of energetic electron precipitation. *Front. Astronomy Space Sci.* 10. doi:10.3389/fspas.2023.1162564

Pettit, J. M., Randall, C. E., Peck, E. D., Marsh, D. R., van de Kamp, M., Fang, X., et al. (2019). Atmospheric effects of >30-keV energetic electron precipitation in the southern hemisphere winter during 2003. *J. Geophys. Res. Space Phys.* 124, 8138–8153. doi:10.1029/2019JA026868

Randall, C. E., Harvey, V. L., Holt, L. A., Marsh, D. R., Kinnison, D., Funke, B., et al. (2015). Simulation of energetic particle precipitation effects during the 2003–2004 Arctic winter. *J. Geophys. Res. Space Phys.* 120, 5035–5048. doi:10.1002/2015JA021196

Randall, C. E., Harvey, V. L., Singleton, C. S., Bailey, S. M., Bernath, P. F., Codrescu, M., et al. (2007). Energetic particle precipitation effects on the Southern Hemisphere stratosphere in 1992–2005. *J. Geophys. Res. Atmos.* 112. doi:10.1029/2006JD007696

Richardson, I. G., and Cane, H. V. (2012). Near-Earth solar wind flows and related geomagnetic activity during more than four solar cycles (1963-2011). *J. Space Weather Space Clim.* 2, A02. doi:10.1051/swsc/2012003

Rodger, C. J., Clilverd, M. A., Green, J. C., and Lam, M. M. (2010). Use of POES SEM-2 observations to examine radiation belt dynamics and energetic electron precipitation into the atmosphere. *J. Geophys. Res. Space Phys.* 115. doi:10.1029/2008JA014023

Salice, J. A., Nesse, H., Babu, E. M., Smith-Johnsen, C., and Richardson, I. G. (2023). Exploring the predictability of the high-energy tail of MEE precipitation based on solar wind properties. *J. Geophys. Res. Space Phys.* 128, e2022JA031194. doi:10.1029/2022JA031194

Sandanger, M. I., Ødegaard, L.-K. G., Nesse Tyssøy, H., Stadsnes, J., Søraas, F., Oksavik, K., et al. (2015). In-flight calibration of NOAA POES proton detectors—derivation of the MEPED correction factors. *J. Geophys. Res. Space Phys.* 120, 9578–9593. doi:10.1002/2015JA021388

Selesnick, R. S., Tu, W., Yando, K., Millan, R. M., and Redmon, R. J. (2020). POES/MEPED angular response functions and the precipitating radiation belt electron flux. *J. Geophys. Res. Space Phys.* 125, e2020JA028240. doi:10.1029/2020JA028240

Seppälä, A., Clilverd, M. A., Rodger, C. J., Verronen, P. T., and Turunen, E. (2008). The effects of hard-spectra solar proton events on the middle atmosphere. *J. Geophys. Res. Space Phys.* 113. doi:10.1029/2008JA013517

Seppälä, A., Lu, H., Clilverd, M. A., and Rodger, C. J. (2013). Geomagnetic activity signatures in wintertime stratosphere wind, temperature, and wave response. *J. Geophys. Res. Atmos.* 118, 2169–2183. doi:10.1002/jgrd.50236

Seppälä, A., Randall, C. E., Clilverd, M. A., Rozanov, E., and Rodger, C. J. (2009). Geomagnetic activity and polar surface air temperature variability. *J. Geophys. Res. Space Phys.* 114. doi:10.1029/2008JA014029

Shen, Y., Artemyev, A. V., Zhang, X.-J., Zou, Y., Angelopoulos, V., Vasko, I., et al. (2023). Contribution of kinetic alfvén waves to energetic electron precipitation from the plasma sheet during a substorm. *J. Geophys. Res. Space Phys.* 128, e2023JA031350. doi:10.1029/2023JA031350

Sinnhuber, M., Funke, B., von Clarmann, T., Lopez-Puertas, M., Stiller, G. P., and Seppälä, A. (2014). Variability of NO_x in the polar middle atmosphere from October 2003 to March 2004: vertical transport vs local production by energetic particles. *Atmos. Chem. Phys.* 14, 7681–7692. doi:10.5194/acp-14-7681-2014

Sinnhuber, M., Kazeminejad, S., and Wissing, J. M. (2011). Interannual variation of $NO_x$from the lower thermosphere to the upper stratosphere in the years 1991-2005: MLT NO_xVARIATION. *J. Geophys. Res. Space Phys.* 116. doi:10.1029/2010JA015825

Sinnhuber, M., Nesse Tyssøy, H., Asikainen, T., Bender, S., Funke, B., Hendrickx, K., et al. (2022). Heppa III intercomparison experiment on electron precipitation impacts: 2. Model-measurement intercomparison of nitric oxide (NO) during a geomagnetic storm in april 2010. *J. Geophys. Res. Space Phys.* 127, e2021JA029466. doi:10.1029/2021JA029466

Sinnhuber, M., Nieder, H., and Wieters, N. (2012). Energetic particle precipitation and the chemistry of the mesosphere/lower thermosphere. *Surv. Geophys.* 33, 1281–1334. doi:10.1007/s10712-012-9201-3

Smith-Johnsen, C., Nesse Tyssøy, H., Hendrickx, K., Orsolini, Y., Kishore Kumar, G., Ødegaard, L.-K. G., et al. (2017). Direct and indirect electron precipitation effect on nitric oxide in the polar middle atmosphere, using a full-range energy spectrum. *J. Geophys. Res. Space Phys.* 122, 8679–8693. doi:10.1002/2017JA024364

Solomon, S., Crutzen, P. J., and Roble, R. G. (1982). Photochemical coupling between the thermosphere and the lower atmosphere: 1. Odd nitrogen from 50 to 120 km. *J. Geophys. Res. Oceans* 87, 7206–7220. doi:10.1029/JC087iC09p07206

Søraas, F., Aarsnes, K., Lundblad, J., and Evans, D. (1999). Enhanced pitch angle scattering of protons at mid-latitudes during geomagnetic storms. *Phys. Chem. Earth, Part C Sol. Terr. Planet. Sci.* 24, 287–292. doi:10.1016/S1464-1917(98)00041-5

Søraas, F., Aarsnes, K., Oksavik, K., Sandanger, M., Evans, D., and Greer, M. (2004). Evidence for particle injection as the cause of Dst reduction during HILDCAA events. *J. Atmos. Solar-Terrestrial Phys.* 66, 177–186. doi:10.1016/j.jastp.2003.05.001

Stepanov, N. A., Sergeev, V. A., Sormakov, D. A., Andreeva, V. A., Dubyagin, S. V., Ganushkina, N., et al. (2021). Superthermal proton and electron fluxes in the plasma sheet transition region and their dependence on solar wind parameters. *J. Geophys. Res. Space Phys.* 126, e2020JA028580. doi:10.1029/2020JA028580

Tenfjord, P., and Østgaard, N. (2013). Energy transfer and flow in the solar wind-magnetosphere-ionosphere system: a new coupling function. *J. Geophys. Res. Space Phys.* 118, 5659–5672. doi:10.1002/jgra.50545

Theodoridis, G. C., and Paolini, F. R. (1967). Pitch angle diffusion of relativistic outer belt electrons. *Ann. Geophys.* 23 (3), 375.

Turunen, E., Verronen, P. T., Seppälä, A., Rodger, C. J., Clilverd, M. A., Tamminen, J., et al. (2009). Impact of different energies of precipitating particles on NOx generation in the middle and upper atmosphere during geomagnetic storms. *J. Atmos. Solar-Terrestrial Phys.* 71, 1176–1189. doi:10.1016/j.jastp.2008.07.005

Tyssøy, H. N., Haderlein, A., Sandanger, M. I., and Stadsnes, J. (2019). Intercomparison of the POES/MEPED loss cone electron fluxes with the CMIP6 parametrization. *J. Geophys. Res. Space Phys.* 124, 628–642. doi:10.1029/2018JA025745

Tyssøy, H. N., Partamies, N., Babu, E. M., Smith-Johnsen, C., and Salice, J. A. (2021). The predictive capabilities of the auroral electrojet index for medium energy electron precipitation. *Front. Astronomy Space Sci.* 8. doi:10.3389/fspas.2021.714146

van de Kamp, M., Rodger, C. J., Seppälä, A., Clilverd, M. A., and Verronen, P. T. (2018). An updated model providing long-term data sets of energetic electron precipitation, including zonal dependence. *J. Geophys. Res. Atmos.* 123, 9891–9915. doi:10.1029/2017JD028253

van de Kamp, M., Seppälä, A., Clilverd, M. A., Rodger, C. J., Verronen, P. T., and Whittaker, I. C. (2016). A model providing long-term data sets of energetic electron precipitation during geomagnetic storms. *J. Geophys. Res. Atmos.* 121. doi:10.1002/2015JD024212

Winningham, J. D., Sharber, J. R., Frahm, R. A., Burch, J. L., Eaker, N., Black, R. K., et al. (1993). The UARS particle environment monitor. *J. Geophys. Res. Atmos.* 98, 10649–10666. doi:10.1029/93JD00461

Xu, W., Marshall, R. A., Tyssøy, H. N., and Fang, X. (2020). A generalized method for calculating atmospheric ionization by energetic electron precipitation. *J. Geophys. Res. Space Phys.* 125, e2020JA028482. doi:10.1029/2020JA028482

Yando, K., Millan, R. M., Green, J. C., and Evans, D. S. (2011). A Monte Carlo simulation of the NOAA POES medium energy proton and electron detector instrument. *J. Geophys. Res. Space Phys.* 116. doi:10.1029/2011JA016671

Zawedde, A. E., Nesse Tyssøy, H., Stadsnes, J., and Sandanger, M. I. (2018). The impact of energetic particle precipitation on mesospheric OH – variability of the sources and the background atmosphere. *J. Geophys. Res. Space Phys.* 123, 5764–5789. doi:10.1029/2017JA025038

Zawedde, A. E., Nesse Tyssøy, H., Stadsnes, J., and Sandanger, M. I. (2019). Are EEP events important for the tertiary ozone maximum? *J. Geophys. Res. Space Phys.* 124, 5976–5994. doi:10.1029/2018JA026201

Zúñiga López, H. D., Tyssøy, H. N., Smith-Johnsen, C., and Maliniemi, V. (2022). The direct effect of medium energy electron precipitation on mesospheric dynamics during a sudden stratospheric warming event in 2010. *Geophys. Res. Lett.* 49, e2022GL097812. doi:10.1029/2022GL097812

Paper III

The High-Energy Tail of Energetic Electron Precipitation: Case Studies

H. Nesse and J. Salice

Submitted to Front. Astron. Space Sci. on 16-March-2024

Graphic design: Communication Division, UiB / Print: Skipnes Kommunikasjon AS

uib.no

ISBN: 9788230869819 (print)
9788230843420 (PDF)